GROWTH AND CHARACTERIZATION OF GROUP III-V NANOSTRUCTURES ON Si SUBSTRATES BY MBE

PhD Dissertation

Burcu ARPAPAY

Eskişehir 2019

GROWTH AND CHARACTERIZATION OF GROUP III-V NANOSTRUCTURES ON Si SUBSTRATES BY MBE

Burcu ARPAPAY

PHD DISSERTATION

Programme in Physics

Supervisor: Assoc. Prof. Uğur SERİNCAN

(Co-supervisor: Prof. Dr. Mehmet Ali GÜLGÜN)

Eskişehir

Eskişehir Technical University

Institute of Graduate Programs

June 2019

This thesis study was supported in part by The Scientific and Technological Research Council of Turkey (TUBITAK) under the Grant No. 116F199 and by Eskişehir Technical University Scientific Research Projects under the project BAP-1305F092.

JÜRİ VE ENSTİTÜ ONAYI

Burcu ARPAPAY'ın "**Growth and Characterization of Group III-V Nanostructures on Si Substrates by MBE**" başlıklı tezi 28/06/2019 tarihinde aşağıdaki jüri tarafından değerlendirilerek "Eskişehir Teknik Üniversitesi Lisansüstü Eğitim-Öğretim ve Sınav Yönetmeliği"nin ilgili maddeleri uyarınca, Fizik Anabilim dalında Doktora tezi olarak kabul edilmiştir.

Jüri Üyeleri	**Unvanı - Adı Soyadı**	**İmza**
Üye (Tez Danışmanı)	: Doç. Dr. Uğur SERİNCAN	.....
Üye	: Doç. Dr. Mustafa KULAKCI	.....
Üye	: Prof. Dr. Aydın DOĞAN	.....
Üye	: Prof. Dr. Raşit TURAN	.....
Üye	: Dr. Öğr. Üyesi Selçuk YERCİ	.....

Prof. Dr. Murat TANIŞLI
Lisansüstü Eğitim Enstitüsü Müdürü

ABSTRACT

GROWTH AND CHARACTERIZATION OF GROUP III-V NANOSTRUCTURES ON Si SUBSTRATES BY MBE

Burcu ARPAPAY

Department of Physics
Eskişehir Technical University, Institute of Graduate Programs, June 2019

Supervisor: Assoc. Prof. Dr. Uğur SERİNCAN
(Co-supervisor: Prof. Dr. Mehmet Ali GÜLGÜN)

Group III-V epilayers and nanostructures were grown on Si (100) substrates by molecular beam epitaxy. GaSb buffer layers on Si substrates to serve as a replacement of GaSb substrate for the Sb-based devices in the long term were investigated in terms of the surface roughness, crystal quality, defects and optical properties. Various growth treatments were carried out to enhance the GaSb epilayer quality and the obtained results were evaluated comparatively. In addition to the nominal substrates vicinal ones were used as well to minimize the common defects observed in lattice mismatch epitaxial growth. GaAs nanowires (NWs) on Si (111) substrates to be used as low dimensional functional devices were grown and the effect of growth parameters on the morphology of NWs were investigated in detail by electron microscopes. Throughout the study the grown samples were deeply analyzed by various characterization tools such as atomic force microscopy, high resolution X-ray diffraction, photoluminescence spectroscopy, scanning electron microscope and transmission electron microscope.

Keywords: GaSb epilayer, GaAs nanowires, Molecular beam epitaxy, Si substrate

ÖZET

Si ALTTAŞ ÜZERİNE III-V GRUBU NANOYAPILARIN MBE TEKNİĞİYLE BÜYÜTÜLMESİ VE KARAKTERİZASYONU

Burcu ARPAPAY

Fizik Anabilim Dalı
Eskişehir Teknik Üniversitesi, Lisansüstü Eğitim Enstitüsü, Haziran 2019

Danışman: Doç. Dr. Uğur SERİNCAN
(İkinci Danışman: Prof. Dr. Mehmet Ali GÜLGÜN)

Bu çalışmada, moleküler demet epitaksi sistemi ile III-V grubu epi-katman ve nanoyapılar Si (100) alttaş üzerine büyütüldü. Sb tabanlı aygıtlar için kullanılan GaSb alttaş yerine Si alttaş üzerine büyütülen GaSb epi-katmanların yüzey pürüzlülüğü, kristal kalitesi, kusur yoğunluğu ve optik özellikleri incelendi. Kristal kalitesini iyileştirmek adına çeşitli büyütme yöntemleri uygulandı ve elde edilen sonuçlar karşılaştırmalı olarak değerlendirildi. Ayrıca örgü uyumsuzluğundan kaynaklanan kusur oluşumlarını indirgemek için farklı özellikte Si alttaşlar kullanıldı ve sonuçları incelendi. Düşük boyutta fonksiyonel aygıtlar için önemli olan Si (111) alttaş üzerine GaAs nanoteller büyütüldü ve elektron mikroskobu tekniği ile büyütme parametrelerinin GaAs nanotel morfolojisine etkisi araştırıldı. Tüm çalışmada büyütülen örnekler, atomic kuvvet mikroskobu, yüksek çözünürlüklü X-ışını kırınımı, fotolüminesans, ve elektron mikrosbu gibi tekniklerle detaylı olarak analiz edildi ve sonuçları sunuldu.

Anahtar Sözcükler: GaSb epi-katman, GaAs nanoteller, Moleküler demet epitaksi, Si alttaş

ACKNOWLEDGMENTS

Foremost, I'd like to thank my advisor Assoc. Prof. Uğur Serincan kindly, whom I pattern myself of his humaneness, approaches and the respect he has towards his job. I should highlight my gratitude for providing me flexible and peaceful research conditions with his friendly attitude, having faith in me more than myself, encouraging and supporting me in my studies and his patience at the unavoidably stressful times caused by the burden of heavy workload. I'd like to state that it is a pleasure to face all the cons and pros starting from the day zero of the Nanoboyut Research Laboratory together with him. The long and the short of it, I feel so fortunate that I have the chance to work with him.

My sincere thanks also goes to Assoc. Prof. Bülent Aslan, for not letting me down with his precious remarks, being a guiding mentor, sharing his experiences and always believing in me. I'd like to state that your effect on my improvement in both life and in science is very precious.

A thank to Assoc. Prof. Mustafa Kulakcı kindly, for endearing me to science with his peerless imitations and models, to nature and history and making me feel a bit smarter as I understand his idiosyncratic humor.

I'd like to thank Prof. Dr. Raşit Turan and Prof. Dr. Aydın Doğan, who are in thesis monitoring committee, for their sensible attitude and precious remarks and refinements that directed my studies.

I'd like to thank Prof. Dr. Mehmet Ali Gülgün and Özgür Duygulu, for their support and contribution of sampling the nanowire samples from TEM analysis process.

Thanks to my Nanoboyut teammates, Seval Şahin, Güven Korkmaz, Mehmet Erkuş, Hülya Kuru Mutlu who provide a sensible and cheery work environment, Onur Şenel who always makes his presence felt with his curious questions, Berkem Hüsam who never debar us from the coffee scent, Ozan Korkan, Muhammed Aktaş and Ali Büyükpınar who immediately showed their support even though they recently joined, and especially Melih Korkmaz, who never cease to help, never left me uninformed of the news in science and provided brief chat sessions that I will miss.

Thanks to Tuğçe Karakulak, my cheerful friend whom we start this path together, later separated, though always wanting me to join the American Dream, for not depraving

me from her voice and my precious friend Berrak Göl, from distant lands, for always showing concern for me.

I'd like to express my thanks especially to my good-hearted friend that I always felt her support with her uplifting attitude, Leyla Başak Büklü, who sweeps away the distance with a single message and always welcomes me in Pendik terminal due to our busy times.

In the remaining times from my studies, my other passion which is Contemporary Dance that I feel the free expression of bodily movement and formed another creation field in which our paths collided with Assoc. Prof. Sernaz Demirel Temel and Assoc. Prof. Tan Temel that I cannot thank enough for acquiring gains from their knowledge and friendships. I'd like to thank my dear friends that colored the gaps of my life, Nur Keskin and Kaan Karaca, whom we together walk in this path, dream, pour out our griefs to each other, burst out laughing, amass reminiscing workshop memories.

I'd like to thank my Arpapay family which I always felt their support in this long road. Especially, I cannot thank enough my dear sisters, Leyla Arpapay and Nesrin Endir who always understand my ideals, be my friends and share my happiness and sorrow. In addition, thanks to my nephew and niece who I enjoy being their aunt, Efe Can Erduran (you know for what it is) and sweet little İrem Endir that always sneaks in and forces the question, "do you love me the most", for making me reminisce about my childhood and youth.

Burcu Arpapay

June, 2019

To My Sister,

Leyla...

28/06/2019

STATEMENT OF COMPLIANCE WITH ETHICAL PRINCIPLES AND RULES

I hereby truthfully declare that this thesis is an original work prepared by me; that I have behaved in accordance with the scientific ethical principles and rules throughout the stages of preparation, data collection, analysis and presentation of my work; that I have cited the sources of all the data and information that could be obtained within the scope of this study, and included these sources in the references section; and that this study has been scanned for plagiarism with "scientific plagiarism detection program" used by Eskişehir Technical University, and that "it does not have any plagiarism" whatsoever. I also declare that, if a case contrary to my declaration is detected in my work at any time, I hereby express my consent to all the ethical and legal consequences that are involved.

Burcu ARPAPAY

TABLE OF CONTENTS

Page

TITLE PAGE ..... **i**

FINAL APPROVAL FOR THESIS ..... **ii**

ABSTRACT ..... **iii**

ÖZET ..... **iv**

ACKNOWLEDGEMENTS ..... **v**

DEDICATION ..... **vii**

STATEMENT OF COMPLIANCE WITH ETHICAL PRINCIPLES AND RULES ..... **viii**

TABLE OF CONTENTS ..... **ix**

LIST OF TABLES ..... **xi**

LIST OF FIGURES ..... **xii**

LIST OF ABBREVIATIONS AND ACRONYMS ..... **xviii**

1. INTRODUCTION **1**

1.1. The Motivation **1**

1.2. The Outline **5**

2. EPITAXIAL GROWTH OF GROUP III-V SEMICONDUCTORS ON Si ... **7**

2.1. Fundamentals of Epitaxial Growth Processes in MBE System **7**

2.2. Challenges of Heteroepitaxial Growth of GaSb on Si **11**

2.2.1. Large lattice mismatch **12**

2.2.2. Large thermal mismatch **15**

2.2.3. Incompatibility of the polar-non-polar surface **16**

2.2.4. Other type of defects **18**

2.3. Nanowire Growth Mechanism **20**

2.3.1. Zinc blende-wurtzite polytypism **21**

3. EXPERIMENTAL METHODS AND DETAILS **23**

3.1. Molecular Beam Epitaxy **23**

3.2. Scanning Electron Microscope **26**

3.3. Transmission Electron Microscope **28**

Page

3.4. Atomic Force Microscopy 29

3.5. Photoluminescence 31

3.6. X-ray Diffraction 32

4. GROWTH OF GaSb ON Si (100) VIA AlSb NUCLEATION LAYER 34

4.1. Introduction 34

4.2. The Effect of AlSb Nucleation Layer Thickness 35

4.3. The Effect of Growth Temperature 42

4.4. The Effect of Post-growth Annealing and Duration 46

4.5. Summary and Conclusions 54

5. GROWTH OF GaSb ON Si (100) VIA GaSb NUCLEATION LAYER 59

5.1. Introduction 59

5.2. The Effect of GaSb Nucleation Layer Thickness 59

5.3. The Effect of GaSb Nucleation Layer Growth Temperature 62

5.4. Summary and Conclusions 64

6. INVESTIGATION OF GaSb EPILAYERS GROWN WITH VARIOUS METHODS 66

6.1. Introduction 66

6.2. The Role of Vicinal Substrate Surfaces on GaSb Epilayers 66

6.3. The Growth of GaSb Epilayers with Superlattice Layers 70

6.4. Conclusions 72

7. GROWTH OF GaAs NANOWIRES ON Si (111) 74

7.1. The Effect of Growth Temperature 74

7.2. The Effect of Group III and V Flux 84

7.3. Conclusions 91

8. CONCLUSIONS AND FINAL REMARKS 92

REFERENCES 95

CURRICULUM VITAE

LIST OF TABLES

Page

Table 2.1. Material properties of GaSb and Si [75] 12

Table 4.1. Growth parameters for the samples in Set 1 34

Table 4.2. Growth parameters for the samples in Set 2 34

Table 4.3. Growth parameters for the samples in Set 3 35

Table 4.4. Summary of the HRXRD results for the samples in Set 2 for different GaSb growth temperatures 42

Table 4.5. Summary of the HRXRD results for the samples in Set 3 for different post annealing temperatures 47

Table 4.6. Summary of the obtained results for the samples in Set 1 with different AlSb nucleation layer thicknesses 55

Table 4.7. Summary of the obtained results for the samples in Set 2 for different GaSb growth temperatures 56

Table 4.8. Summary of the obtained results for the samples in Set 3 for different post annealing temperatures 57

Table 5.1. Growth parameters for the samples in Set 4 59

Table 5.2. Growth parameters for the samples in Set 5 59

Table 5.3. Summary of the obtained results for the samples NB1-3 and NB5-2 65

Table 6.1. The Si (100) substrate types for the samples in Set 6 66

Table 6.2. Summary of the obtained results for the samples in Set 6 and Set 7 73

Table 7.1. Growth parameters for the samples in Set 8 74

Table 7.2. Growth parameters for the samples in Set 9 84

LIST OF FIGURES

Page

Figure 1.1. The plot of bandgap energy/thermal expansion coefficients (at 300 K) versus lattice constant/misfit for group III-V and IV 2

Figure 1.2. The publishing result for III-V nanowires on silicon substrates by year, received from Scopus 4

Figure 2.1. Schematic illustration of basic processes during epitaxial growth 7

Figure 2.2. The interaction potential seen by an atom or molecule due to the surface 8

Figure 2.3. Schematic of basic growth modes 10

Figure 2.4. Step flow growth on vicinal substrate surface 11

Figure 2.5. Schematic illustration of lattice-matched layer, pseudomorphic layer and partially relaxed layer with a misfit dislocation in epitaxial growth 13

Figure 2.6. (a) A closed loop around a dislocation and (b) the same atom to atom path in a defect-free crystal lattice; the black arrow indicates the Burgers vector 14

Figure 2.7. Schematically illustration of (a) edge dislocation and (b) screw dislocation. The red arrows indicate the Burgers vectors 14

Figure 2.8. Unit cell of (a) diamond structure Si and (b) zinc blende structure GaSb 16

Figure 2.9. (a) APBs in GaSb formed by a single step on the Si substrate and (b) suppression APBs in GaSb epilayer by featuring double step on the Si substrate surface 17

Figure 2.10. Self-annihilation of an APB by kinking to higher index planes 18

Figure 2.11. A schematic representation of stacking sequences of ZB structure 19

Figure 2.12. A schematic representation of (a) perfect ABC stacking sequence (ZB), (b) stacking sequence with intrinsic SF, (c) extrinsic SF and (d) a twin boundary 19

Figure 2.13. Schematic illustration of the VLS growth mechanism 20

Figure 2.14. Schematic illustration of self-assisted GaAs NWs on Si (111) substrate 21

Figure 2.15. Crystal structure of (a) ZB and (b) WZ GaAs: ..ABCABC.. and ..ABAB.. demonstrate stacking sequences, respectively 22

Figure 3.1. Basic schematic illustration of an MBE system 24

Figure 3.2. Schematic diagram of an SEM 27

Figure 3.3. The signals generated by electron-matter interaction in the SEM 28

Page

Figure 3.4. (a) Picture of a holey carbon grid and (b) TEM image of GaAs NW suspended on holey carbon film 29

Figure 3.5. Basic schematic diagram of an AFM 30

Figure 3.6. Interaction force versus distance between AFM tip and sample surface 31

Figure 3.7. Schematically illustrated basic PL processes in a semiconductor 32

Figure 3.8. Schematic representation of X-ray diffraction in a crystal 33

Figure 4.1. RHEED patterns at the [110] azimuth (a) during the growth of AlSb NL with thickness of 20 ML indicating 3D island nucleation, (b) towards to the end of the growth of AlSb NL with thickness of 80 ML which indicates the island coalescence, (c) during the growth of GaSb epilayer representing (1x3) reconstructed surface and (d) the SEM image of AlSb NL with thickness of 20 ML 35

Figure 4.2. The FWHM of X-ray RC around the (004) reflection and the TD density of GaSb epilayers as a function of AlSb NL thickness 36

Figure 4.3. 3D AFM images of the samples in Set 1 with AlSb NL thickness of (a) 5 ML, (b) 10 ML, (c) 20 ML, (d) 40 ML and (e) 80 ML 37

Figure 4.4. SEM images of GaSb epilayers grown on Si with AlSb NL thickness of (a) 5, (b) 10, (c) 20, (d) 40 and (e) 80 MLs. The MTs and APBs are marked by yellow and violet arrows, respectively in (e) 38

Figure 4.5. The MT density and RMS of the GaSb epilayers grown on Si as a function of AlSb NL thickness 38

Figure 4.6. SEM images of etched GaSb epilayers grown on Si having AlSb NL thickness of (a) 5, (b) 10, (c) 20, (d) 40 and (e) 80 MLs 39

Figure 4.7. The APB density, RMS and PV of the GaSb epilayers grown on Si as a function of AlSb NL thickness. The dotted lines are guide for the eyes. The APB density is obtained from etched where the RMS and PV values are obtained from the as-grown samples 40

Figure 4.8. 10 K PL spectra of the samples in Set 1 with different AlSb NL thicknesses. From the fit (solid black line) of the measured spectra (dotted black line) using Gaussian distribution the accurate peak positions/intensities and the energy values were found. The BA, DA, BE and FE peaks are identified by the green, red, blue and orange lines, respectively 41

Figure 4.9. 3D AFM images of the samples for the growth temperature of (a) 530 ºC, (b) 550 ºC and (c) 570 ºC 42

Figure 4.10. The MT density and RMS of the GaSb epilayers grown on Si as a function of growth temperature 43

Page

Figure 4.11. SEM images of as-grown GaSb epilayers on Si at the growth temperature of (a) 530, (b) 550 and (c) 570 ºC 43

Figure 4.12. SEM images of etched GaSb epilayers on Si at the growth temperature of (a) 530, (b) 550 and (c) 570 ºC 44

Figure 4.13. The APB density, RMS and PV of the GaSb epilayers grown on Si as a function of growth temperature. The dotted lines are guide for the eyes. The APB density is obtained from etched where the RMS and PV values are obtained from the as-grown samples 45

Figure 4.14. 10 K PL spectra of the samples in Set 2 for different GaSb growth temperatures (T_g). From the fit (solid black line) of the measured spectra (dotted black line) using Gaussian distribution the accurate peak positions/intensities and the energy values were found. The BA, DA, BE and FE peaks are identified by the green, red, blue and orange lines, respectively 46

Figure 4.15. SEM images of GaSb epilayers grown on Si and post annealed at (a) none, (b) 550 and (c) 570 and (d) 590 ºC with EDX analysis 48

Figure 4.16. 3D AFM images of the samples for a post annealing temperatures of (a) none, (b) 550 ºC and (c) 570 ºC 48

Figure 4.17. The MT density and RMS of the GaSb epilayers grown on Si as a function of post annealing temperature 49

Figure 4.18. SEM images of etched GaSb epilayers on Si grown at 530 ºC (a) as-grown and post annealed at (b) 550 ºC and (c) 570 ºC for 30 min 50

Figure 4.19. The APB density, RMS and PV of the GaSb epilayers grown on Si as a function of post-growth annealing temperature. The dotted lines are guide for the eyes. The APB density is obtained from etched where the RMS and PV values are obtained from the as-grown samples 50

Figure 4.20. 10 K PL spectra of the samples in Set 3 for different post annealing temperatures (T_a). From the fit (solid black line) of the measured spectra (dotted black line) using Gaussian distribution the accurate peak positions/intensities and the energy values were found. The BA, DA, BE and FE peaks are identified by the green, red, blue and orange lines, respectively 51

Figure 4.21. The FWHM of X-ray RC around the (004) reflection, the TD density and APB density of the GaSb epilayers grown at the temperature of 570 ºC as a function of post-growth annealing duration. The dotted lines are guide for the eyes. The APB density is obtained from etched samples 52

Figure 4.22. SEM images of as-grown GaSb epilayers on Si post annealed at 570 ºC for (a) 30 min (b) 60 min and (c) 120 min. SEM images of etched GaSb epilayers on Si post annealed at 570 ºC for (a) 30 min (b) 60 min and (c) 120 min. The MTs are marked by yellow arrows in (c) 52

Page

Figure 4.23. The growth steps of the samples (a) NB3-6 and (b) NB3-7 53

Figure 4.24. SEM image of the samples (a) NB3-4, (b) NB3-6 and (c) NB3-7. SEM image of the etched samples (d) NB3-4, (e) NB3-6 and (f) NB3-7. The MTs and APBs are marked by yellow and violet arrows, respectively in (c) and (f) 54

Figure 4.25. The FWHM of X-ray RC around the (004) reflection, the TD density and APB density of the samples, NB3-4, NB3-6 and NB3-7. The dotted lines are guide for the eyes. The APB density is obtained from etched samples 54

Figure 4.26. The GaSb layers grown directly on Si at a growth temperature of 530 ºC with group V/III ratio of (a) 10 and (b) 20 55

Figure 4.27. 3D AFM image of the sample that contains 20 ML AlSb IMF layer and post annealed at 550 ºC. The RMS value is determined as 0.4 nm 58

Figure 5.1. The FWHM of X-ray RC around the (004) reflection and the TD density of GaSb epilayers as a function of GaSb NL thickness 60

Figure 5.2. SEM images of GaSb epilayers grown on Si with GaSb NL thickness of (a) 2, (b) 8, (c) 24, (d) 40 and (e) 80 MLs. The MTs and APBs are marked by yellow and violet arrows, respectively 61

Figure 5.3. SEM images of etched GaSb epilayers grown on Si having with GaSb NL thickness of (a) 2, (b) 8, (c) 24, (d) 40 and (e) 80 MLs. The MTs and APBs are marked by yellow and violet arrows, respectively 61

Figure 5.4. The APB density and RMS of the GaSb epilayers grown on Si as a function of GaSb NL thickness 62

Figure 5.5. The FWHM of X-ray RC around the (004) reflection and the threading dislocation density of GaSb epilayers as a function of growth temperature of GaSb NL 63

Figure 5.6. SEM images of as-grown GaSb epilayers having GaSb NL grown at the growth temperature of (a) 350, (b) 400, (c) 450 and (d) 500 ºC. SEM images of etched GaSb epilayers having GaSb NL grown at the growth temperature of (e) 350, (d) 400, (g) 450 and (h) 500 ºC 63

Figure 5.7. The APB density and RMS of the GaSb epilayers grown on Si as a function of GaSb NL thickness 64

Figure 6.1. (a) represents the SEM image of NB1-3 as a reference sample. SEM images of GaSb epilayers grown on Si (100) vicinal surfaces with (b) 0.15º, (c)2º, (d) 4º and (e) 6º towards [110] direction 67

Figure 6.2. (a) represents the 3D AFM image of NB1-3 as reference sample. 3D AFM images of GaSb epilayers grown on Si (100) vicinal surfaces with (b) 0.15º, (c)2º, (d) 4º and (e) 6º towards [110] direction 68

Page

Figure 6.3. The FWHM of X-ray RC around the (004) reflection, the TD densities and APB densities of the samples having miscut angles of 0.15, 2, 4 and 6°. The dotted lines are guide for the eyes. The APB density is obtained from etched samples 69

Figure 6.4. (a) represents the SEM image of NB1-3 as a reference sample. SEM images of etched GaSb epilayers grown on Si (100) vicinal substrates (b) 0.15°, (c) 2°, (d) 4° and (e) 6° towards [110] direction 69

Figure 6.5. Step geometry of vicinal Si (100) substrate 70

Figure 6.6. Schematic representation of GaSb epilayer structures of the samples, NB7-1 and NB7-2 70

Figure 6.7. The XRD pattern of the sample, NB7-2 71

Figure 6.8. (a) represents the 2D AFM image of NB1-3 as a reference sample. 3D AFM images of GaSb epilayers grown on nominal Si (100) substrates (b) NB7-1 and (c) NB7-2. The blue circles denote the MTs 71

Figure 6.9. (a) represents the SEM image of NB1-3 as reference sample. SEM images of etched GaSb epilayers grown on nominal Si (100) substrates (b) NB7-1, (c) NB7-2 72

Figure 7.1. Tilted-view SEM images of the samples of NBW1-2-3. The SEM images of the parasitic growth regions on the sample surfaces are framed in violet 75

Figure 7.2. EDS profile of a NW extracted from NBW-1 which belongs to (a) the tip of NW (region 1) and (b) just below the tip of NW (region 2) 76

Figure 7.3. The average length of NWs obtained from the samples in Set 8 as a function of growth temperature 77

Figure 7.4. The variation of vertical and non-vertical NW density with respect to the growth temperature 78

Figure 7.5. (a) The illustration of convex-like NW, (b) the illustration of inversed tapered NW and the tapering formula and (c) the variation of NW diameter with respect to the growth temperature; the tapering amounts are specified on the graph 80

Figure 7.6. SEM images of the individual GaAs NW samples gathered from (a) NBW-1, (b) NBW-2 and (c) NBW-3 81

Figure 7.7. Time evolution of RHEED patterns observed during the growth of NBW-1, (a) showing the appearance of spotty RHEED patterns gradually and the formation of twinned ZB phase at the initial stage, (b) indicating ZB/WZ mixed phase at the growth time of 1 min, (c) showing the transition to twin-ZB phase at the growth time of 15 min, and (d) the re-observation of twinned ZB and WZ spots at the

end of the growth. Twin-ZB and WZ spots are denoted by white arrows 82

Figure 7.8. TEM images of the NWs collected from NBW-1 83

Figure 7.9. TEM image of a GaAs NW obtained from the sample NBW-1. The SAED patterns captured from the regions 1 and 2 on the GaAs NW indicates ZB phase and twinned ZB phase, respectively 83

Figure 7.10. (a) The TEM image and (b) EDS mapping of a single GaAs NW from NBW-1, (c-e) corresponding elemental distribution maps of Ga-K, As-K, O-K, respectively 84

Figure 7.11. Tilted-view SEM images of the samples (a) NBW-4, (b) NBW-5 and (c) NBW-6 85

Figure 7.12. Average length of NWs as a function of Ga growth rate and V/III flux ratio 85

Figure 7.13. The role of group V flux on the average length of GaAs NWs grown at 0.07 and 0.18 nm/s Ga growth rates 86

Figure 7.14. Average diameter and tapering obtained from the GaAs NWs 87

Figure 7.15. TEM images of the samples (a) NBW-4, (b) NBW-5 and (c) NBW-6 88

Figure 7.16. (a) The TEM image and (b) EDS line profile analysis of a single GaAs NW collected from NBW-4 and (c-d) corresponding elemental distribution maps of Ga-K, As-K, respectively 89

Figure 7.17. The TEM images of a NW belong to the sample NBW-5. (a) HRTEM low-magnification overview, (b) HRTEM image of pure ZB phase, (c) FFT pattern of point 1. (d) HRTEM image of twinned ZB segment, (e) and (f) FFT and SAED patterns of rotational twinned ZB region (point 2), respectively, (g) HRTEM image of pure ZB phase, (h) FFT pattern of point 3, (i) HRTEM image of the top segment of NW, (j) FFT pattern of pure ZB segment, (k) SAED pattern that indicates WZ and twinned ZB with the planar defects region and (l) FFT pattern that shows WZ phase of the segment under the Ga droplet 90

LIST OF ABBREVIATIONS AND ACRONYMS

AlSb : Aluminum antimonide

AFM : Atomic force microscopy

APD : Anti-phase domain

APB : Anti-phase boundary

Au : Gold

BEP : Beam equivalent pressure

BFM : Beam flux monitor

EDS : Energy dispersive x-ray spectroscopy

FWHM : Full width at half maximum

HRTEM : High resolution transmission electron microscope

HRXRD : High resolution x-ray diffraction

GaAs : Gallium arsenide

GaSb : Gallium antimonide

IMF : Interfacial misfit

MBE : Molecular beam epitaxy

MT : Micro-twin

NL : Nucleation layer

NW : Nanowire

PL : Photoluminescence

PV : Peak-to-valley

QD : Quantum dot

RC : Rocking curve

RGA : Residual gas analyzer

RHEED : Reflection high-energy electron diffraction

RMS : Root mean square

SAE : Selective area epitaxy

SEM : Scanning electron microscope

Si : Silicon

SF : Stacking fault

SL : Superlattice

TD : Threading dislocation

UHV : Ultra-high vacuum

VLS : Vapor-liquid-solid

VS : Vapor-solid

1. INTRODUCTION

1.1. The Motivation

In the semiconductor technology, the integration of electronic and photonic components on the same integrated circuit has been an increasing demand for the multi-purpose systems [1,2]. Silicon (Si) with very special properties is the basic semiconductor used in the integrated circuits, involving as transistors and diodes from past five decades and today about 95% percent of semiconductor devices have been produced on Si substrates. The usage of Si in this platform offers some prominent advantages such as robust mechanical properties, higher thermal conductivity, acting as a good insulator, larger-diameter wafer with high quality and low-cost and nature abundance. However, it is not preferable for optoelectronics due to the indirect band nature, leading to low light emission efficiency. On the other hand, group III-V compound semiconductors are predominant in optoelectronics and high-speed devices owing to the direct band nature and the high mobility properties, which are commonly processed on gallium arsenide (GaAs) or gallium antimonide (GaSb) wafers. However, GaAs and GaSb wafers are not cost-effective compared to Si substrates. Naturally, the concept of the direct heteroepitaxial integration of group III-V compounds on Si had been arisen as a need, as well as, non-epitaxial group III-V on Si techniques (i.e. bonding) for achieving the goals in this trend [2-8]. Abstractly, if the heteroepitaxial growth of group III-V compound on Si substrates is performed successfully, it will become the most functional and practical path in the optoelectronic industry. Yet, the drawbacks emerge in the matter of the epitaxial growth of group III-V compound semiconductors on Si substrates. The fundamental challenges are large lattice mismatch, differences in the thermal expansion coefficients and non-polar surface chemical bonding feature of Si (Figure 1.1) [9]. So, the success of that interest is directly related to overcome those problems between group III-V compound semiconductors and Si substrate. Because the generation of defects such as anti-phase boundaries (APBs), threading dislocations (TDs), stacking faults (SFs), micro-twins (MTs) and crack formation during the epitaxial growth of group III-V on Si substrates are inevitable, some detrimental effects have been observed on device performances [10-17]. Up to now, although group III-V based devices on Si substrates have been reported by applying various growth approaches [18-22], there is still a limiting factor due to the defect formation and hence, those approaches need to be

improved for high quality optoelectronic applications. At this point, to explore an effective buffer layer on Si, which would curtail the defects penetrating into the device structure, is worthy for the growth of mismatched heteroepitaxy of semiconductors.

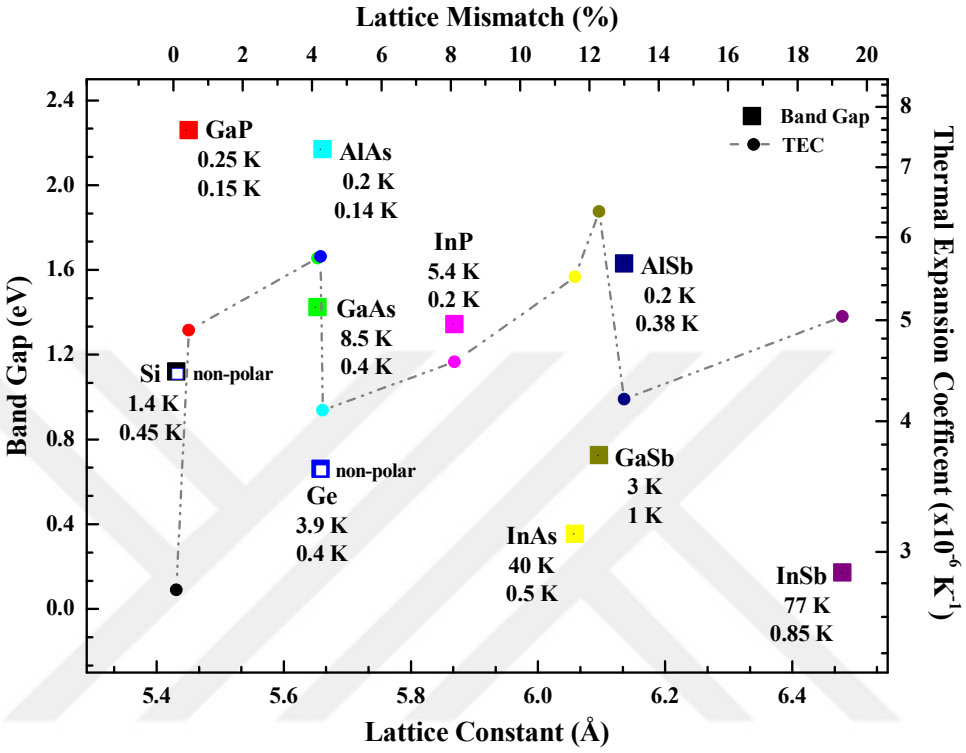

Figure 1.1. *The plot of bandgap energy/thermal expansion coefficients (at 300 K) versus lattice constant/misfit for group III-V and IV, the data were adopted from references [23-24]. The numbers below the chemical symbols are electron and hole mobilities in units of cm^2/V.s. Each semiconductor material is represented by different color. Empty squares and solid squares indicate the band gap energy of nonpolar and polar semiconductors, respectively. Solid circles indicate the thermal expansion coefficient (TEC).*

Among group III-V compound semiconductors, GaSb substrate is a good choice owing to its lattice parameter compatibility with various ternary and quaternary group III-V compounds. GaSb has a band gap of 0.726 eV at room temperature. Together with other electrical properties, that makes GaSb to be a good choice for a wide range of applications such as laser diodes, tandem solar cells, thermophotovoltaics, infrared photodetectors and high frequency devices [25-28]. However, those favorable properties of GaSb are limited by cost related factors such as lack of large-scale, defect-free and semi-insulating GaSb substrates. Those limitations channel researchers to develop new approaches to reduce the cost of GaSb based devices. One way of solving cost related factors is to use an epitaxial method to grow GaSb epilayer on Si substrate which is

a comparatively cheap and easily available substrate in large-scale. Hence, achieving high quality GaSb epilayer on Si substrate is of increasing interest as it would allow the integration of the unique properties of 6.1 Å group III-V family materials with the mature Si technology. Yet, the lattice mismatch between GaSb and Si is quite large (~12.2%) which makes it more challenging to grow high crystal quality GaSb epilayers on Si substrates (Figure 1.1). In particular, considering integration of Sb based devices with Si, the buffer layer having smooth surface with devoid of defects is important for the growth of thin film heterostructures.

Luckily, improvements in epitaxial growth systems allow researchers to overcome that complication by using various methods such as aluminum antimonide (AlSb) quantum dots (QDs) as a seed for a better initiation of GaSb on Si, Si substrates with various miscut angles to prevent anti-phase domains (APDs) and variable steps such as superlattice (SL) intermediate layers, post-growth annealing, low/high growth temperature combinations etc. to decrease the defects throughout the buffer GaSb layer [29-35].

Up to now, the defects that could be formed during the growth of GaSb on Si have been extensively studied by high-resolution transmission electron microscopy (HRTEM) [33,34,36-39]. In addition to those reports, in Ref [40] where AlSb nucleation layer (NL) were used on highly miscut Si substrate, TDs and MTs were observed by atomic force microscopy (AFM) and it was found that the density of the MTs increases with an increase in AlSb NL thickness. Furthermore, in the same study, it was reported that the surface roughness of the GaSb epilayer was dominated by those MTs. In another study, it was shown that two step (low followed by high growth temperature) growth of GaSb on Si by metalorganic chemical vapor deposition results in an APBs free surface with very low surface roughness but a TDs density at a level of 10^9 cm ^{2} [41]. Huu Ha et. al. [42] introduced a GaSb layer grown on temperature-graded GaAs buffer layer, which has a TD density of $5x10^{-6}$ cm^{-2}. Also, Craig et. al. [43] benefited from GaSb/AlSb SLs as a dislocation filter in the GaSb buffer layer and by this way the TD density was reduced to $1x10^8$ cm^{-2} from $1x10^{10}$ cm^{-2} at the interface. Madisetti et al. [44] introduced a more complex structure (AlSb QDs + GaSb/AlSb SL + InSb QDs) and the density of MTs was determined as ~$2x10^4$ cm^{-1} for 800 nm thick GaSb layer. By introducing a similar structure called as metamorphic buffer layer, Sasaki et. al. [45] indicated that MTs and TDs were still observed for the sample grown on miscut substrate although domain APD

suppression was achieved and compared to the sample grown on off-cut zero Si substrate, the density of MTs (~$5x10^3$ cm^{-1}) and TDs (~$1x10^8$ cm^{-2}) were halved. Obviously, in order to grow device quality films, it is crucial to define and reduce the density of the defects that can reach to the surface.

For the integration of III-V compounds on Si technology platform, the other promising roadmap is to make use of the group III-V nanowires (NWs). NWs are favorable nanostructures with the properties of high aspect ratios, the tailored diameter, higher thermal/electrical mobility and the integrability with flexible substrates [46-47]. When considering III-V compound semiconductors with unique properties, semiconductor NWs exhibit compatible platform to optoelectronics technology with the ability of axial and radial heterostructures growth. Besides, in this context, the growth of group III-V NWs on low cost Si substrates helps to eliminate APBs and TDs as a consequence of reduced strain energy, compared to high mismatched heteroepitaxy films on Si. Hence, the studies have shown that group III-V compound based NW devices such as transistors, LEDs, solar cells and lasers, [48-53] are up for the future optoelectronics. Thus an increasing effort on the investigation of NW growth on Si have gained a popularity for last 15 years (Figure 1.2). Among group III-V compound NWs, GaAs NWs are one of the most promising nanostructures with the ideal band gap, high carrier mobility for the nano-electronics and optical/sensing applications [54-57].

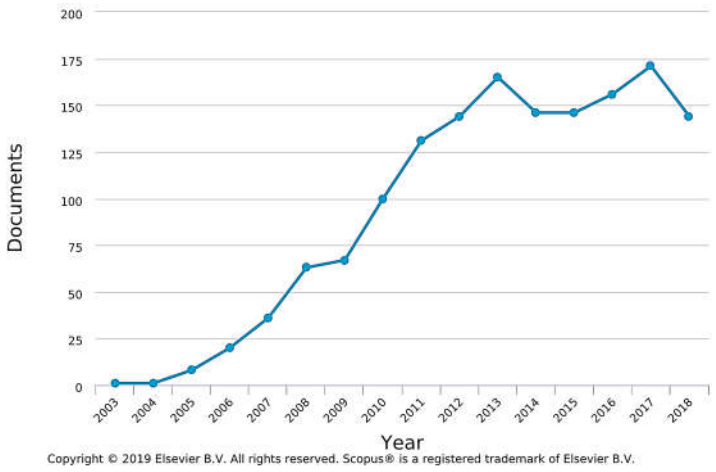

Figure 1.2. *The publishing result for III-V nanowires on silicon substrates by year, received from Scopus.*

One of the dominant method to synthesize group III-V NWs is vapor-liquid-solid (VLS) growth by initiating the crystallization from beneath a metal catalyst [58-60], that

is mostly gold (Au). Yet, Au catalyzed NWs may lead to the degradation in NWs due to diffusion of Au atoms into NWs [61-63] and causing trap levels. Alternatively, it is able to assist self-seeded group III-V NWs by using group III elements as a catalyst. Thus, it provides clean growth process without using a foreign catalyst. As a matter of the fact that, Ga assisted GaAs NWs can also be directly processed on Si substrates having native oxide [64-66]. Also, selective area epitaxy (SAE) growth is performed, that is, the growth is initiated on a substrate covered by a dielectric layer such as SiO_x, having well-defined openings [51, 67]. It allows for identical surrounding during the growth and the position control and the density.

In this stage, considering group III-V NW growth on Si substrates, it is necessary to find out a reproducible way for manufacturing. This is because group III-V NW formation is highly sensitive to the growth kinetics and the substrate surface condition. So the most important factor in the growth of group III-V NWs on unpatterned Si substrates is to overcome some difficulties: To manage the control of NW density, to have uniform distribution in size, to adjust the growth direction (vertical/non-vertical) of whole NWs due to the polar nature of Si [68], to have a consistent growth condition on the native oxide depending on its properties according to the different wafer batches [69] and to preserve the crystal phase with the lack of defects such as SFs and twins for whole NWs.

1.2. The Outline

The objective of this thesis is to execute group III-V compound heteroepitaxial layers and nanostructures grown on Si substrates by molecular beam epitaxy (MBE) with applying various methods, for the comprehensive understanding of the growth dynamics and the enhancement of the structures. Within the scope of the thesis, the focus is on the process of GaSb buffer layers on Si (100) substrates to serve as a replacement of GaSb substrate for the Sb-based devices in the long term and GaAs NWs on Si (111) substrates to be used as a low dimensional functional devices. As a buffer layer, GaSb epilayers grown on Si (100) substrates were investigated in terms of the surface roughness, crystal quality, defects and optical properties. Also, various growth treatments were carried out to enhance the GaSb epilayer quality and the obtained results were evaluated comparatively. For GaAs NWs on Si (111) substrates, it was concentrated on the effect of growth parameters on the morphology of NWs.

This thesis consists of eight chapters. Chapter 2 deals with a general overview of the epitaxial growth process, including the fundamental challenges for the highly mismatched group III-V compounds on Si. Chapter 3 gives an overview of the main characterization methods and the experimental details. In Chapter 4, the GaSb epilayers with AlSb NL layer grown on nominal Si (100) substrates were examined. In Chapter 5, the role of GaSb NL on the growth of GaSb epilayers on nominal Si (100) were explained. Chapter 6 offers the effect of alternative methods (the use of vicinal Si substrate and SLs layer) on the growth of GaSb epilayers. In Chapter 7, the influence of the growth parameters on the process of Ga-assisted GaAs NWs on Si (111) was investigated. Finally, the concluding remarks and future works are presented in Chapter 8.

2. EPITAXIAL GROWTH OF GROUP III-V SEMICONDUCTORS ON Si

2.1. Fundamentals of Epitaxial Growth Processes in MBE System

Epitaxy is defined as the growth of an orientated monocrystalline layer on a monocrystalline substrate where the orientation is determined by the substrate and the overlayers deposited on the substrate. The epitaxy is generally classified in two types: Homoepitaxy and Heteroepitaxy. Homoepitaxy is the growth of the epitaxial layer on which the substrate is identical (i.e. GaSb on GaSb). Heteroepitaxy is the case of the epitaxial layer grown on a dissimilar substrate (i.e. GaAs on GaSb). Thus, the heteroepitaxy is the base of semiconductor devices including various heterostructures. One of the preferred epitaxy technique to attain the high quality multilayered heterostructures is MBE system in modern technology.

In an MBE system, a series of surface processes can happen with the start of exposing the substrate to the atomic or molecular beam and many of these processes are depend on the specific growth parameters (the surface orientation, the substrate temperature, the atomic species and flux). During the epitaxial growth, the surface processes can be summarized as: Adsorption of the atoms or molecules on the substrate surface, diffusion of the adatoms on the surface to find energetically preferred crystal site, the arrangement of the constituent atoms of the substrate/epilayer and thermal desorption of the species not incorporated into the lattice site, as shown in Figure 2.1 [70].

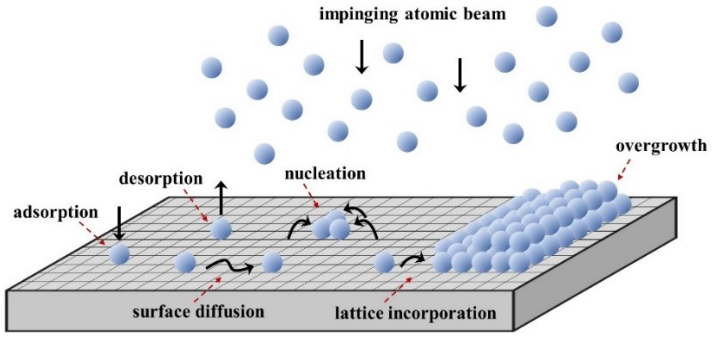

Figure 2.1. *Schematic illustration of basic processes during epitaxial growth.*

In the case of adsorption, the atomic or molecular species are physisorbed or chemisorbed on the surface. Physisorption is the state where no electron transferring takes place between the adsorbate and the adsorbent by forming van der Waals bonds, while

chemisorption refers to electron transferring between the adsorbate and the adsorbent by forming ionic or covalent bond. The interaction potentials seen by an incoming molecule is illustrated in Figure 2.2. As an exception; a variety of other potential configurations can also exist. Figure 2.2 demonstrates that the adsorbed specie in the physisorbed state has to overcome a lower barrier when it is subsequently chemisorbed at the surface rather than the re-evaporation into the vacuum [70]. Actually in this case, the physisorbed state means the precursor state. The species adsorbed via weak physisorption are allowed to migrate on the surface or desorbed from the surface until occupied by the vacant sites in the chemisorbed state.

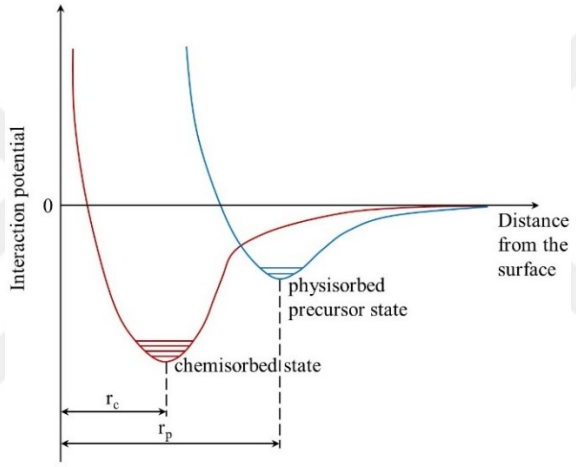

Figure 2.2. *The interaction potential seen by an atom or molecule due to the surface.*

The surface processes during the MBE growth depend on kinetic parameters which allow to control the crystallization process and also it is very important to understand the thermodynamics of growth to attain functional epitaxial structures. The adsorption is described quantitatively by the thermal accommodation coefficient and the sticking coefficient. The atom or molecular beam exposed to the substrate has an energy distribution depending on the effusion cell temperature T_i. When the atoms reaching the substrate surface which has a temperature T_s, they either re-evaporate immediately with an energy corresponding to a temperature of T_e or exchange energy with the atoms on the surface until they come to a thermodynamic equilibrium at T_s. This condition is defined as thermal accommodation coefficient (α) which is expressed as:

$$\alpha = \frac{T_i - T_e}{T_i - T_s} \tag{2.1}$$

When considering T_e is equal to T_s, the thermal accommodation coefficient will be unity which means the measure of the extent of the arriving atoms in the state of thermodynamic equilibrium with the substrate. The sticking coefficient (s), on the other hand, is the ratio of the number of atoms adhering to the substrate surface (N_{adh}) to the atoms arriving there (N_{tot}), as defined in Equation 2.2. It must be stated that the sticking coefficient and the thermal accommodation coefficient are different quantities and should not be used interchangeably.

$$s = \frac{N_{adh}}{N_{tot}} \tag{2.2}$$

In most instances, the sticking coefficient is less then unity depending on the growth condition such as low adsorption energy of atoms or high substrate temperature. To put it more explicitly, all atoms on the substrate surface would be accommodated in the thermodynamic equilibrium, representing the case of α=1. But it doesn't mean that all atoms will stay in this condition permanently. If they find sufficient energy to overcome the attractive forces, some of the adatoms can re-evaporate. Therefore s can be nearly equal to zero even though α is unity. Considering the adsorption, the sticking coefficients for the chemisorbed and physisorbed phase can be dissimilar. In the case of the chemisorption process, the sticking coefficient may be depend on orientation of the substrate surface and spatial distribution of the adatoms on the surface. For physisorbed phase, the sticking coefficient may show no dependence to the orientation and surface site arrangement [70].

During epitaxial growth, the surface energies between the epitaxial layer and substrate is leading to reach thermal equilibrium conditions. As already been mentioned, the growth in MBE is also a kinetic process and the mobility of the adatoms on the surface can have an effect on the behavior of the deposition. Among all kinetic parameters, it is quite likely that the most important one is the diffusion coefficient which determines the average distance of an atom on the surface before bonding to the lattice sites. This distance is termed as the surface diffusion length (l_D) and is given in Equation 2.3 where τ is the residence time before re-evaporation and D_s is the surface diffusion coefficient.

$$l_D = \sqrt{D_s \tau} \tag{2.3}$$

Commonly, τ for group III elements can be taken as the inverse of the growth rate due to negligible re-evaporation of group III elements. Similarly, the surface diffusion

coefficient is expressed in Equation 2.4 where E_A is the activation energy, v is the attempt frequency and a is the characteristic jump distance [71].

$$D_s = va^2 e^{-\frac{E_A}{k_B T}} \tag{2.4}$$

Here, it is seen that the growth temperature is a determining factor in the change of the effective surface diffusion coefficient. Hereby, the growth modes in MBE system is controlled by kinetic factors as well as thermodynamics.

Epitaxial growth is mainly classified into three growth modes: the Frank-van der Merwe mode for two dimensional layer by layer growth, the Stranski-Krastonov mode for layer plus island growth, and Volmer-Weber mode for three dimensional island formation, as schematically illustrated in Figure 2.3. Those growth regimes hinge on the material system with its growth kinetics where the surface energies and interface energy at the substrate-epitaxial layer strongly determines the equilibrium morphology [72].

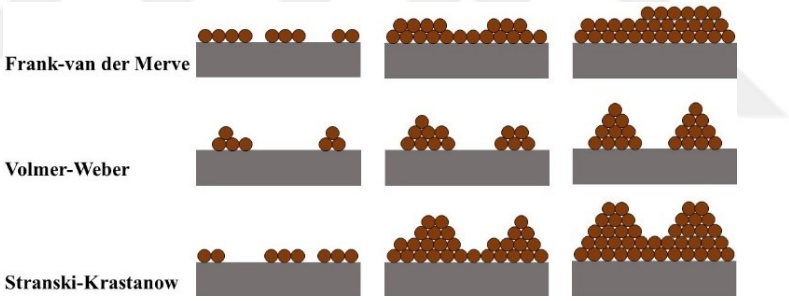

Figure 2.3. *Schematic of basic growth modes.*

In Frank-van der Merwe growth mode, the surface energy of the substrate is higher than the one between layer constituents, thus the layer constituents bond strongly to the substrate surface to reduce the total surface energy. This situation is expressed by Equation 2.3 where $\gamma_s, \gamma_l, \gamma_{sl}$ are the substrate, layer and interface surface energies, respectively.

$$\gamma_s \geq \gamma_l + \gamma_{sl} \tag{2.3}$$

Initially, one monolayer wets the substrate surface and a continuous uniform layer is deposited on the substrate surface. Then the process repeat itself as illustrated in Figure 2.3, wherefore referring to the layer by layer growth (Frank-van der Merwe).

The Volmer-Weber growth mode occurs when the binding force between the layer constituents is stronger rather than the substrate and the layer. This results in the nucleation of the layer constituents as 3D islands directly on the substrate surface. Therefore, the energy reduction condition takes place as given in Equation 2.4.

$$\gamma_s < \gamma_l + \gamma_{sl} \tag{2.4}$$

In Stranski-Krastonov growth mode, the mixed growth happens, namely, the first few monolayer forms until exceeding the critical thickness, then the subsequent layer prefers the island growth on this wetting layer. This case is attributed to the mismatch in lattice constants between the substrate and the layer. During the growth, the stress is induced to the interface and the growth mode changes by the strain relieving after the point will reach up to the critical thickness.

The epitaxial growth is usually executed on nominal substrate where in some cases vicinal substrate is preferred which is cut along a direction vicinal to a high symmetry orientation. The step flow growth refers to the growth on the substrate surface with terraces separated by steps, as shown in Figure 2.4. Here θ is the surface orientation angle determined by the terrace width (l) and the step height (a). During the crystal growth, the atoms are absorbed on terraces and then diffuse until they either desorb or attach to a step [73]. This growth mode is favorable for reducing the defects through the prevention of island formation and their coalescence [74], and also suppresses APD formation due to polar on nonpolar surface growth.

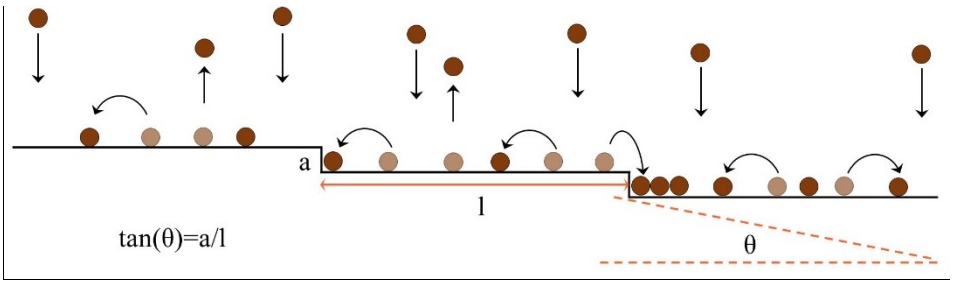

Figure 2.4. *Step flow growth on vicinal substrate surface.*

2.2. Challenges of Heteroepitaxial Growth of GaSb on Si

The growth of GaSb layer on Si substrate possesses structural problems. To overcome those difficulties is an essential challenge for cost effective Sb-based semiconductor device technology. The differences in material properties between GaSb

and Si are summarized in Table 2.1, where the crystal structure, the thermal expansion and the polarity shows discrepancy from each other. For this reason, in the grown GaSb buffer layer, the defects will be induced that can propagate up to the surface. It means that the Sb-based heterostructures grown on GaSb buffer layer would contain the defects, as well. Those deleterious defects will thus lead to the formation of deep level traps, the reduction in carrier lifetime and mobility in the device structure. The major challenging problems are lattice mismatch, thermal mismatch and incompatibility of the polar-non-polar interfaces and therefore, the GaSb layer grown on Si typically contains large defect density such as MTs or cracks, TDs and anti-phase domains (APDs).

Table 2.1. *Material properties of GaSb and Si [75].*

Property \ Semiconductor	Si	GaSb
Crystal structure	Diamond	Zinc Blende
Lattice constant (Å)	5.4310	6.0959
Thermal expansion coefficient at 300 K (K^{-1})	2.62×10^{-6}	6.35×10^{-6}
Band gap energy at 300 K (eV)	1.12	0.72
Band gap type	Indirect	Direct
Polarity	Non-polar	Polar

2.2.1. Large lattice mismatch

Considering to the growth of GaSb on Si substrate, the foremost challenge is to overcome the lattice mismatch issue. In the case of large difference in the lattice constants between the GaSb layer and Si substrate, a prominent strain is inevitable in the grown layer, resulting in the defect formation.

In epitaxial growth, the lattice mismatch between the layer and the substrate is given by,

$$f = \frac{a_l - a_s}{a_s} \tag{2.5}$$

where a_l and a_s are the layer and substrate lattice constant, respectively [76]. The strain arises from the lattice mismatch. Mostly biaxial strain is induced in the crystal lattice, meaning that it is introduced equally along two in-plane directions while the third (out-of-plane) direction is free to adopt where a and c represent in-plane and out-of-plane lattice constants, respectively [77]. When the lattice constant of the layer is smaller than

the lattice constant of the substrate, the in-plane of the lattice constant of the layer is experienced a tensile strain by the substrate. Alternatively, the layer with a larger lattice constant than the substrate undergoes a compressive strain in the in-place lattice constant by the substrate. In any case, the extent of the mismatch plays a fundamental role in heteroepitaxial growth.

For low mismatched system, 2% or less, the growth is initiated in Frank-van der Merwe mode. The overgrown layer can adopt the in-plane lattice constant. Namely, pseudomorphic growth occur where a strain arises at the interface (Figure 2.5). At this point, the strain energy is released in the grown layer following the atomic bond breaking at the interface above a certain critical thickness. During the relaxation of mismatch strain, the defects at the interface are introduced, called as misfit dislocations. This situation is illustrated schematically in Figure 2.5 for cubic lattice.

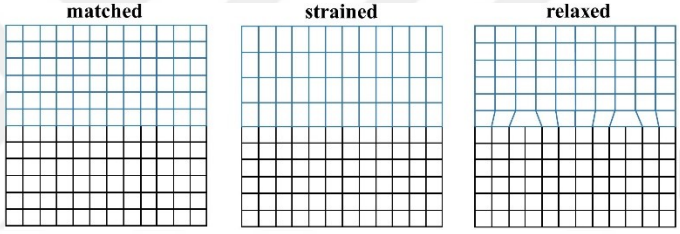

Figure 2.5. *Schematic illustration of lattice-matched layer, pseudomorphic layer and partially relaxed layer with a misfit dislocation in epitaxial growth.*

If the lattice mismatch is between 2% and 6%, the Stranski-Krastonov growth mode takes place and the critical thickness is defined as the wetting layer before the transition to 3D growth. The introduction of misfit dislocations becomes energetically favorable again depending on a certain size of the islands.

In the case of highly mismatched systems, larger than 6%, the Volmer-Weber growth will be dominant and 3D islands promptly form on the substrate without reaching a critical thickness, usually being at the order of one monolayer or less. By the island coalescence, a higher density of defects such as threading dislocations is expected for the grown layer. Hereby, there is a reasonable relationship between the lattice mismatch strain and the dislocation density.

Dislocations are called as line defects, causing the crystal lattice to distort along a dislocation line. The magnitude and direction of the lattice distortion is determined by Burgers vector via forming a closed path around dislocation line by atom to atom steps

(Figure 2.6(a)). If the same atom to atom path is applied to defect-free crystal lattice, the loop will fail and the closure failure is the Burgers vector of the dislocation (Figure 2.6(b)).

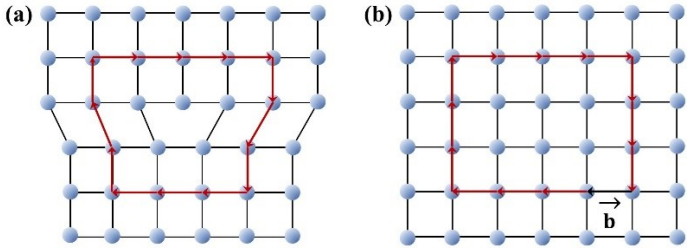

Figure 2.6. *(a) A closed loop around a dislocation and (b) the same atom to atom path in a defect-free crystal lattice; the black arrow indicates the Burgers vector.*

The dislocations occur in two basic form; the edge dislocations and the screw dislocations. Edge dislocation introduces a half extra (or missing) plane through the crystal lattice where the Burger vector is perpendicular to the dislocation line. If the plane of atoms trace a helical path, the dislocation is called as screw dislocation and its Burgers vector is parallel to the dislocation line. Besides, the dislocations also exhibit mixed character, resulting from a mixture of edge and screw dislocations with the Burgers vector inclined at an angle between 0^o - 90^o range to the dislocation line. For highly mismatched group III-V semiconductor growth, the most usually observed ones are 60^o and 90^o type misfit dislocations and are called Lomer dislocations [39, 78-79].

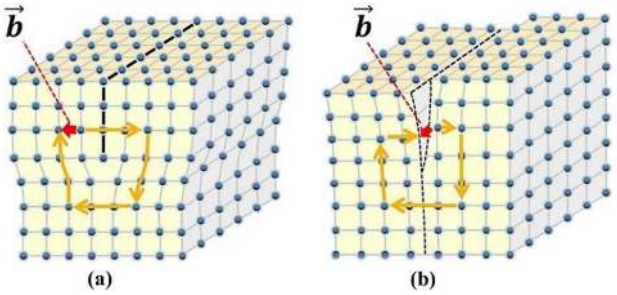

Figure 2.7. *Schematically illustration of (a) edge dislocation and (b) screw dislocation. The red arrows indicate the Burgers vectors.*

Threading dislocations, on the other hand, are caused by the misfit dislocations during the relaxation of the strain. In particular, they are propagating vertically through

the crystal lattice by breaking bonds. For this reason, threading dislocations act as non-radiative recombination centers, leading to a deterioration in device performance.

When the lattice mismatch between GaSb layer and Si (12.2%) is considered, a large strain will accommodated in the interface, promoting Volmer-Weber growth with the critical thickness of 2.043 Å for GaSb on Si [34]. Nowadays, a prevailing method applied is the growth of AlSb nucleation layer on Si substrate initially to enhance crystal imperfections in GaSb layer which was first promoted by Akahane *et.al*. [80]. Due to smaller diffusion length of Al compared to Ga on Si surface, more dense AlSb islands formation provides the reduction of the surface diffusion length of Ga atoms and act as nucleation sites for Ga and Sb species. Hence, the surface morphology of overlayers enhances [34]. Besides, AlSb/Si interface exhibits more regular misfit dislocation arrays, compared to GaSb/Si interface [36]. But yet, the threading dislocations and planar defects are still encountered in the GaSb epilayers even if AlSb islands are used.

2.2.2. Large thermal mismatch

The thermal expansion coefficient of the semiconductors is related to the expansion or contraction of the crystal lattice in response to a change in its temperature. In general, the lattice would expand at the higher temperatures and return to its original dimensions during reducing the temperature. If the layer and the substrate have different thermal expansion coefficients, the thermal mismatch occurs considering the gap in the temperature from the growth temperature to the ambient temperature. High thermal mismatch for group III-V/Si system can induce micro-crack or delamination in the grown layer, regarding to the order of the difference in the lattice mismatch between the layer and substrate. Assuming that the mismatched grown layer has fully relaxed at the elevated temperature, a tensile thermal strain ϵ_t will arise within the layer during the cooling process, which will be proportional to the overall temperature variation of the system:

$$\epsilon_t = \int_{T_o}^{T} [\alpha_s - \alpha_l] dT \tag{2.6}$$

where T and T_o are the final and initial growth temperatures, α_s and α_l are the temperature dependent thermal expansion coefficients of substrate and layer, respectively [81]. In this case, it is important to consider the grown layer thickness without any crack formation, called as the critical cracking thickness.

2.2.3. Incompatibility of the polar-non-polar surface

APBs are originated from the incompatibility of the polar and nonpolar surfaces between the substrate and the epilayer, which is typically encountered in the growth of group III-V on Si. Primarily, it is necessary to have knowledge about the crystal structure of the substrate and the grown epilayer in order to comprehend the formation of APBs. As shown in Figure 2.8(a), Si has a diamond structure, which comprises of two fcc sublattices displaced by $(1/4,1/4,1/4)a_o$ along the body diagonal with respect to each other. Whereas both sublattices are occupied by the same atomic species. Each Si atom forms four strictly covalent bonds with the neighboring atoms in a tetrahedral arrangement. In this case, the same charge distribution is exhibited between the constituent atoms, in other words, the atomic bonding exists with equal electronegativity. The elemental crystalline materials featuring this characteristic such as Si, Ge is called as non-polar semiconductors. Conversely, GaSb has a zinc blende structure in which the atomic position is the same as the diamond structure, but one fcc sublattice is comprised of Ga atoms and the other of Sb atoms (Figure 2.8(b)). Hence, the atomic arrangements of the atoms in the planes changes, such that the (111) surfaces contain either Ga or Sb atoms while the (110) surfaces have both Ga and Sb atoms, in addition the lattice lacks of inversion symmetry. The chemical bond between Ga and Sb atoms shows mixed covalent-ionic characteristics, leading the difference in the electronegativity, and so GaSb, GaAs etc. are polar semiconductors.

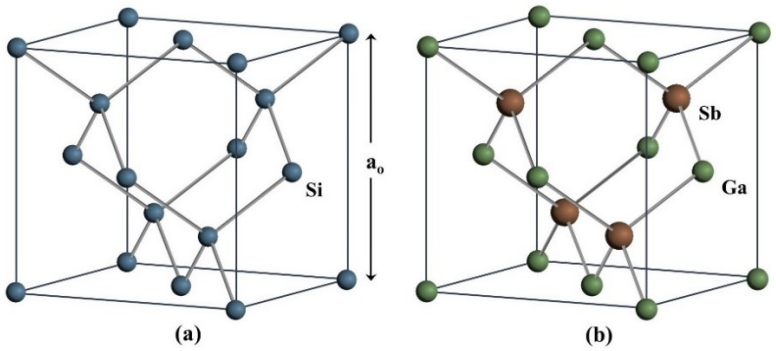

Figure 2.8. *Unit cell of (a) diamond structure Si and (b) zinc blende structure GaSb.*

Due to the dissimilarities in the polarity, APBs, which belongs to the planar defect family, can arise during the epitaxy of GaSb on Si. In the lattice with antiphase disorder, two nonequivalent orientations of sublattices occupied with the Ga atoms and the other

one, the Sb atoms, leads to the reverse of crystal polarity and bonding directionality. This anti-phase regions having opposing sublattices are called as APDs and the interface between domains forms APBs, which are electrically active defects, acting as non-radiative recombination centers and leakage paths in optoelectronic devices.

Surface steps with atomic height is the inherent characteristic of a real Si (100) surface, which can exhibits single or double steps [11]. The most common step height is single atomic layer for a typical Si (100) wafer. In this case, the formation of APDs and APBs is inevitable in the growth of group III-V on Si. As an example of GaSb epilayer grown on Si (100) surface with single step, the domain regions occur above the surface step by reversing the polarity of the crystal and the two group III-V domains is separated by a plane of alternating Ga-Ga and Sb-Sb anti-site bonds, referring to an APB, as shown in Figure 2.9. In the event of the growth on Si (100) substrate having double steps surface, the orientation of the sublattices doesn't reversed and the presence of double atomic height steps inhibits the occurrence of APBs [82].

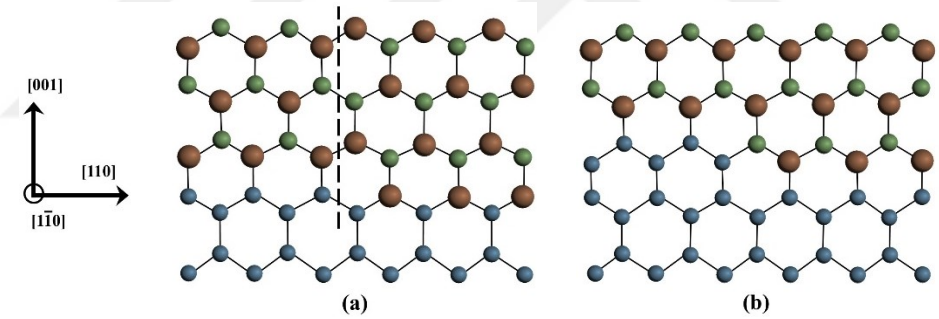

Figure 2.9. *(a) APBs in GaSb formed by a single step on the Si substrate and (b) suppression APBs in GaSb epilayer by featuring double step on the Si substrate surface.*

APBs can be classified depending on the nature of antisite disorder. While the stoichiometric APBs occur on {110} and {211} planes with equal number of antisite bonds of groups III-III and V-V, the non-stoichiometric type on {113} planes contain an unequal mixture of both groups III-III and V-V bonds. Besides, APBs on {100} and {111} planes are comprised of the same antisite bonds, i.e. group III-III or group V-V bonds. Calculations of the formation energy of APBs suggest that the APBs along the {110} plane have the lowest formation energy. In addition, an APB may self-annihilate with another APB in some way. The annihilation of APBs occur between the APBs on {110} planes or {111} planes as well as self-annihilation which is based on

kinking over from {110} by faceting to higher index planes such as {112}, {113}, as shown in Figure 2.10. By this way, the suppression of APBs is able to be achieved for polar group III-V epilayers grown on non-polar substrates [83].

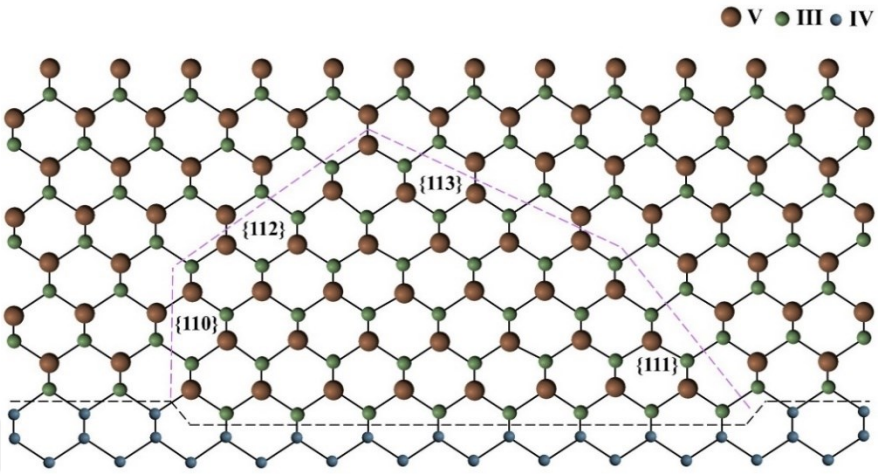

Figure 2.10. *Self-annihilation of an APB by kinking to higher index planes.*

For suppression of APBs, some methods are executed such as the growth of group III-V epilayers on a reconstructed Si surface with double atomic steps, the utilization of misorientated or (211) orientated Si substrates [84-85] and the initiation of either group III or V prelayer on Si substrate for a precise time in order to cover the surface by a monolayer before starting the growth [86]. Among those, the most common application is the Si (100) wafers deliberately tilted a few degrees (0.15°-6°) off the (110) plane, which are termed as vicinal substrates. The off-cut Si (100) substrates introduce regular array of steps with higher density, and when the off-cut angle is increased, the distance between terraces is decreased, thus the step density increases. Thus, the self-annihilation of APBs has been observed for the grown epilayers on vicinal Si (100) substrates [85]. Furthermore, the vicinal substrates pre-heated at high temperatures (up to 1000 °C) under ultra-high vacuum environment, exhibit higher percentages of double step surfaces, leading APB suppression. Besides, double step surface on nominal Si substrates is achievable with high temperature pre-heating for a long period of time [87].

2.2.4. Other type of defects

Other type of planar defects happened during the highly mismatched growth are SFs and MTs. A perfect crystal consists of a stack atomic layers in a particular sequence.

As shown in Figure 2.11, the stacking sequence of the zinc blende structure in the [111] direction is described by using …ABCABC… stacking notation (each letter represent a monolayer). If this regular arrangement of atomic layers are altered, a stacking fault occurs by inserting an extra plane of atoms into the stacking sequence (…ABCBABC….) or by removing a plane of atoms (…ABCBCABC….), which are called as extrinsic and intrinsic stacking faults, respectively (Figure 2.12(b) and (c)). On the other hand, in the case of a reflection of the stacking of planes in the [111] direction, twinning occurs. Basically, twinning can be denoted by …ABC**A**CBA… stacking notation, where the bold marked A is a twin plane. Here, a mirror image of the parent crystal is created by changing the crystal orientation across the twin plane, as presented in Figure 2.12(d). The formation of stacking faults and micro twins is associated with the initial nucleation of growth processes, in contrast to deformation related to the lattice mismatch and the thermal stress.

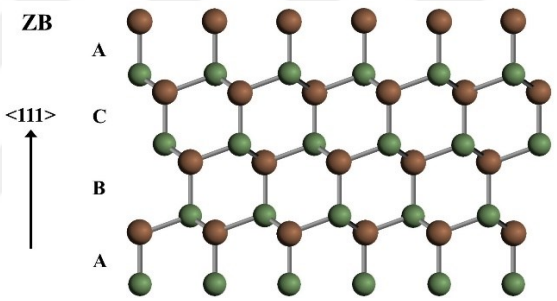

Figure 2.11. *A schematic representation of stacking sequences of ZB structure.*

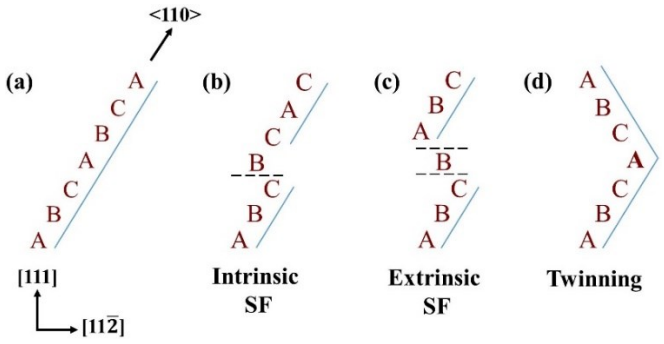

Figure 2.12. *A schematic representation of (a) perfect ABC stacking sequence (ZB), (b) stacking sequence with intrinsic SF, (c) extrinsic SF and (d) a twin boundary.*

2.3. Nanowire Growth Mechanism

The most common method for the nanowire synthesis by the bottom-up approach is VLS mechanism, proposed firstly by Wagner and Ellis in 1964 to grow Si whiskers using chemical vapor deposition [88]. The VLS mechanism involves three phases: Vapor-phase precursor, liquid-phase metal catalyst and solid-phase crystallization. In this method, a metal seed acting as a catalyzer is deposited on the substrate whose temperature is kept above the eutectic temperature of the metal. By exposing the source materials in the vapor phase, a liquid-alloy is formed in consequence of the interaction with catalyzer. With the continuous treatment of materials in vapor phase, the catalyzer reaches supersaturation and the nanowire growth starts at the interface of the liquid-alloy and substrate (Figure 2.13).

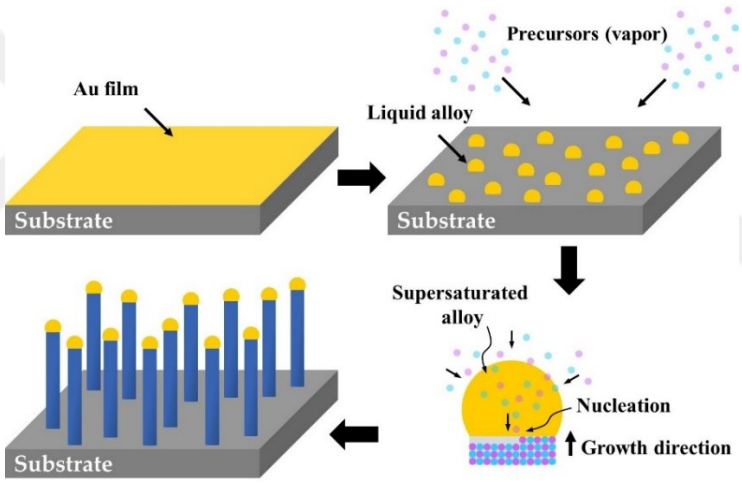

Figure 2.13. *Schematic illustration of the VLS growth mechanism.*

In the VLS method used for the growth of group III-V semiconductor NWs, Au is usually used as a metal seed. Although Au is a non-oxidized element and formed in smaller sizes easily, they can penetrate through the nanowire. Hence, it causes the deep level traps [89] which reduce the optical and electrical quality of the NW structures. To overcome this problem, self-assisted method is introduced for the growth of III-V semiconductor NWs [90]. Namely, group III elements is used as a catalyzer in this method, instead of a foreign metal catalyzer. In this study, GaAs nanowires were grown on GaAs substrates coated with a thin layer of SiO_2. It was demonstrated that Ga atoms form liquid droplets on the SiO_2 surface and they create pinholes as a result of the interaction with SiO_2. Then, being similar to Au-catalyzed VLS growth, GaAs NWs

can grow below the droplets on the surface of Si substrate, during the introduction of Ga and As precursors. In the meantime, the studies demonstrated the growth of GaAs NWs on Si (111) substrates with native oxide or SiO_2 layer prepared dedicatedly and SiO_2 masked Si (111) substrates [65, 91-92]. A schematic view of self-assisted growth of GaAs NWs on Si (111) is presented in Figure 2.14. Ga atoms was deposited on the Si (111) substrate to form the droplets for a short period of time. Hence, the contact of Ga droplets on Si substrates is occurred. Subsequently, As flux is supplied and the initiation of GaAs NWs begins from the liquid-solid interface in the wake of the supersaturation of Ga droplets with As.

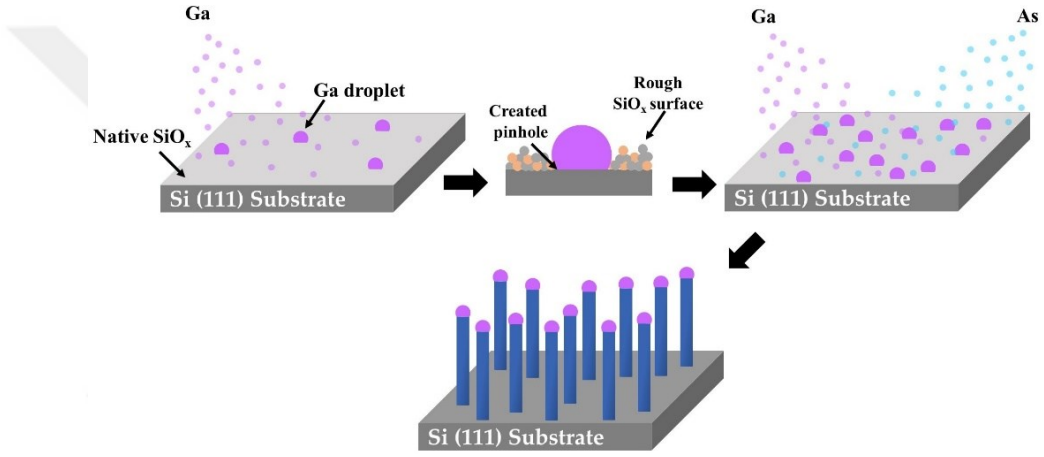

Figure 2.14. *Schematic illustration of self-assisted GaAs NWs on Si (111) substrate.*

2.3.1. Zinc blende-wurtzite polytypism

Polytypism is the co-existence of the different crystal phases. The crystal structure of the most III-V semiconductors is zinc blende in bulk form at ambient conditions. However, group III-V NWs present polytypic behavior, involving ZB and WZ crystal phases which differ their stacking sequences. As shown in Figure 2.15, the stacking sequences of Ga-As bilayers in the zone axis (110) for cubic ZB and (1120) for hexagonal WZ is described as ABCABCABC and ABABAB, respectively. Hence, polytypism is observed frequently in the growth of GaAs NWs due to kinetic reasons [93].

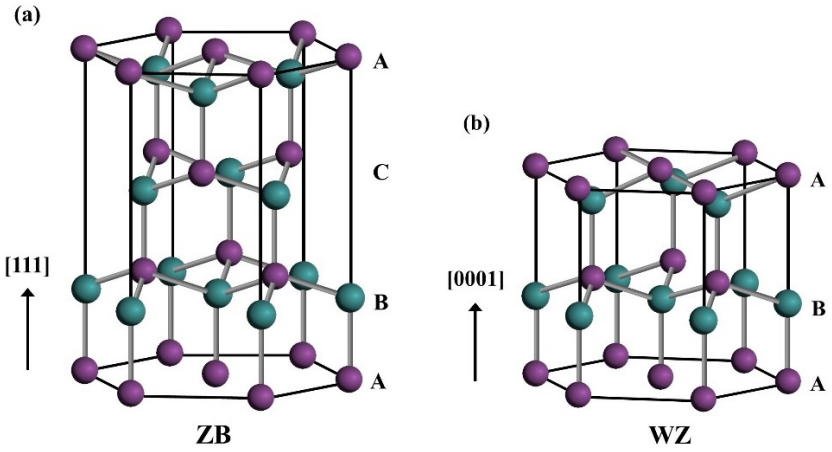

Figure 2.15. *Crystal structure of (a) ZB and (b) WZ GaAs: ..ABCABC.. and ..ABAB.. demonstrate stacking sequences, respectively.*

The band gap of WZ GaAs is 35 meV above the band gap of ZB GaAs [94]. Hence, considering the band alignment, unregularly arrangement of WZ/ZB phase may affect the optical and electronic properties of the NWs in device applications. Therefore, it is important to control the crystal phase of the NWs and pure phase NWs or ZB/WZ SL NWs is in prospect. Another object of concern is the formation of defects such as SFs and twinning during the growth of NWs. Similarly, the extent of the defects can affect the device functionalities. Ultimately, it is essential to understand the growth dynamic of NWs and focus to optimize the growth parameters for high quality NW based future devices.

3. EXPERIMENTAL METHODS AND DETAILS

3.1. Molecular Beam Epitaxy

MBE is an epitaxial growth technique that carries out the formation of crystalline homoepitaxial or heteroepitaxial layers on a crystalline substrate in ultra-high vacuum (UHV) conditions with precision epilayer thickness control. A basic MBE system is made of stainless steel chamber equipped with effusion cells, vacuum pumps, surface analysis tools, mass spectroscopy and temperature sensors. While a wide range of various materials including oxides, semiconductors, and metals are grown via MBE systems, this technique offers a particular possibility to process low dimensional structures as well.

A new electronic age had begun with the invention of the transistor [95]. As required by circumstances, producing high quality crystals and smaller devices gained importance and hence that created a need in the crystal growth technology. MBE was first introduced in the late 1960s by J. R. Arthur and A. Y. Cho with the works based on GaAs compound semiconductors [96]. It has become highly developed as well as flexible tool, meanwhile, has made the process of unique physical structures possible. As a consequence, it plays an unavoidable role in the contribution of nanotechnology progress [97].

A basic MBE system is presented in Figure 3.1. The fundamental requirements of an MBE system are to obtain high quality materials; therefore UHV condition ($\sim 10^{-11}$ Torr for background pressure) is required and it is provided by ion pumps and/or cryo pumps in order to keep the chamber environment clean and minimize contamination during the growth process. Besides, the growth chamber itself with liquid nitrogen filled shroud contributes to enhance the vacuum level. Residual gases are also monitored by residual gas analyzer (RGA) to assist the control of ambient growth chamber. Ultra-high purity materials are loaded in crucibles inside the effusion cells equipped with shutters and sublimated or evaporated through the orifice of the crucible by heating the crucibles. The beam flux is controlled with the shutters where the operation time is ~0.1 s. Hence, the low growth rates (<1 ML/s) and precision composition control is achievable conveniently [98]. The flux ratios and growth rates are determined by beam flux monitor (BFM) gauges located at the substrate heater position. Before the growth process, the beam flux of source material depending on the effusion cell temperature is measured by BFM gauge. Then, the substrate loaded to the substrate heater is heated up to a proper

temperature, as well as the effusion cells. By opening the shutters, the atoms or molecules impinge on the surface and proceed to physical and chemical reactions on the surface leading the crystallization process under proper growth conditions (background vacuum level, the beam flux ratio and the substrate temperature). During the growth process, the temperature of substrate is monitored by the substrate heater's thermocouples and non-contact temperature sensors (Pyrometer or band-edge thermometry). One of the essential tool is reflection high-energy electron diffraction (RHEED) for monitoring the growth process in real time. RHEED is based on the reflection with grazing incidence angle of the electron beams from the surface atoms. Thus, it enables to ascertain the surface crystal information at atomic levels, the growth modes and also, measures the growth rates.

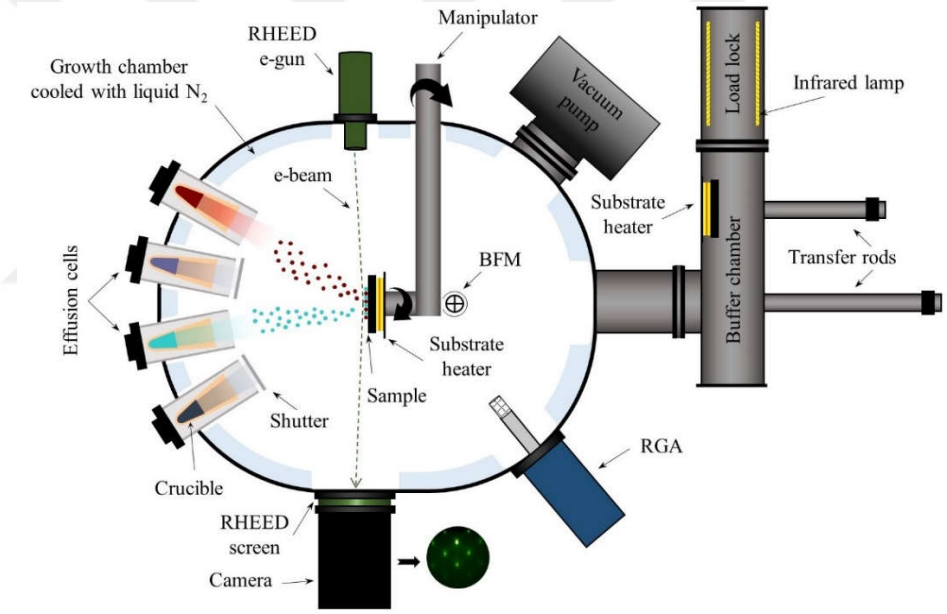

Figure 3.1. *Basic schematic illustration of an MBE system.*

In this study, all samples were grown by using Veeco GEN20MC solid-source MBE system equipped with valved antimony (Sb), arsenic (As) cracker cells and gallium (Ga), aluminum (Al) dual filament cells. As_2 and As_4 were used as group-V uxes by keeping the cracker temperature at 900 or 625 ºC, respectively and the cracker temperature for Sb_2 was 900 °C. The beam equivalent pressure (BEP) was measured by an ionization gauge at the back of the substrate manipulator, when it was rotated into the direct beam path. The base pressure of the MBE system was $7x10^{-11}$ Torr at the standby temperature of the effusion cells. The substrate temperature was monitored by using an IRCON

pyrometer which was calibrated against the GaSb (1×3) → (2×5) surface reconstruction transition [99].

GaSb buffer layers were grown on nominal Si (100) substrates and vicinal Si (100) substrates with different miscut angles towards [110] direction. For all sets, the Ga flux was set to a BEP of $7.4x10^{-8}$ Torr, corresponding to a growth rate of 0.5 ML/s and the group V/III ratio was kept at 10. Prior to the growth, the Si substrates were loaded to the load-lock chamber of the MBE and baked at 150 ºC for 1 h under a minimum vacuum level of $1x10^{-7}$ Torr. After transferring to the buffer chamber, each substrate was degassed at 400 ºC separately by probing a minimum vacuum level of $2x10^{-8}$ Torr. In the growth chamber, native oxide was desorbed from the Si substrate's surface at 850 ºC and the desorption process was verified by RHEED patterns. Following oxide desorption, the Si substrate was reduced to the growth temperature and exposed to the Sb flux (BEP: $1.6x10^{-7}$ Torr) for 5 min.

For GaSb epilayers with AlSb NL, the ratio of Sb flux to Al flux was kept at 50 and the Al flux BEP was $6.2x10^{-9}$ Torr. The AlSb NLs were deposited with a growth rate of 0.1 ML/s at 485 ºC on nominal Si substrates. To understand the effect of AlSb NL thickness on the crystal quality of GaSb epilayer five different thicknesses between 5-80 ML were used (Set 1). For the GaSb epilayer, the temperature was increased to 530 ºC under Sb flux and Ga shutter was open to start 1 µm thick non-intentionally doped GaSb epilayer. For an AlSb NL thickness of 20 ML, two additional growth temperatures (at 550 and 570 ºC; Set 2) and three different post-growth annealing temperatures and durations (at 550, 570 and 590 ºC for 30 min and at 570 ºC for 30 min, 60 min, 120 min; Set 3) were applied to investigate the influence of growth temperature and post annealing on the GaSb epilayer crystal quality. The samples were exposed to Sb flux (BEP: $7.8x10^{-7}$ Torr) during the post annealing.

GaSb epilayers with GaSb NL were grown on nominal Si substrates. For GaSb NL, the Sb/Ga flux ratio was kept at 5 and the Ga flux BEP was $2.7x10^{-8}$ Torr. For the determination of favorable growth parameters, the GaSb NL with a growth rate of 0.1 ML/s was initiated with different thicknesses (2, 20, 40, 80 ML; Set 4) and at different growth temperatures (350, 400, 450, 500 ºC for 40 ML thick GaSb NL; Set 5). Subsequently, 1 µm thick GaSb epilayers were grown at 530 ºC on the Si/GaSb NL.

In addition, GaSb epilayers with AlSb NL were grown on Si substrates with off-cut (miscut) angles 0.15, 2, 4 and 6º to examine the influence of misorientated substrate on

the epilayers (Set 6). For the inhibition of the defects propagating through the epilayer, the growth of GaSb buffer layers consisting of GaSb/AlSb superlattices (SLs) was applied on nominal Si substrates (Set 7). The SL growth rate was set at 0.5 ML/s for both GaSb and AlSb (the Al BEP flux was 6.6×10^{-8} Torr). For comparison, the growth parameters of the GaSb epilayer grown at 530 ºC with 20 ML thick AlSb NL were applied for the samples in Set 6 and Set 7.

Self-assisted VLS growth of GaAs NWs were performed on (111) orientated Si substrates. After degassing in the load-lock and buffer chambers (150 and 400 ºC, respectively), the Si substrate was transferred and heated up to the desired temperature in the growth chamber. First, Ga was deposited for 30 s to form the droplets on the native oxide layer. Following Ga deposition, As shutter was opened to initiate GaAs NWs. The As_4/Ga flux ratio was 20 and the growth rate was 0.8 ML/s, corresponding to a 2D growth rate. The GaAs NWs were grown at three different growth temperatures (580, 600 and 620 ºC; Set 8) for 30 min. For Set 9, the growth temperature and duration was kept at 580 ºC and 20 min. Two different Ga growth rates (0.25 or 0.65 ML/s) and group III/V flux ratios (20 or 80) were used for the growth of three samples in Set 9. During the cooling process, the substrate temperature was reduced rapidly and As shutter was closed at 500 ºC.

3.2. Scanning Electron Microscope

SEM is a type of imaging tool for the surface morphology and chemical composition analysis of the specimens. As the specimen is exposed to the electron beam which contains electrons having much shorter wavelengths compared to the visible photons' wavelengths, SEM can reach to a resolution of ~2 nm which provides 100 times greater resolution with respect to the optical microscope. The electron beam, of which accelerating voltage varies between 1-30 keV, is generated by a thermionic filament or a field emission gun. Electromagnetic lenses are used to focus the beam, which is scanned over the surface of the specimen with scanning coils in a raster pattern. Then, the signals as a consequence of the interaction of beam with the specimen is collected by specific detectors. The instrument is kept under vacuum for preventing the beam scattering and the electron gun damage (Figure 3.2).

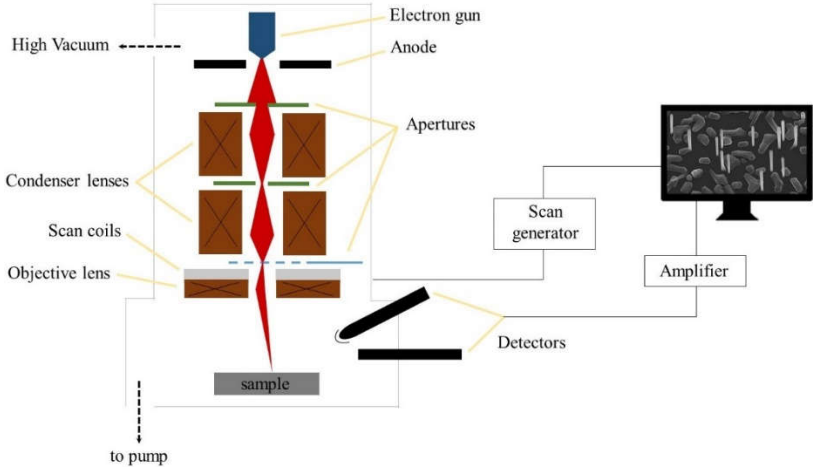

Figure 3.2. *Schematic diagram of an SEM.*

When the specimen is illuminated with the focused beam, the primary electrons interacts with the matter, as summarized in Figure 3.3 [100]. Secondary and backscattered electrons are the signals used for imaging in SEM. Secondary electrons are produced from the near surface as a result of inelastic collisions of the primary electrons with the shell electrons, and give topographical/morphological information. The interaction of the primary electrons with the nucleus of the atoms produce the backscattered electrons which lose only small portion of their energy or none since they have higher kinetic energy than secondary electrons. Topographical contrast and compositional information is obtained with the emitted backscattered electrons. Mainly used secondary and backscattered electrons are detected by Everhart-Thornley and solid state backscatter electron detectors, respectively. Another type of data is X-ray signals which is emitted to balance the energy difference when one of the electron in the beam ejects an inner shell electron of the specimen and an outer shell electron fills the missing electron position. Thus, qualitative and semi-quantitative elemental analysis is performed through energy dispersive spectroscopy (EDS) by using characteristic X-rays.

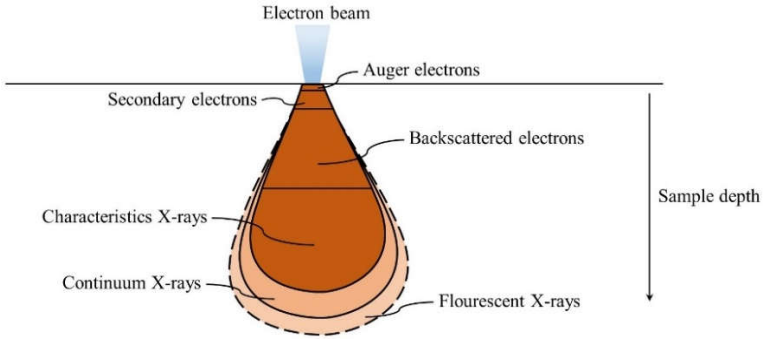

Figure 3.3. *The signals generated by electron-matter interaction in the SEM.*

The surface morphologies of the samples were investigated using ZEISS model ULTRAplus field emission scanning electron microscopy (FE-SEM) equipped with EDS (EDAX/AMETEK materials analysis division) for elemental analysis. An electron gun potential of 15 kV was employed and the images were taken using the Everhart-Thornley and in-lens detector for the GaSb epilayers and the GaAs NWs, respectively. The images were collected with a tilt angle of 20^{o} for the GaAs NWs. Also, the cleaved GaAs NW samples were placed in isopropyl alcohol (IPA) and were removed from the growth substrates via sonication. Then, the GaAs NWs suspended in IPA were transferred on a Si wafer with the micropipettes. By this way, the SEM images of the individual GaAs NWs were obtained.

3.3. Transmission Electron Microscope

TEM having similar configuration as in SEM, is a vital tool for the imaging of the materials in atomic scales. The significant distinctive features of TEM are high accelerating voltage electron beams, using the transmitted electrons and very thin specimens. TEM typically operates at high voltages between 100 and 300 kV. In microscope column, the accelerated electron beam is focused by electromagnetic lenses and illuminates the specimen placed in the middle of the column. As a result of the interaction of electrons and specimen based on the diffraction phenomena, a magnified image is projected through electromagnetic lenses onto a CCD camera or phosphorous screen. Therefore, the specimen should be enough transparent to the incident electrons for TEM investigations. Since the electron transparency of the specimen depends on the accelerating voltage, its average atomic number and the desired features to be resolved, obviously “thin” is a relative term. Typically, the thickness of the specimen

should be 100 nm or less [101]. Therefore, in general, a complex sample preparation process is required for epitaxial structures grown on wafers. On the other hand, for NWs, electron transparency is a natural fact due to their low dimensions, in most cases. Nevertheless, TEM allows a greater resolution/magnification imaging and provides the structural examination of the crystals and the analysis of chemical composition via various operation modes.

For the sample preparation, GaAs NWs is removed from the Si (111) substrates as previously described in Section 3.2 and then NWs dispersed in IPA were transferred onto the lacey or holey carbon grids (300 mesh) depending on the lengths of NWs. As presented in Figure 3.4., the grid is made of copper and coated with a fine layer of carbon having random holes. Lacey and holey terms describe the extent of open areas of the carbon layer.

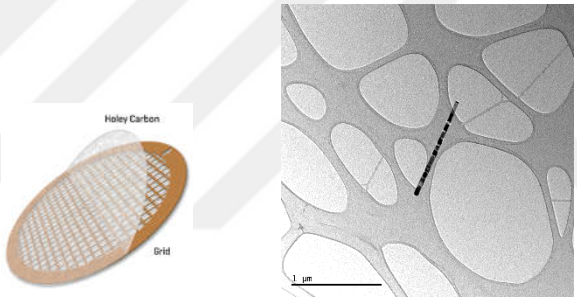

Figure 3.4. *(a) Picture of a holey carbon grid and (b) TEM image of GaAs NW suspended on holey carbon film.*

TEM images and EDS spectra of GaAs NWs (Set 8) were taken by JEOL ARM200F HRTEM equipped with selected area electron diffracton (SAED) and JEOL Centrio Dry SD100GC SDD Detector. The GaAs NWs in Set 9 are examined by JEOL 2100 JEM HRTEM for high resolution imaging and the crystal analysis. EDS analysis is performed by Oxford Instruments X-Max 80 Aztec system.

3.4. Atomic Force Microscopy

AFM is a type of scanning probe microscopy for surface imaging of a wide variety of materials. The topographic and morphologic information is fundamentally attained from Coulombic and van der Waals interactions between the probe and the surface atoms. The AFM probe consists of a sharp tip at the end of a microfabricated flexible cantilever.

The cantilever is mainly made of silicon or silicon nitrite with the tip in the range of 5-20 nm end radius. The attractive and repulsive forces between the tip and the surface atoms produce the cantilever deflections. By this way, the angular deflection of the cantilever is perceived by the differences at the position of the laser beam which is reflected from the back of the cantilever to a photodiode. The probe and the sample is mounted on a piezo positioners which allow the probe performing a raster scan across the surface. Thus, the detected signals are converted into a 2D or 3D surface image (Figure 3.5).

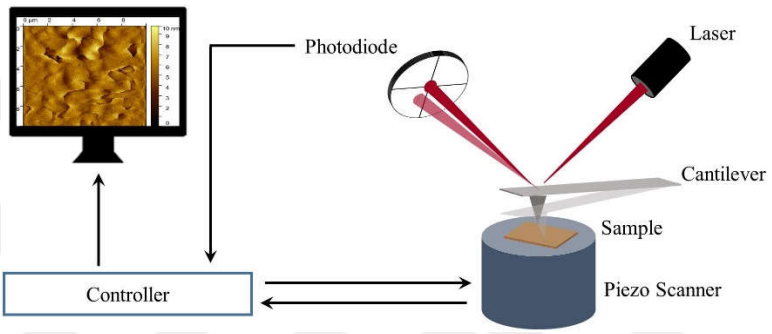

Figure 3.5. *Basic schematic diagram of an AFM.*

AFM can be operated in three different modes, as shown in Figure 3.6 [102]. In the contact mode, the probe is softly in physical contact with the surface so that the repulsive forces are measured. High scan speed and high resolution imaging is achievable with this mode. In the non-contact mode, the cantilever is oscillated near its resonant frequency without the tip touching to the surface. The frequency deviation is measured as a consequence of attractive forces. Therefore, this mode can be used for very soft materials and provides extended probe lifetime. Tapping mode is also called semi-contact mode. The cantilever is oscillated at its frequency that the tip slightly taps to the surface during the scan. Improved lateral resolution images can be obtained compared to the contact and the non-contact modes. Also, the reduction in the applied force results in less damage in soft material as well as tip.

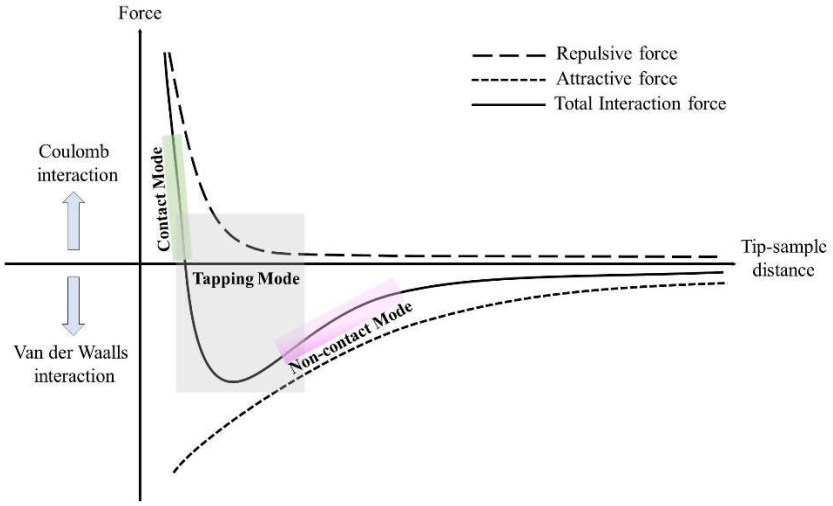

Figure 3.6. *Interaction force versus distance between AFM tip and sample surface.*

The surface roughness of the GaSb samples was measured by NT-MDT NANOEDUCATOR II model AFM in semi-contact mode with aluminum coated silicon nitride tip of below 10 nm. The RMS values were obtained from the areas of 25 or 100 μm^2.

3.5. Photoluminescence

PL is a nondestructive method to investigate the electronic structure of the materials. The material is illuminated with an external source, usually a laser, and this process is called photo-excitation. The absorbed photons excite the carriers within the material to the allowed electronic states and then the excess energy is released as photon emission while the carriers returning to their equilibrium states.

PL spectroscopy is a fundamental method due to the ability to provide worthful information about the semiconductors via optical process. The excitation with a laser beam whose energy much larger than the band gap generates electron-hole pairs by driving valance band electrons to the conduction band (Figure 3.7). While releasing the excess energy, the radiative and non-radiative recombination transitions in a variety of paths occurs depending on the structure and properties of the semiconductors. By this way, the information such as band gap energy, impurity and defect levels as well as alloy concentrations can be obtained in order to gain insight into the semiconductor properties.

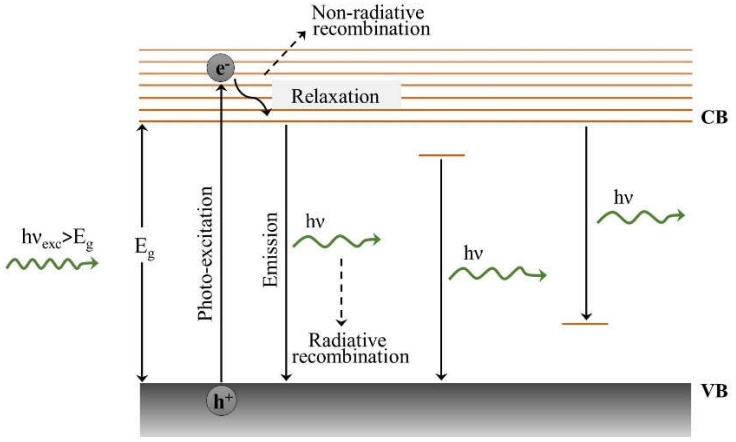

Figure 3.7. *Schematically illustrated basic PL processes in a semiconductor.*

In this study, the PL measurements of GaSb samples were carried out by using a Bruker Vertex 80 V Fourier transform infrared spectrometer. The samples were mounted in a closed-cycle helium cooled cryostat and were excited at 10 K using a 532 nm continuous wave laser which has a penetration depth of 26 nm for GaSb. The PL signals were detected by an InGaAs detector.

3.6. X-ray Diffraction

X-ray diffraction based on the interference of scattered X-rays by the atoms, is a non-destructive and very handy method to analyze the crystalline materials comprehensively. For semiconductor heterostructures, substantial information is provided including crystal quality, lattice strain-stress, dislocation density, surface and interface roughness, layer composition and thickness [103].

In a crystalline material, the atoms are packed in regularly and periodically in all three dimensions. The periodicity of the atoms is described by a network in space where array of each point represents atom positions and has identical surroundings. This is called space lattice and the lattice planes are specified by Miller indices (h, k, l). When a monochromatic coherent beam such as X-ray with a wavelength comparable to the atomic distance in the crystal strikes the atoms of the crystal planes, the coherent and incoherent scatterings occur. If the reflected beam interferes constructively where the path length difference is an integer number of the wavelength, the diffraction occurs as shown in Figure 3.8 and it is expressed by Bragg's law [104]:

$$n\lambda = 2d_{hkl}\sin\theta \tag{3.1}$$

where n is an integer representing the order of diffraction, λ is the wavelength, d_{hkl} is the lattice plane spacing and θ is the angle between the incident beam and the diffracted beam. Hence, a certain intense Bragg peak is produced by the diffraction and contains the information about the atomic ordering within the crystal, which means that either the crystal quality or the perturbation in the crystal structure can be investigated by evaluating the shape, broadening and the position of the Bragg peak.

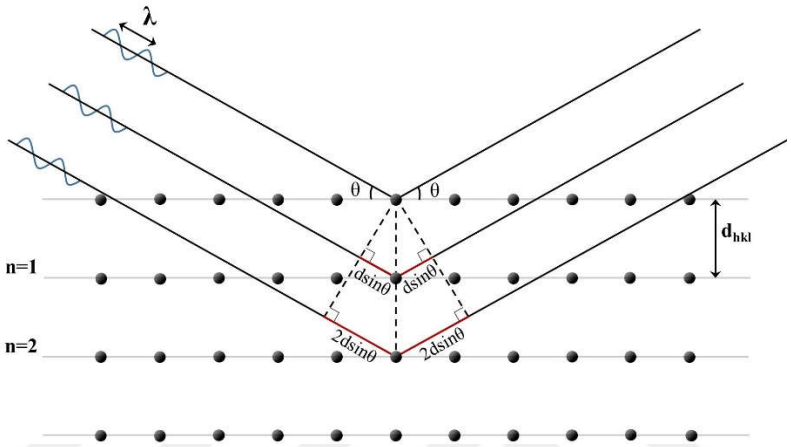

Figure 3.8. *Schematic representation of X-ray diffraction in a crystal.*

In order to determine the structural properties of the GaSb epilayer, high resolution X-ray diffraction (HRXRD) rocking curve (RC) measurements were performed by PANalytical X'Pert Pro MRD system equipped with parabolic W/Si mirror, a four bounce (Ge220) symmetric monochromator and a Pixcel detector using Cu $K_{\alpha 1}$ radiation (λ= 0.15406 nm). Omega RCs were measured via the symmetrical (004) GaSb reflection. The TD density of the samples were also determined by using the X-ray RCs as described in Ref [105].

4. GROWTH OF GaSb ON Si (100) VIA AlSb NUCLEATION LAYER

4.1. Introduction

In this chapter, the growth of GaSb epilayers on Si (100) via AlSb NL are presented. A series of samples were grown to investigate the effect of AlSb NL thickness, the growth temperature, the post-growth annealing temperature and duration on the surface morphology, structural and optical properties of the GaSb epilayers. The crystal quality of the epilayers were determined by HRXRD RCs measurements. SEM analysis and AFM measurements were performed for the surface morphology observation. The optical properties were investigated by PL measurements.

For all samples, the growth parameters including Al/Sb flux ratio (50), the growth temperature of the AlSb NL (485 ºC) and Sb/Ga flux ratio (10) and GaSb epilayer thickness (1 μm) were kept identical. To understand the effect of AlSb NL thickness on the crystal quality of GaSb epilayer, five different thicknesses were used (Set 1). After determining the optimum AlSb NL thickness, two additional growth temperatures (Set 2) and three different post-growth annealing temperatures and durations (Set 3) were performed to examine the influence of the growth temperature and post-growth annealing on the GaSb epilayer crystal quality. The growth parameters of Set 1, Set 2 and Set 3 are summarized in Table 4.1, Table 4.2 and Table 4.3, respectively. NB1-3 would be the reference sample for comparison purposes after the optimization of AlSb NL thickness.

Table 4.1. *Growth parameters for the samples in Set 1.*

Sample Code		NB1-1	NB1-2	NB1-3	NB1-4	NB1-5
AlSb	**Thickness (ML)**	5	10	20	40	80
GaSb	**Growth Temperature (ºC)**	530	530	530	530	530

Table 4.2. *Growth parameters for the samples in Set 2.*

Sample Code		NB1-3	NB2-1	NB2-2
AlSb	**Thickness (ML)**	20	20	20
GaSb	**Growth Temperature (ºC)**	530	550	570

Table 4.3. *Growth parameters for the samples in Set 3.*

Sample Code		NB1-3	NB3-1	NB3-2	NB3-3	NB3-4	NB3-5
AlSb	**Thickness (ML)**	20	20	20	20	20	20
GaSb	**Growth Temperature (°C)**	530	530	530	530	530	530
Post-growth annealing	**Temperature (°C)**	None	550	570	590	570	570
	Time (min)	None	30	30	30	60	120

4.2. The Effect of AlSb Nucleation Layer Thickness

As a beginning, the RHEED patterns were recorded to explore the structure of AlSb NL surfaces. For AlSb NL with thicknesses between 5-40 ML, the spotty patterns indicating 3D island nucleation [106] were monitored on RHEED screen during the growth and the RHEED pattern for 20 ML thick AlSb NL is shown representatively in Figure 4.1(a). Also, the SEM image representing AlSb islands in Figure 4.1(d) was taken from 20 ML thick AlSb NL for the purpose of better understanding of AlSb NL. Unlike the others, the transformation of RHEED pattern from spotty to streaky was observed towards the end of the growth of AlSb NL with thickness of 80 ML, indicating the island coalescence with the appearance of a streaky (1x3) AlSb reconstructed surface (Figure 4.1(b)). After the initiation of AlSb NL, the clear streaky (1x3) pattern was appeared within 4-7 minutes (corresponding the GaSb thickness between 45-65 nm) during the growth of GaSb epilayer samples (Figure 4.1(c)).

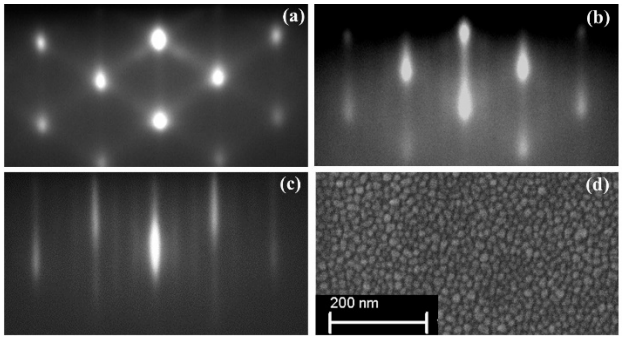

Figure 4.1. *RHEED patterns at the [110] azimuth (a) during the growth of AlSb NL with thickness of 20 ML indicating 3D island nucleation, (b) towards to the end of the growth of AlSb NL with thickness of 80 ML which indicates the island coalescence, (c) during the growth of GaSb epilayer representing (1x3) reconstructed surface and (d) the SEM image of AlSb NL with thickness of 20 ML.*

To understand the structural quality, the samples were investigated by HRXRD. The FWHM values were extracted from HRXRD RCs for each sample and presented in Figure 4.2. It was observed that depending on the AlSb NL thickness, the FWHM values of the GaSb epilayers show variations. Among all the samples in this set, the sample NB1-3 depicts the best FWHM with 302 arcsec which corresponds to an AlSb NL thickness of 20 ML. It seems that, up to 20 ML thick AlSb NL, the FWHM value of the GaSb epilayer improves as a function of it. However, above that thickness, the FWHM value of the GaSb epilayer worsens and it reaches 374 arcsec for an AlSb NL thickness of 80 ML. The TD density of the samples were also determined by using the X-ray RCs as described in Ref [102]. As can be seen from Figure 4.2, all the samples have TD densities at the order of 10^8 cm^{-2} and the best value in this set belongs to the sample NB1-3 with a value of 3.09×10^8 cm^{-2}.

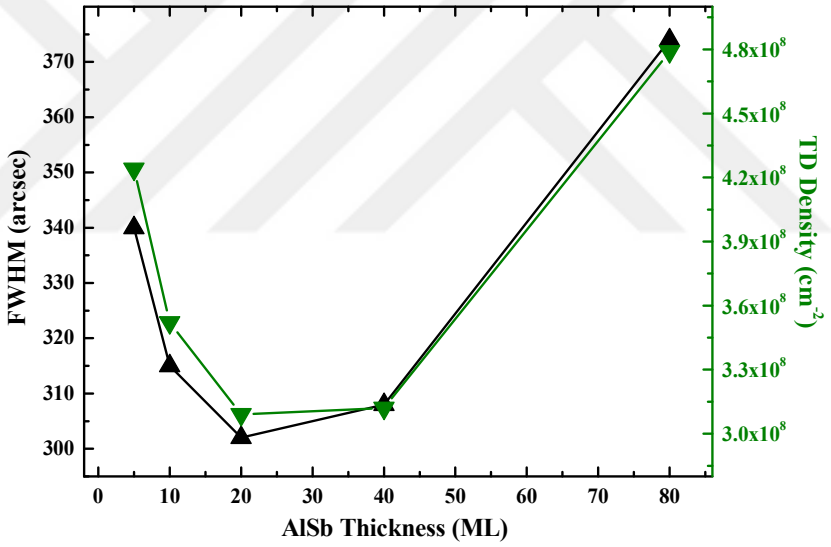

Figure 4.2. *The FWHM of X-ray RC around the (004) reflection and the TD density of GaSb epilayers as a function of AlSb NL thickness.*

Due to the fact that GaSb on Si is aimed to be used as a substrate-like structure for GaSb based devices, the morphology and the surface roughness of the epilayer is crucial. To this purpose, the root mean square roughness (RMS) and the peak-to-valley height (PV) of the surfaces were determined the AFM images and presented in Figure 4.3. As can be seen, NB1-1, NB1-2 and NB1-3 have an RMS values which is better than the RMS value of the samples NB1-4 and NB1-5. Besides, the best PV value was obtained for the sample NB1-3 as 9.77 nm.

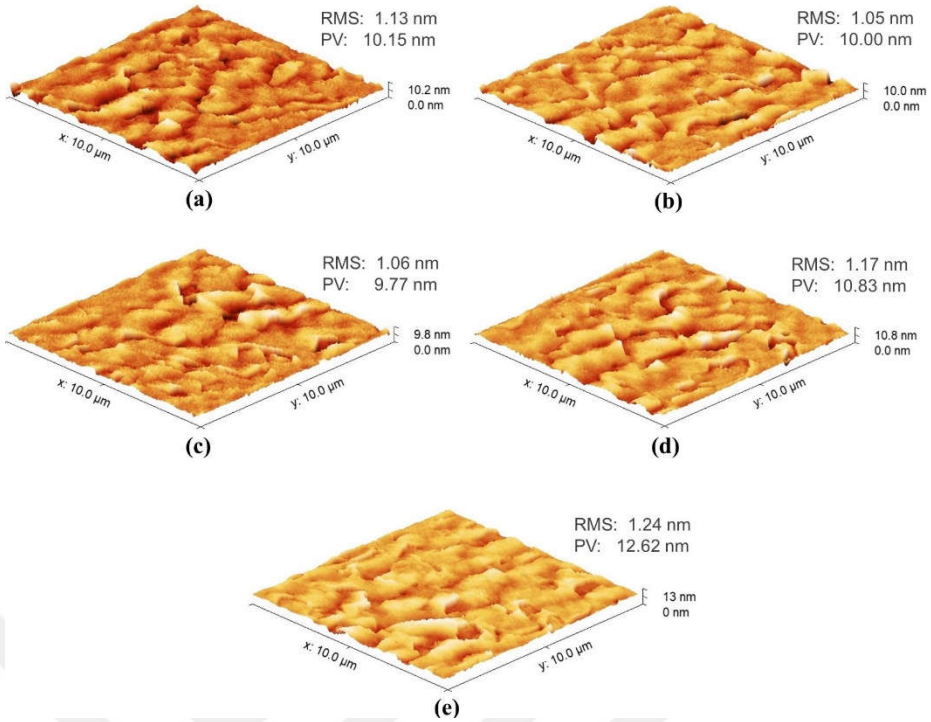

Figure 4.3. *3D AFM images of the samples in Set 1 with AlSb NL thickness of (a) 5 ML, (b) 10 ML, (c) 20 ML, (d) 40 ML and (e) 80 ML.*

When the surface morphologies of the samples were analyzed by SEM, the MTs and APBs can be seen from the obtained images and have been marked by yellow and violet arrows, respectively, for clarity sake (Figure 4.4). Some segments either isolated or connected with other segments to form L-like shape which are attributed to MTs [40]. It is observed that the density of MTs is related with the AlSb NL thickness. The density of the MTs can be determined by dividing the total length of the segments by the scan area. The determined MTs densities are presented in Figure 4.5 as a function of AlSb NL thickness. As can be perceived from Figure 4.5, the density of MTs tends to decrease with an increase in AlSb NL thickness up to 20 ML. Namely, it decreases from 2887 cm^{-1} down to 268 cm^{-1} for an AlSb NL thickness of 5 and 20 ML, respectively. However, that trend changes above 20 ML AlSb NL thickness and it starts to increase and reaches up to a value of 4181 cm^{-1} which is even higher than the one with a 5 ML AlSb NL thickness.

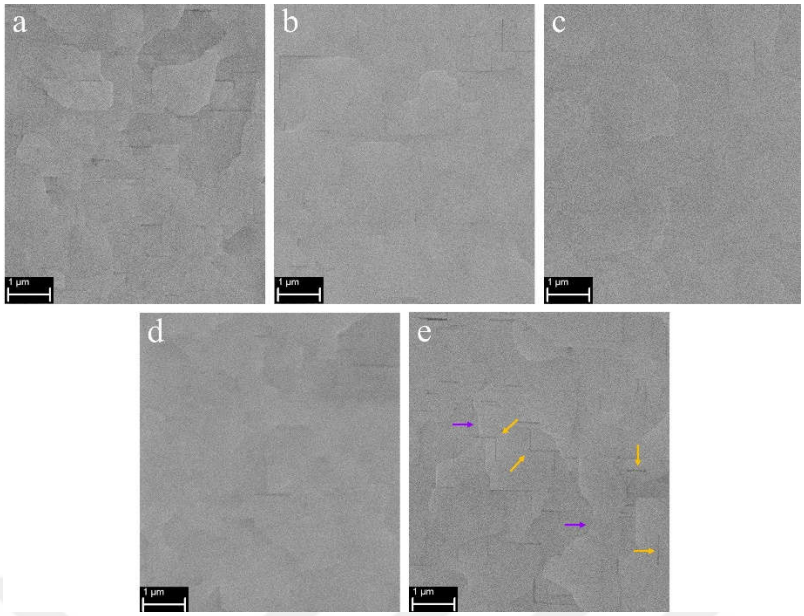

Figure 4.4. *SEM images of GaSb epilayers grown on Si with AlSb NL thickness of (a) 5, (b) 10, (c) 20, (d) 40 and (e) 80 MLs. The MTs and APBs are marked by yellow and violet arrows, respectively in (e).*

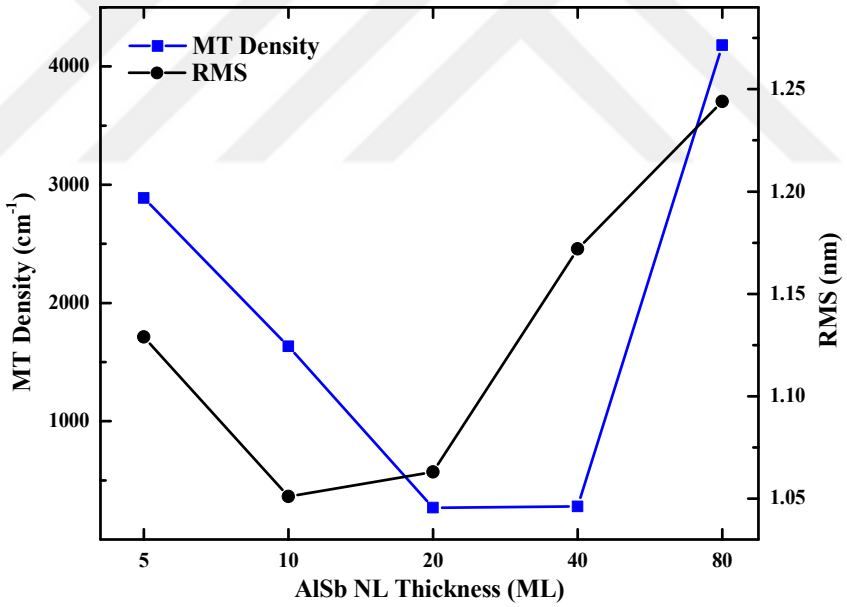

Figure 4.5. *The MT density and RMS of the GaSb epilayers grown on Si as a function of AlSb NL thickness.*

A similar behavior is observed for the RMS values of the samples: The RMS value decreases with an increase in AlSb NL thickness until 10 ML and it increases above that value and reaches up to a value of 1.24 nm for a scanning area of 100 µm^2. Although the best RMS value was obtained from an AlSb NL thickness of 10 ML, together with the determined MT density the sample that has an AlSb NL thickness of 20 ML seems to be an optimized value since the RMS value of that sample (1.06 nm) is very close to

the one with an AlSb NL thickness of 10 ML. Thus, it may be proposed that there is a relation between the surface roughness and the MT density.

In order to examine the samples deeper, further experiments were applied to define the defect types by wet etching process [107]. As shown in Figure 4.6, better identification of the APBs are possible for all samples, which is an expected result due to the polar/nonpolar surface incompatibility. In addition to the APBs, in the etched samples the etch pits are observed as well. The APB density for each sample was determined and plotted as a function of AlSb NL thickness in Figure 4.7. In order to present the role of the APB density on the surface of the as-grown GaSb epilayers, both the RMS and PV values are given in Figure 4.7, as well. As it can be perceived from the figure, the APB density trend changes as a function AlSb NL thickness. Namely, up to 20 ML thickness it decreases and reaches to a minimum value of 0.55 μm^{-1} where above that thickness it increases and reaches to a maximum value of 0.66 μm^{-1}. It is ascertained that the RMS and PV exhibits almost the same behavior and the surface roughness seems to be dominated by the APB density, considering the PV values.

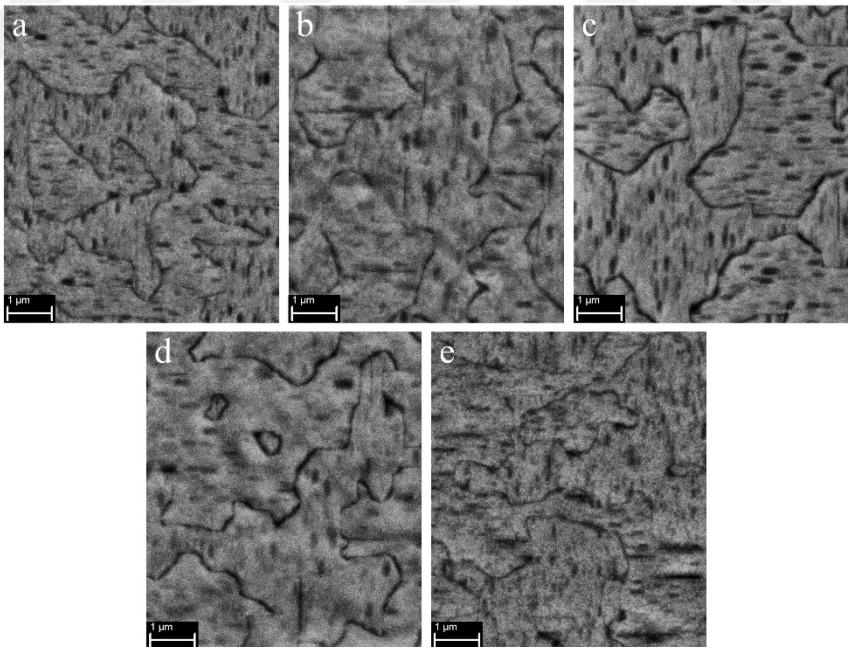

Figure 4.6. *SEM images of etched GaSb epilayers grown on Si having AlSb NL thickness of (a) 5, (b) 10, (c) 20, (d) 40 and (e) 80 MLs.*

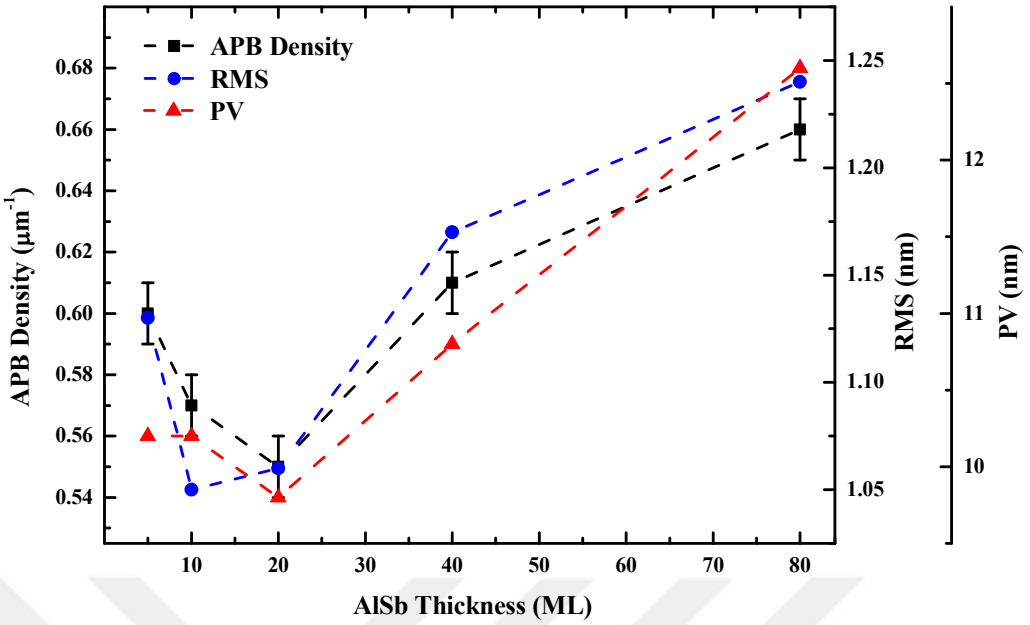

Figure 4.7. *The APB density, RMS and PV of the GaSb epilayers grown on Si as a function of AlSb NL thickness. The dotted lines are guide for the eyes. The APB density is obtained from etched where the RMS and PV values are obtained from the as-grown samples.*

For a better understanding of the effect of AlSb NL thickness on the optical quality of GaSb epilayer, PL measurements were conducted for all the samples in Set 1 at 10 K and presented in Figure 4.8. By deconvoluting the measured spectra (dotted black line) using Gaussian distribution, the peak positions/intensities and the energy values were determined. As can be observed, all the samples depict four characteristic peaks at ~ 767, 780, 795 and 810 meV that are attributed to undoped GaSb radiative transitions [108]. Among those, the peaks at ~ 767 and 780 meV are interpreted as transitions from the conduction band to an acceptor level (BA) and from a donor to an acceptor level (DA), respectively [108]. Furthermore, the other ones observed at ~ 795 meV are assigned to bound exciton (BE) and 810 meV are assigned to free exciton (FE) [108].

It is known that observation of FE transition peak is an indication of high material quality [108, 109]. In our samples, the FE peak appears as a shoulder rather than a clear peak. However, this peak is commonly not observed due to the low crystal quality of the GaSb epilayer [110]. At this point it is important to note that the excitation wavelength (532 nm) used in PL measurements has a penetration depth of 26 nm [111], which means that the obtained PL signal is coming from the regions close to the surface. Although, due to the excitation wavelength, the PL signals do not offer information from the complete GaSb epilayer, they are comparable and crucial in the discussion of epilayer

quality close to the surface. Besides, keeping in mind that the defects throughout the GaSb epilayer have an impact on the region close to the surface, the obtained PL exhibits clue about the quality of the whole GaSb epilayer.

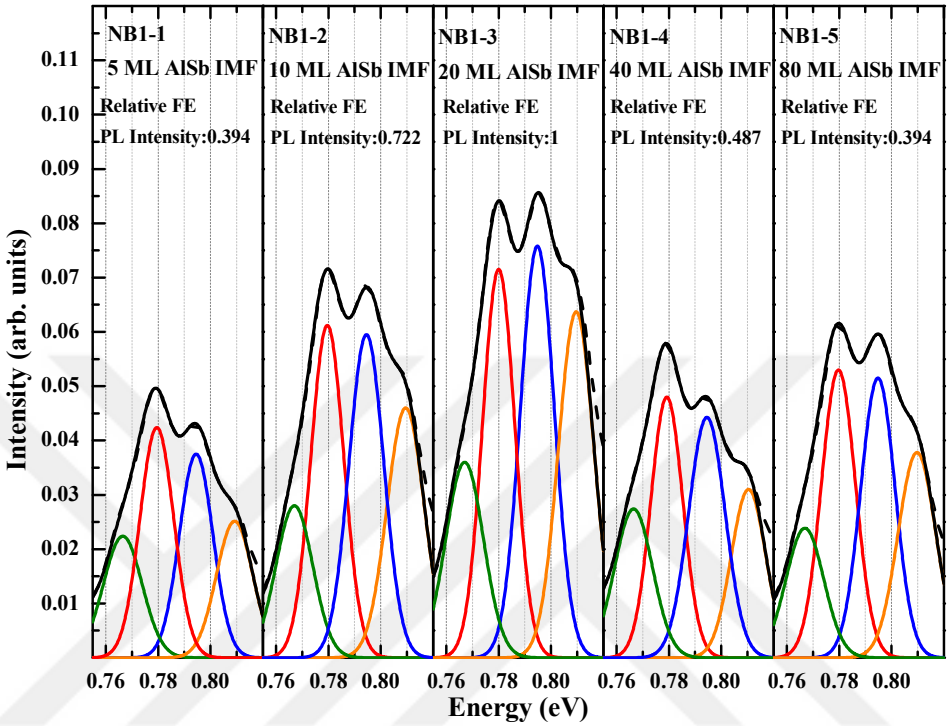

Figure 4.8. *10 K PL spectra of the samples in Set 1 with different AlSb NL thicknesses. From the fit (solid black line) of the measured spectra (dotted black line) using Gaussian distribution the accurate peak positions/intensities and the energy values were found. The BA, DA, BE and FE peaks are identified by the green, red, blue and orange lines, respectively.*

For a better comparison of the samples in Set 1, the relative FE peak intensities (relative to the highest intensity obtained from the sample in Set 1) are given in Figure 4.8. It is observed that the highest FE peak intensity was obtained from the sample NB1-3. This result is consistent with the FWHM value and TD density and indicates that the best GaSb epilayer crystal quality was achieved for the sample where AlSb NL thickness of 20 ML was used. Another important point is that only this sample shows a different BE/DA peak intensity ratio in Set 1. Namely, as it can be observed from Figure 4.8, only the sample NB1-3 has a BE/DA peak intensity ratio which is higher than 1. This behavior is attributed to a better crystal quality as well as FE peak observation in the PL signal [108].

4.3. The Effect of Growth Temperature

After determining the optimized AlSb NL thickness, the effect of growth temperature on the crystal quality of GaSb epilayers were monitored by using three different growth temperatures (530, 550 and 570 °C). In a similar way to Set 1, the samples in the Set 2 were investigated by HRXRD, PL, AFM and SEM analysis. As can be seen from Table 4.4, the FWHM values and TD densities are improved with an increase in growth temperature. On the other hand, it is observed that the RMS and PV values are getting worse at a growth temperature higher than 530 °C, as shown in Figure 4.9. Those results indicate that although a structural improvement was achieved by increasing the growth temperature, the surface roughness of the GaSb epilayers are affected negatively at growth temperatures above 530 °C.

Table 4.4. *Summary of the HRXRD results for the samples in Set 2 for different GaSb growth temperatures.*

Sample Code	**NB1-3**	**NB2-2**	**NB2-3**
GaSb growth temperature (°C)	530	550	570
RC FWHM (arcsec)	302	272	252
TD density (cm^{-2})	3.09×10^{8}	2.63×10^{8}	2.09×10^{8}

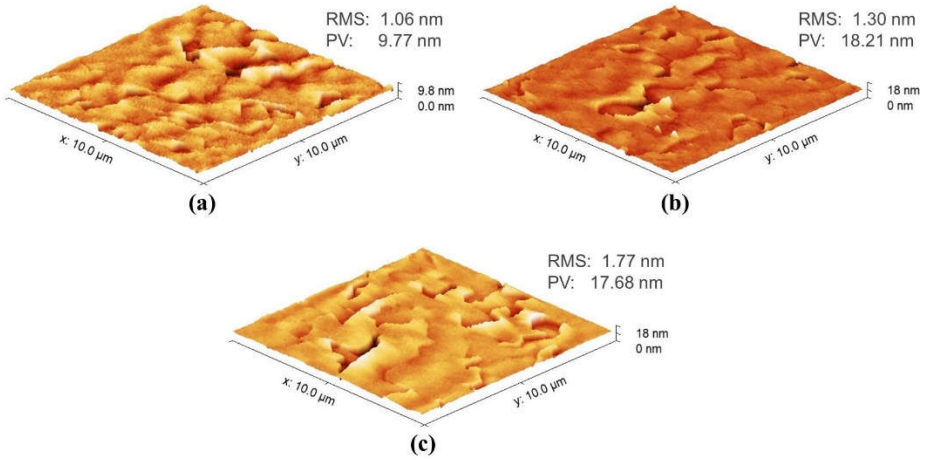

Figure 4.9. *3D AFM images of the samples for the growth temperature of (a) 530 °C, (b) 550 °C and (c) 570 °C.*

The effect of growth temperature on the GaSb epitaxial films in terms of the MT density and RMS value were investigated and the determined MT density and RMS values are given in Figure 4.10. Although the MT density slightly decreases with growth

temperature, the RMS value increases up to 1.77 nm for the growth temperature of 570 °C. According to that result, it can be argued that the MT density is not very effective on the surface roughness. The images obtained from SEM for as-grown and etched films are presented in Figure 4.11 and Figure 4.12, respectively. The boundaries of anti-phases on the surface of the sample grown at the highest growth temperature in Figure 4.11(c) appear sharper and it is observed that an increase in the growth temperature has a significant role on etch pits. As can be seen from Figure 4.12, the etch pits are disappeared for the samples grown at 550 and 570 °C.

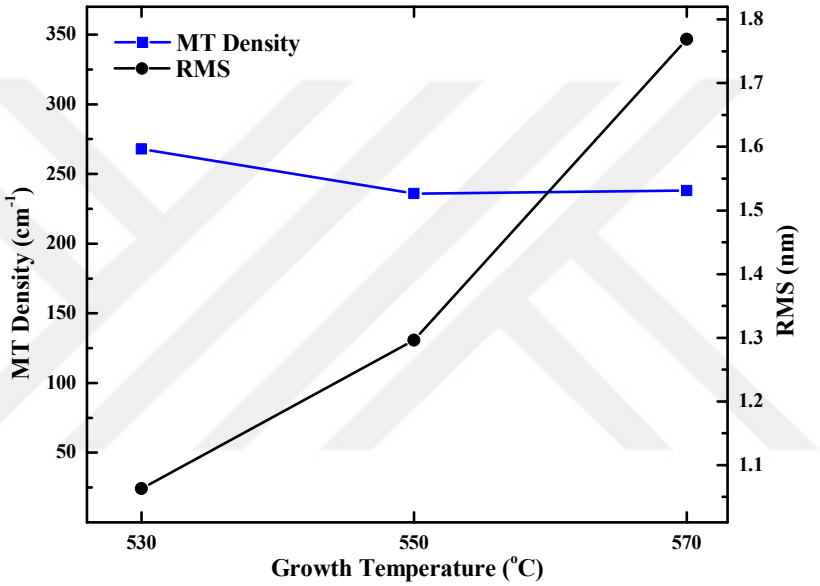

Figure 4.10. *The MT density and RMS of the GaSb epilayers grown on Si as a function of growth temperature.*

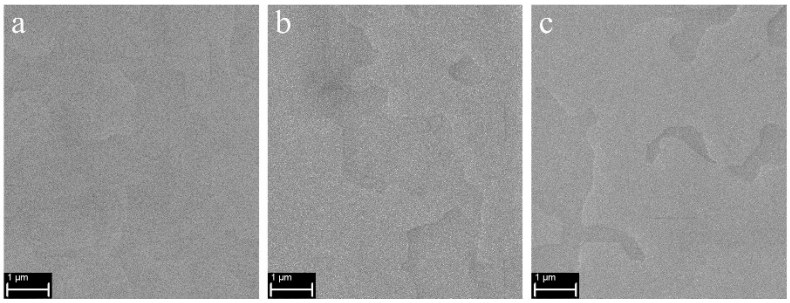

Figure 4.11. *SEM images of as-grown GaSb epilayers on Si at the growth temperature of (a) 530, (b) 550 and (c) 570 °C.*

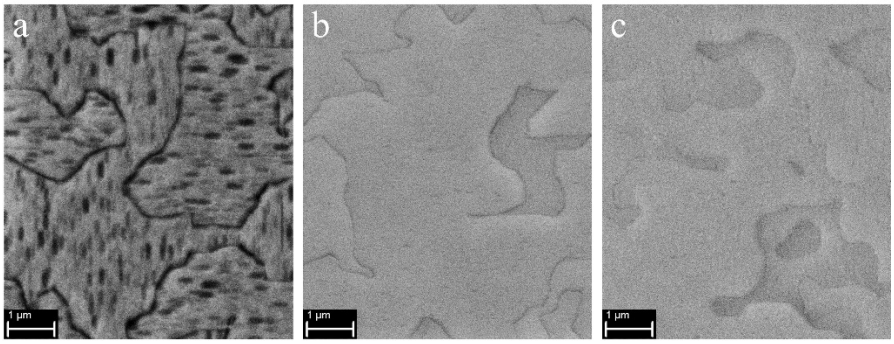

Figure 4.12. *SEM images of etched GaSb epilayers on Si at the growth temperature of (a) 530, (b) 550 and (c) 570 ºC.*

However, the APB density decreases at the growth temperature of 550 ºC. This is an expected result and related with APB kinking and annihilation at higher growth temperatures [112-114]. However, it increases and reaches to 0.63 μm^{-1} for the growth temperature of 570 ºC which is even higher than the one's grown at 530 ºC (Figure 4.13). In spite of the higher growth temperatures leading the APB self-annihilation, the abrupt increase in the APB density is unclear for the growth temperature of 570 ºC or higher. As it is observed, both the APB density and RMS value are higher than the one's grown at comparably lower temperature. It is worth to note that the decrease in the APB density doesn't show itself as an improvement in the RMS value. It is believed that, this behavior can be explained by the PV value which is higher than the sample grown at 530 ºC. It seems that the decrease in the APB density cannot compensate the increase in the PV value which results in a worse RMS value compared to the one's grown at 530 ºC.

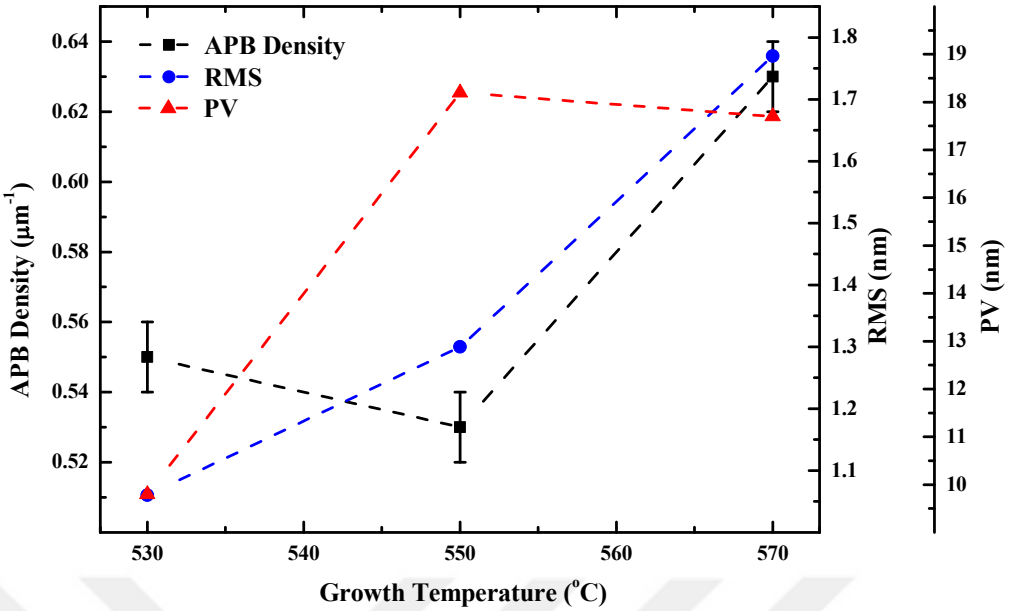

Figure 4.13. *The APB density, RMS and PV of the GaSb epilayers grown on Si as a function of growth temperature. The dotted lines are guide for the eyes. The APB density is obtained from etched where the RMS and PV values are obtained from the as-grown samples.*

It is known that the APBs have a role in the surface morphology depending on the growth temperature [115] and relatively higher growth temperatures can trigger APDs with larger sizes [115,116], while resulting in a decrease in APBs density. That behavior can be explained by the initiation of self-annihilation of APBs via kinking to higher index planes and the APD self-annihilation regions under the surface may induce the sharper surface undulation with an increase in the growth temperature. Thus, it is concluded that using a relatively lower temperature (530 °C) results in a smoother surface and can be accepted as a more suitable temperature to grow GaSb epilayers on Si (100).

To probe the optical properties of the GaSb epilayers, low temperature PL measurements were conducted and presented in Figure 4.14. Contrary to the FWHM and the TD density results, the whole PL signal, as well the FE peak intensity decreases dramatically as a function of growth temperature. Although a structural improvement was achieved by increasing the growth temperature, the optical quality and the surface roughness of the GaSb epilayers are affected negatively at growth temperatures above 530 °C.

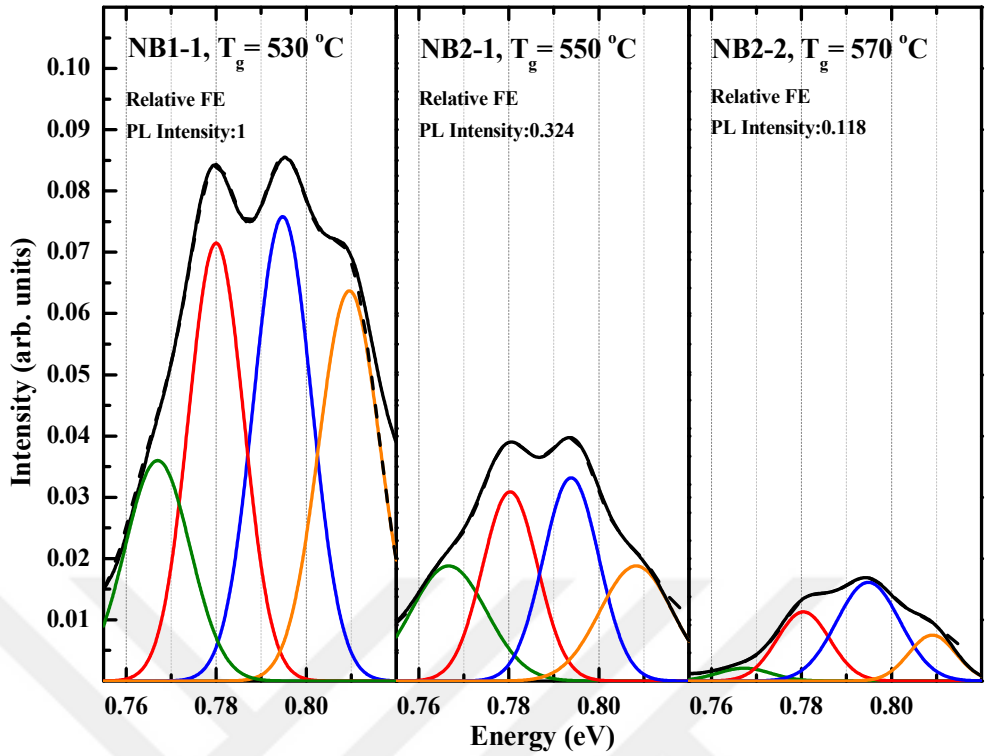

Figure 4.14. *10 K PL spectra of the samples in Set 2 for different GaSb growth temperatures (T_g). From the fit (solid black line) of the measured spectra (dotted black line) using Gaussian distribution the accurate peak positions/intensities and the energy values were found. The BA, DA, BE and FE peaks are identified by the green, red, blue and orange lines, respectively.*

4.4. The Effect of Post-growth Annealing and Duration

It is well known that post annealing in the growth chamber helps to improve the crystal quality of the epilayer. To this purpose, three different post annealing temperatures (550, 570 and 590 ºC) for 30 min were applied to the samples following the growth process. The RCs exhibit a structural improvement as a function of post-growth annealing temperature (Table 4.5). Namely, the FWHM value decreases with an increase in post-growth annealing temperature. For a post-growth annealing temperature of 590 ºC for 30 min the FWHM values and TD densities are decreased by 20% and 39%, respectively.

Table 4.5. *Summary of the HRXRD results for the samples in Set 3 for different post annealing temperatures.*

Sample Code	**NB1-3**	**NB3-1**	**NB3-2**	**NB3-3**
Post annealing temperature (ºC)	none	550	570	590
RC FWHM (arcsec)	302	277	260	242
TD density (cm^{-2})	3.09×10^{8}	2.60×10^{8}	2.36×10^{8}	1.89×10^{8}

The images obtained from the surface of the samples by SEM and AFM are presented in Figure 4.15 and 4.16, respectively. An interesting result was attained from the sample post annealed at 590 ºC where Sb desorption occurred and Ga droplets were formed at the surface of the sample. In order to define the Ga droplets, elemental analysis at two different positions on the surface were conducted and the results are presented in Figure 4.15(d). As can be seen elemental analysis clearly indicates that the regions marked by yellow and blue plus signs involve Ga and Ga/Sb elements, respectively. As can be perceived from Figure 4.15(d), due to the high temperature, Sb desorption from the surface occurs and Ga droplets are formed at the surface which results in an RMS value of 36.7 nm. For a better comparison with the rest of the samples in this set, the RMS value is obtained from the Ga droplet free surface region as 1.7 nm. This result is remarkable since it demonstrates a radical change on the surface of the grown GaSb epilayer even the FWHM value is improved down to 242 arcsec. Besides, the TD density determined for this sample is as low as 1.89×10^{8} cm^{-2}. Hence, we believe that an improvement in the FWHM value alone could not be a direct evidence of a better crystal quality of GaSb on Si without considering other complementary methods such as PL and AFM. Considering the surface roughness, it is observed that the RMS value is improved for the sample NB3-1 and decrease to 0.98 nm for a region of 100 μm^2 (Figure 4.16(b)). However, in contrast with the RMS value, all the post annealed samples exhibit worse PV values than the reference sample NB1-1.

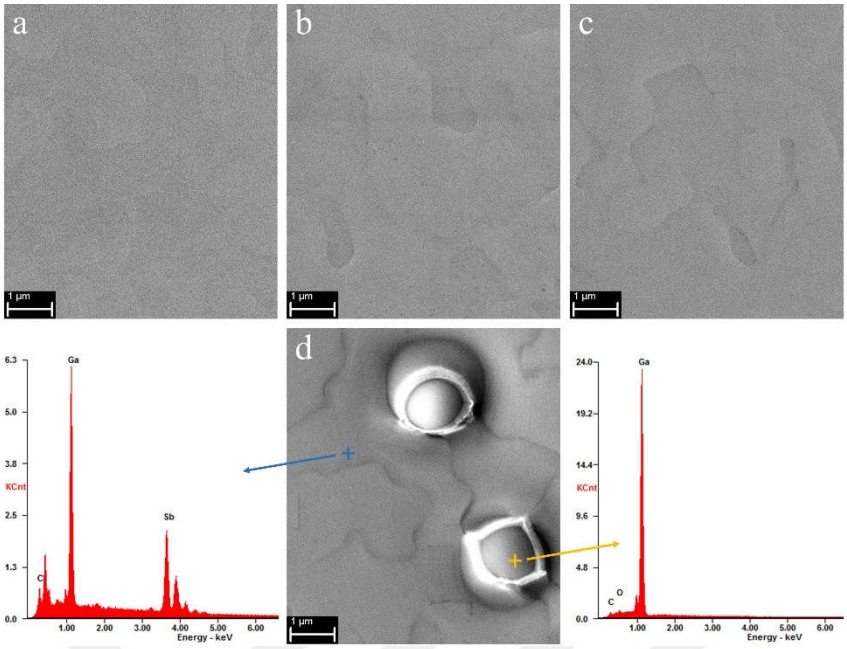

Figure 4.15. *SEM images of GaSb epilayers grown on Si and post annealed at (a) none, (b) 550 and (c) 570 and (d) 590 °C with EDX analysis.*

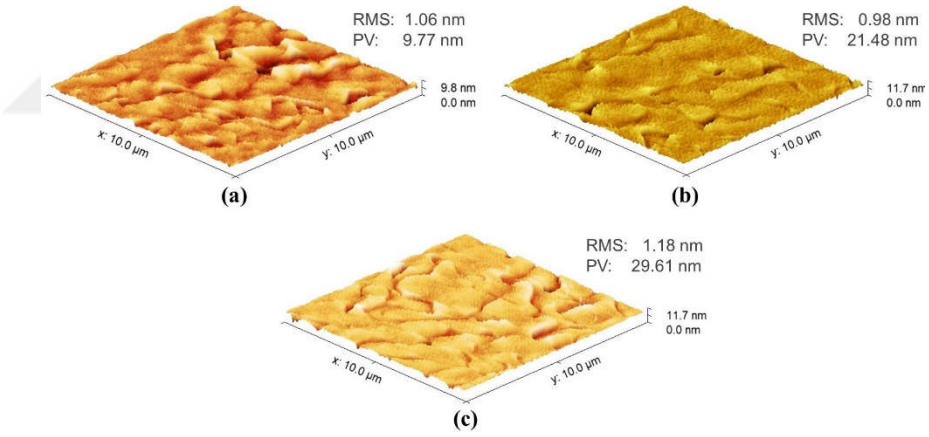

Figure 4.16. *3D AFM images of the samples for a post annealing temperatures of (a) none, (b) 550 °C and (c) 570 °C.*

The MT density and RMS values are shown in Figure 4.17. As can be seen, the MT density reduces significantly for the sample which was post annealed at 570 °C. With this sample, a value of 186 cm^{-1} was achieved which is a quite reasonable value considering the large lattice mismatch been Si and GaSb.

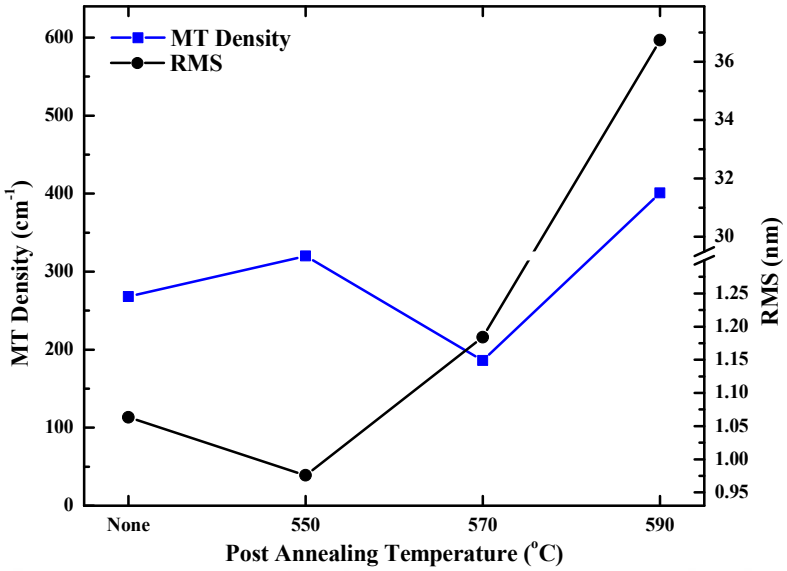

Figure 4.17. *The MT density and RMS of the GaSb epilayers grown on Si as a function of post annealing temperature.*

Comparing etched surfaces, it is demonstrated that post-growth annealing has a similar effect as growing GaSb epilayers at comparably higher temperatures. Due to the Ga droplet formation on the sample of NB3-3 in this set, only the other ones are subjected to the etch process and the SEM micrographs are shown in Figure 4.18. Namely, for the post annealed samples no etch pits are observed in contrast to the one that no post annealing treatment applied (reference sample). Besides, it is detected that the APB density decreases significantly and reaches to a value of 0.5 μm^{-1} for a post annealing of 550 ^{o}C for 30 min (Figure 4.19). In addition, although the PV value increases, due to a significant decrease in the APB density RMS value improved and reached to a value of 0.98 nm. Which is crucial for the fabrication of Sb-based material on Si substrates [117]. In contrary to the improvement for the sample post annealed at 550 ^{o}C, Figure 4.19 depicts that a further increase in the post annealing temperature causes an increase in both the APB density and PV value. Although it is unknown and exhibits similar behavior as in case of the growth temperature, the APB density of this sample is lower than the reference sample and due to the increase in the PV value the RMS value getting worse which is not desired.

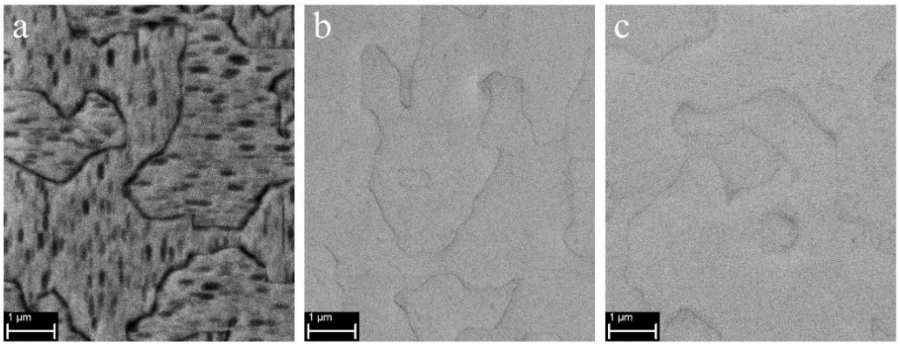

Figure 4.18. *SEM images of etched GaSb epilayers on Si grown at 530 °C (a) as-grown and post annealed at (b) 550 °C and (c) 570 °C for 30 min.*

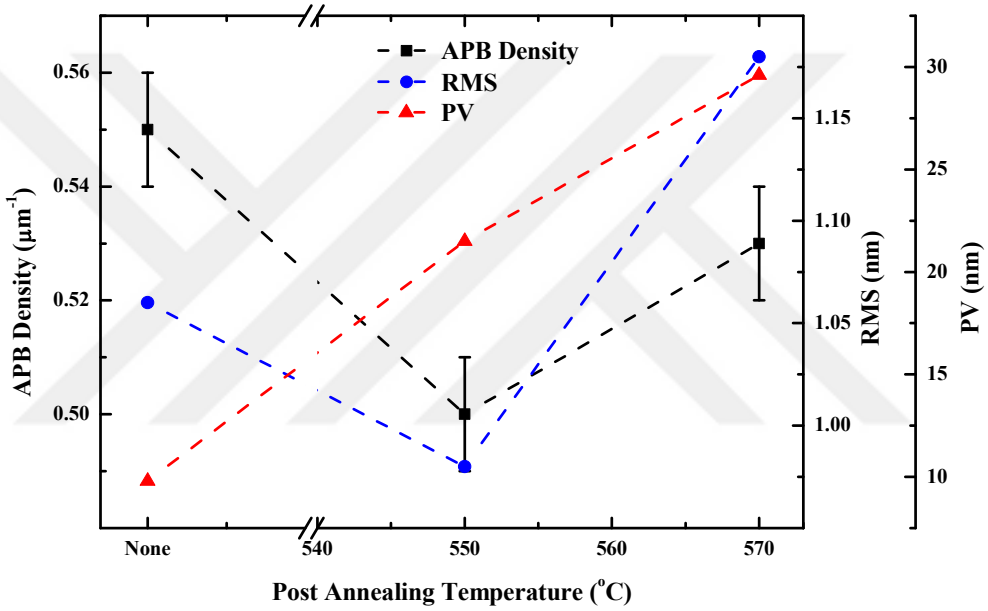

Figure 4.19. *The APB density, RMS and PV of the GaSb epilayers grown on Si as a function of post-growth annealing temperature. The dotted lines are guide for the eyes. The APB density is obtained from etched where the RMS and PV values are obtained from the as-grown samples.*

Guo et.al. [118] have reported that an APB-modified thermodynamic equilibrium mechanism was suggested to explain the alteration of surface roughness. It indicates that the post-growth annealing leads an enhanced migration of the surface atoms toward more stable positions, such as free crystalline sites. Thus, anti-phase and main phase regions are separated and appear like crystalline mountains, giving rise to an increase in the surface roughness due to the deep trenches in the boundary lines. As shown in Figure 4.18, the higher post-growth annealing temperature might promote further this event. It is apparent that the thermal annealing process has an impact on the mobility of atoms

involving APBs. Besides the reduction of the APB density depending on the post-annealing temperature can be explained by the atomic motion toward APB centers of curvature, happening near the surface region [119].

As it is demonstrated from Set 2, the improvement in structural quality cannot be directly related to the improvement in optical and surface quality of the epilayers. On the other hand, unlike to Set 2, in Set 3 an improvement in optical quality was achieved for the sample NB3-2 which was post annealed at a temperature of 570 ºC for 30 min. As it is extracted from Figure 4.20, the sample NB3-2 shows the highest FE peak intensity.

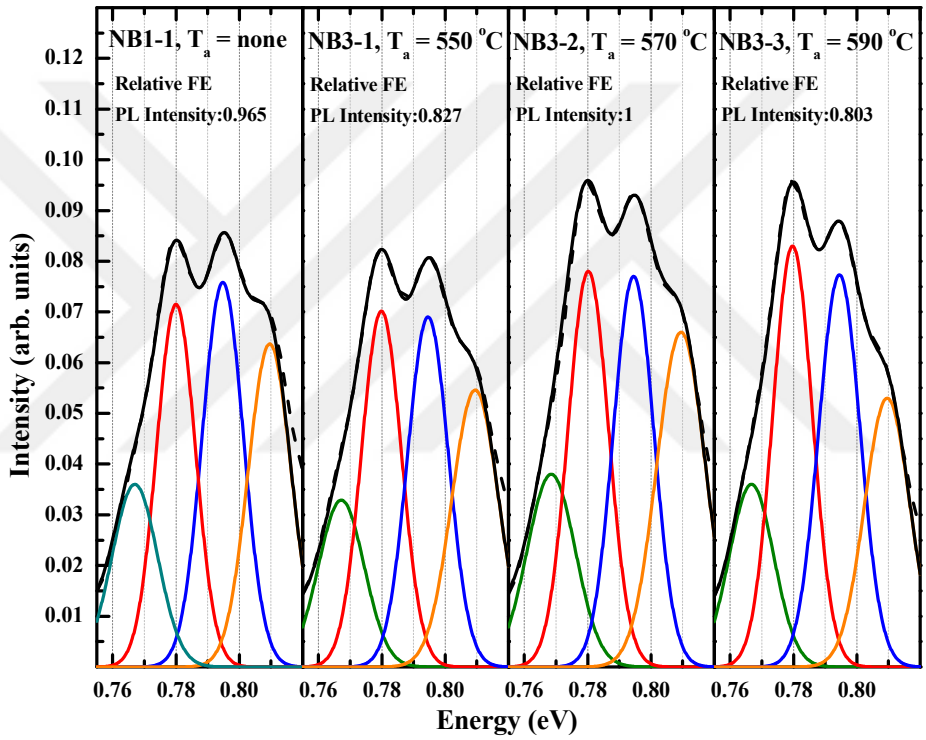

Figure 4.20. *10 K PL spectra of the samples in Set 3 for different post annealing temperatures (T_a). From the fit (solid black line) of the measured spectra (dotted black line) using Gaussian distribution the accurate peak positions/intensities and the energy values were found. The BA, DA, BE and FE peaks are identified by the green, red, blue and orange lines, respectively.*

To find out the optimum post-growth annealing temperature, the GaSb epilayers were annealed for various durations at the temperature of 570 ºC, following the growth process. As presented in Figure 4.21, the best post-growth annealing duration is found as 60 min. in terms of the crystal quality. As increasing the duration, it is obvious that the TD and APB densities increase again. Besides, the MTs on the surface of sample NB3-5 pops out, as demonstrated in Figure 4.22(c).

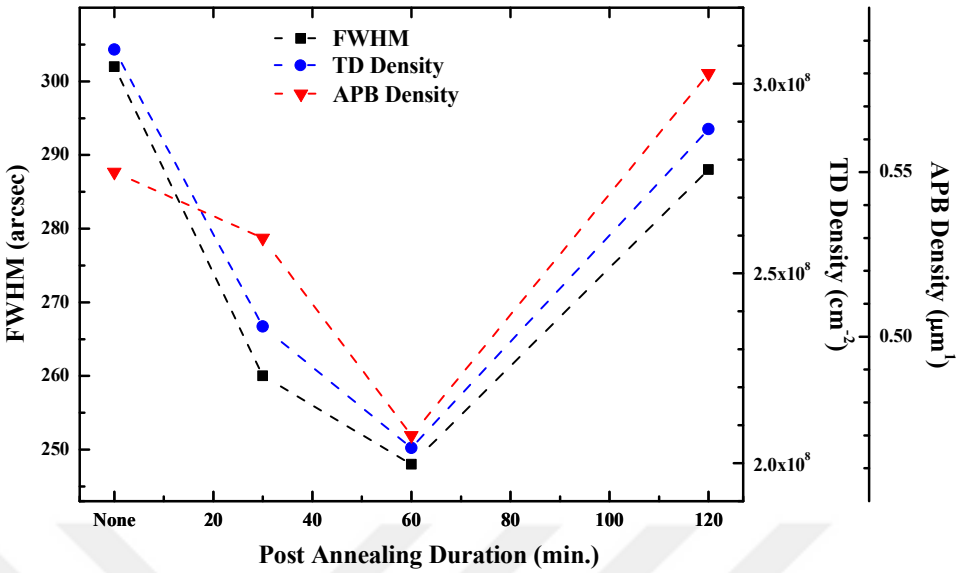

Figure 4.21. *The FWHM of X-ray RC around the (004) reflection, the TD density and APB density of the GaSb epilayers grown at the temperature of 570 °C as a function of post-growth annealing duration. The dotted lines are guide for the eyes. The APB density is obtained from etched samples.*

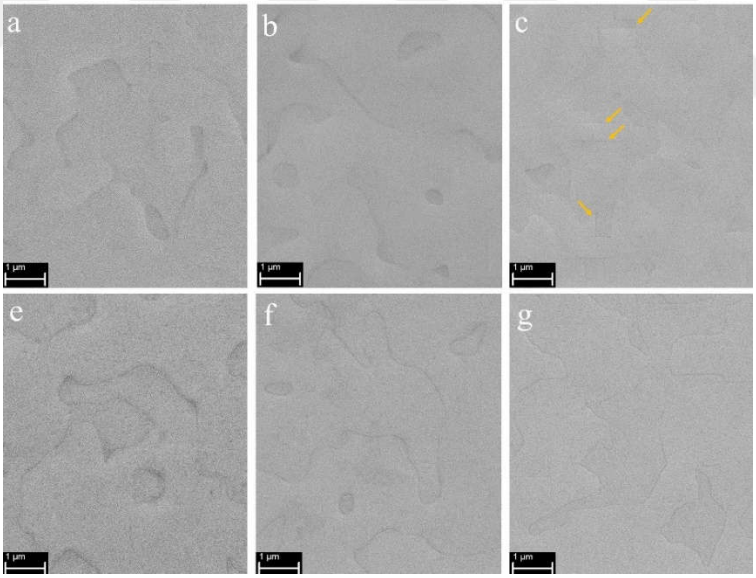

Figure 4.22. *SEM images of as-grown GaSb epilayers on Si post annealed at 570 °C for (a) 30 min (b) 60 min and (c) 120 min. SEM images of etched GaSb epilayers on Si post annealed at 570 °C for (a) 30 min (b) 60 min and (c) 120 min. The MTs are marked by yellow arrows in (c).*

In the light of the results, two different thermal treatments was also applied to enhance the crystal quality of the GaSb epilayers. The growth process of the grown GaSb samples is presented in Figure 4.23. For the sample NB3-6, thermal annealing at 570 °C

for 30 min was applied as an intermediate step, subsequent to the growth of 150 nm thick GaSb epilayer. Then the growth of GaSb epilayer was proceeded to reach the total thickness of 1 μm. For the sample NB3-7, 50 nm thick GaSb layer was grown at the growth temperature of 485 ºC following the initiation of AlSb NL. Then, the 50 nm of GaSb layer was grown at different temperatures by increasing the substrate temperature with a very slow ramp rate (2.5 ºC/min), as shown in Figure 4.23(b). After reaching at the growth temperature of 530 ºC, the growth of GaSb layer in thickness of 850 nm was carried out.

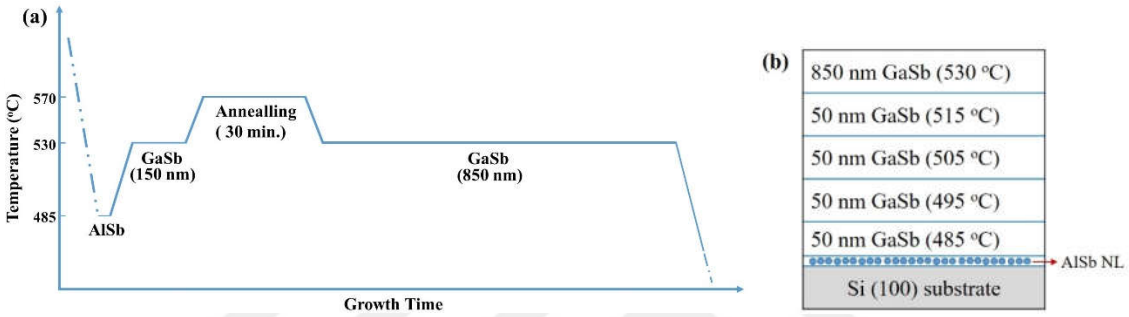

Figure 4.23. *The growth steps of the samples (a) NB3-6 and (b) NB3-7.*

When examining the surface of etched samples, NB3-7 exhibits a surface with APBs and MTs, as shown in Figure 4.24(c). It indicates that the growth of GaSb epilayer at low temperature introduces MTs into the layer. Besides, the TD and APB densities of NB3-7 increased by 38% and 128%, respectively, when comparing with sample NB3-4 (Figure 4.25). On the other hand, the RMS value of NB3-7 is determined as 2.26 nm, which is the highest value obtained within all sets in this chapter. It is clear that severely increased defects show an effect on the surface roughness.

Considering the NB3-6, it is found a more promising method as a thermal treatment. Comparing the samples NB3-4 and NB3-6, it is observed that the TD density of NB3-6 is obviously decreased with the enhancement of the crystal quality (Figure 4.25) and a surface without MTs is obtained (Figure 4.24(e)), although the post-annealed duration was kept same as NB3-4. However, it can be said that an intermediate annealing step does not has an influence on the APBs density, dramatically, when compared with NB3-4.

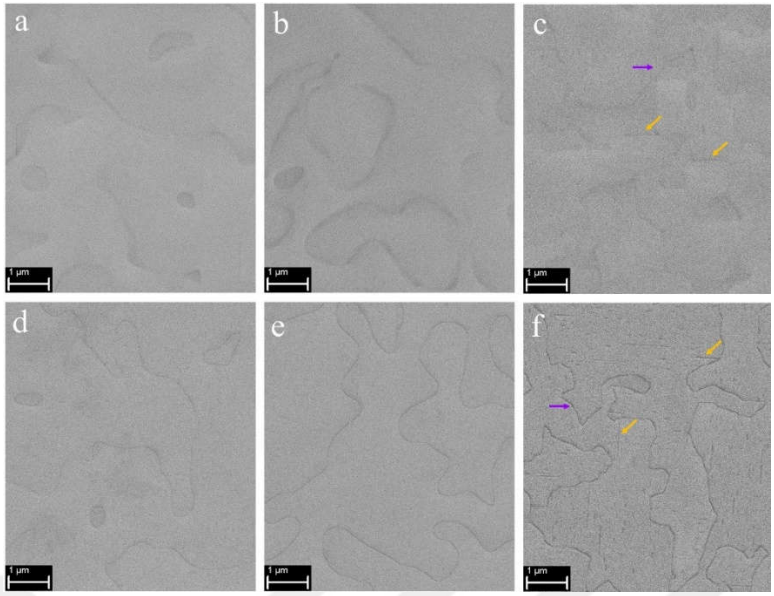

Figure 4.24. *SEM image of the samples (a) NB3-4, (b) NB3-6 and (c) NB3-7. SEM image of the etched samples (d) NB3-4, (e) NB3-6 and (f) NB3-7. The MTs and APBs are marked by yellow and violet arrows, respectively in (c) and (f).*

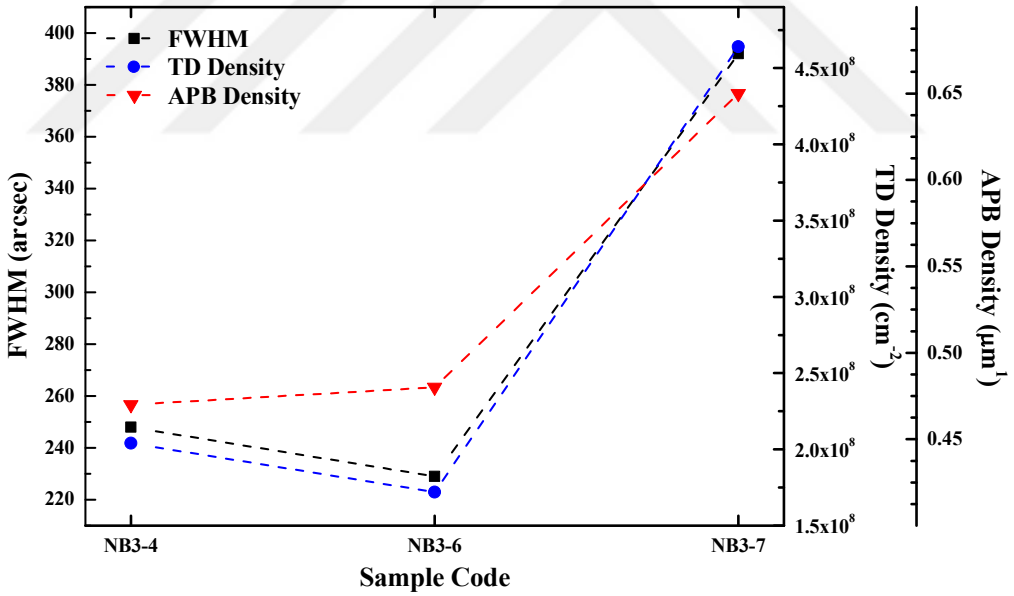

Figure 4.25. *The FWHM of X-ray RC around the (004) reflection, the TD density and APB density of the samples, NB3-4, NB3-6 and NB3-7. The dotted lines are guide for the eyes. The APB density is obtained from etched samples.*

4.5. Summary and Conclusions

The crystal quality of the heteroepitaxial GaSb epilayers on Si with AlSb interfacial layer was investigated in terms of NL thickness, growth and post annealing temperature.

All obtained results are summarized in Table 4.6, Table 4.7 and Table 4.8, respectively. Considering the structural, optical and surface roughness properties of the GaSb epilayers grown at 530 ^{o}C on Si (100), the results demonstrate that the best GaSb epilayer quality was obtained with an AlSb NL thickness of 20 ML, in respect to interfacial layer. In addition, it should be mentioned that GaSb epilayers were also grown directly on Si substrates to observe the impact of AlSb NL. The SEM images of GaSb epilayers grown with different group III/V ratios presented in Figure 4.26. exhibit either GaSb crystal structures with Ga droplets or GaSb crystallization with very high surface roughness. As depicted in Section 4.2, it is obvious that even 5ML thick AlSb NL can drastically enhances the GaSb epilayer quality by forming favorable 3D nucleation sites along the interface and creating a strain relief for misfit dislocations [34].

Table 4.6. *Summary of the obtained results for the samples in Set 1 with different AlSb nucleation layer thicknesses.*

Sample Code	**NB1-1**	**NB1-2**	**NB1-3**	**NB1-4**	**NB1-5**
RC FWHM (arcsec)	340	315	302	308	374
TD density (cm^{-2})	4.24×10^{8}	3.52×10^{8}	3.09×10^{8}	3.12×10^{8}	4.79×10^{8}
Relative FE PL intensity	0.394	0.722	1	0.487	0.593
RMS (nm)	1.13	1.05	1.06	1.17	1.24
PV (nm)	10.15	10.00	9.77	10.83	12.62
The MT density (cm^{-1})	2887	1634	268	279	4181
The APB density (µm^{-1})	0.6	0.57	0.55	0.61	0.66

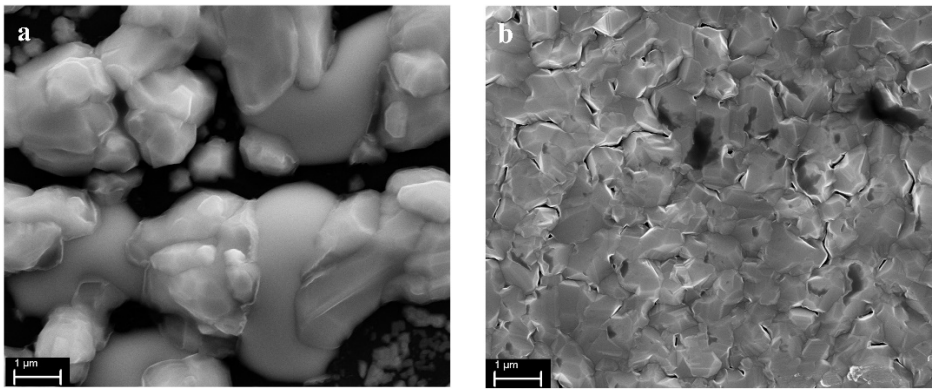

Figure 4.26. *The GaSb layers grown directly on Si at a growth temperature of 530 ^{o}C with group V/III ratio of (a) 10 and (b) 20.*

Considering the defect formation, it is understood that the variation of AlSb NL thickness has a pronounce effect on both the APB and MT densities (Table 4.6). Combining the obtained results from the growth temperature and post-growth annealing, the significant reduction in the MT density was observed as a function of AlSb NL thickness. Vajargah *et.al.* [34] have reported that AlSb islands reduce the diffusion length of Ga atoms and the GaSb atomic layers nucleate on the energetically preferred facets of AlSb islands. More particularly, it is ascertained that increasing AlSb NL thickness (i.e. the formation of the island coalescence) induces more defects to the GaSb epilayer during the growth (Figure 4.1(b)). Therefore, more structural analysis should be executed on the GaSb nucleation via AlSb NL thickness to understand the mechanism of defect formation. As a consequence, it is important to optimize the AlSb NL growth parameters for the growth of better quality GaSb epilayers.

Although the structural improvements and the surface without the etch pits were observed for the GaSb epilayers grown at higher temperatures, it was shown that the optical quality and the surface roughness of the samples worsens by increasing the growth temperature. It may be argued that non-radiative recombinations become more dominant by activation of complex defects at higher growth temperatures, although this needs further investigation. Comparing with the other results, the formation of MTs is more insensitive at elevated temperatures (Table 4.7) and it is evidenced that the deterioration in the RMS is more related to the APBs compared to MTs as discussed in Section 4.3.

Table 4.7. *Summary of the obtained results for the samples in Set 2 for different GaSb growth temperatures.*

Sample Code	**NB1-3**	**NB2-1**	**NB2-2**
GaSb growth temperature (°C)	530	550	570
RC FWHM (arcsec)	302	272	252
TD density (cm^{-2})	3.09×10^{8}	2.63×10^{8}	2.09×10^{8}
Relative FE PL intensity	1	0.324	0.118
RMS (nm)	1.06	1.30	1.77
PV (nm)	9.77	18.21	17.68
The MT density (cm^{-1})	268	236	238
The APB density (μm^{-1})	0.55	0.53	0.63

While improving the structural quality by post annealing it is revealed that the improvement in the optical quality and surface roughness of the samples are limited. The results assist that the post-growth annealing process is more favorable way, rather than increasing the growth temperature. Compared to the reports where the buffer layers include variable epilayer steps or are grown on vicinal Si substrates [40, 120], our results denote that MTs density could be notably reduced to 186 cm^{-1} with the utilization of AlSb NL layer and the post-growth annealing for the GaSb epilayer grown on nominal Si substrates (Table 4.8). Besides, the post annealing process demonstrated that the APB density and RMS value could be significantly improved even though the PV value increased. In addition, it should be noted that the thermal annealing provides a straightforward, effective method for highly mismatched structures, by healing defects. Furthermore, it is shown that the crystal quality can be improved with the post-growth annealing duration and an intermediate annealing step. Hence, it is important to comprehend the effect of the growth temperature and the post-growth annealing on the atomic configuration of the APBs, and it is worthy to conduct further investigation to reveal the APBs formation mechanism relative to the growth temperature and the thermal treatment process.

Table 4.8. *Summary of the obtained results for the samples in Set 3 for different post annealing temperatures.*

Sample Code	**NB1-3**	**NB3-2**	**NB3-2**	**NB3-3**
Post annealing temperature (°C)	none	550	570	590
RC FWHM (arcsec)	302	277	260	242
TD density (cm^{-2})	3.09×10^{8}	2.60×10^{8}	2.36×10^{8}	1.89×10^{8}
Relative FE PL intensity	0.965	0.827	1	0.803
RMS (nm)	1.1	1.0	1.2	36.7/1.7
PV (nm)	9.8	21.5	29.6	321.2/20.8
The MT density (cm^{-1})	268	320	186	
The APB density (μm^{-1})	0.55	0.5	0.53	

By applying different growth conditions, it is observed that the defects still exist within the GaSb epilayer. It is demonstrated that the defects reaching the surface leads to surface roughness. Thus, the efforts to further explore of methods is necessary for preventing the defects propagation through active device structure and the interface

roughness for very thin multilayered heterostructures. Besides, considering the size of a single pixel device fabrication for optoelectronic devices it is important to present larger surfaces. Hence, the AFM scanning area is crucial in presenting more accurate statistics about the surface morphology. In order to emphasize the importance of the scanning area, the RMS value obtained from a smaller area of the sample NB3-1 is presented in Figure 4.26. The RMS value obtained from a scanning region of 25 μm^2 is 0.4 nm which is same as the best reported RMS value up to now [41] for a 900 nm thick GaSb layers grown on Si. As can be seen form Figure 4.27, for a smaller scanning area the RMS value decreases abruptly but the accuracy in the statics is lost. Hence, in this thesis, larger AFM scanning areas are preferred to provide more accurate statistics about the surface morphology of the grown epilayers.

Figure 4.27. *3D AFM image of the sample that contains 20 ML AlSb IMF layer and post annealed at 550 °C. The RMS value is determined as 0.4 nm.*

Considering the samples used in this thesis, the best value was obtained for the sample grown at 530 °C an AlSb NL thickness of 20 ML and post annealed at 550 °C for 30 min which yields an APB density and RMS value of 0.50 μm^{-1} and 0.98 nm, respectively. The best value for the MT density (186 cm^{1}) is achieved for the sample grown at 530 °C, has an AlSb NL thickness of 20 ML and post annealed at 570 °C for 30 min. These results are the best values reported for the GaSb epilayers grown on nominal substrates up to now. Besides, it was demonstrated that the thermal treatment is an effective way in the reduction of the defect density. The APB density as low as 0.48 μm^{-1} is obtained with the post-growth annealing for 60 min and by an intermediate annealing step. Also, the FWHM of 229 arcsec and the TD density of 1.72×10^{-8} cm^{-2} are achieved for the sample grown with an intermediate annealing step.

5. GROWTH OF GaSb ON Si (100) VIA GaSb NUCLEATION LAYER

5.1. Introduction

In this chapter, the growth of GaSb epilayers on Si (100) via GaSb NL are studied. It is revealed that AlSb NL is a very functional as an intermediate layer for the highly mismatched heteroepitaxy of GaSb on Si. We intend to investigate an alternative NL and its effect to the GaSb epilayers. Thus, a series of samples were grown to find out the optimum GaSb NL growth conditions.

The growth parameters of Set 4 and Set 5 are summarized in Table 5.1 and Table 5.2, respectively. For all the samples, Sb/Ga flux ratio for the GaSb NL, the GaSb epilayer and the thickness of the GaSb epilayer (1 μm) were kept identical. The samples in Set 4 and Set 5 were grown on nominal Si substrates to determine the optimum thickness and the growth temperature of GaSb NL, respectively. The growth of all the samples were monitored by RHEED: During the growth of GaSb NL, the spotty patterns were observed on RHEED screen, which indicates 3D island formation. When the substrate temperature was increased for the growth of GaSb epilayers, the clear streaky (1x3) pattern began to appear, after opening the Ga shutter.

Table 5.1. *Growth parameters for the samples in Set 4.*

Sample Code	NB4-1	NB4-2	NB4-3	NB4-4	NB4-5
Thickness of GaSb NL (ML)	2	8	24	40	80
Growth Temperature of GaSb Layer (°C)	530	530	530	530	530

Table 5.2. *Growth parameters for the samples in Set 5.*

Sample Code	NB4-4	NB5-1	NB5-2	NB5-3
Thickness of GaSb NL (ML)	40	40	40	40
Growth Temperature of GaSb NL (°C)*	350	400	450	500
Growth Temperature of GaSb Layer (°C)**	530	530	530	530

*Substrate holder thermocouple temperature
**Pyrometer temperature

5.2. The Effect of GaSb Nucleation Layer Thickness

To understand the structural quality, the FWHM values and the TD density of the samples were extracted from HRXRD RCs. As presented in Figure 5.1, the best value

is obtained from the sample NB4-4 grown with 40 ML GaSb NL. The FWHM value and the TD density are determined as 375 arcsec and 4.69×10^{8} cm^{-2}, respectively. Besides, the surface morphology of the samples are presented in Figure 5.2. All the samples exhibit APB regions. Distinctly, the MTs appear on the surface of the samples grown with GaSb NL thickness below 4 ML. The MT densities were determined as 6681 and 4463 cm^{-1} for the samples NB4-1 and NB4-2, respectively, while the MT densities extracted from the samples with GaSb NL thickness higher than 8 ML were varied in the range between 200-220 cm^{-1}. From the etched surface of all the samples, the APBs are clearly seen where the MTs are observed for the samples NB4-1, NB4-2 and NB4-5 only, as shown in Figure 5.3.

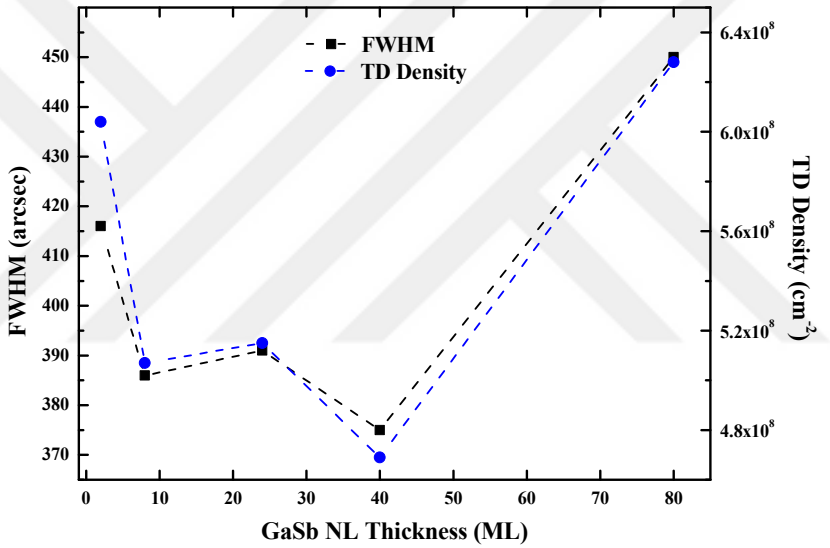

Figure 5.1. *The FWHM of X-ray RC around the (004) reflection and the TD density of GaSb epilayers as a function of GaSb NL thickness.*

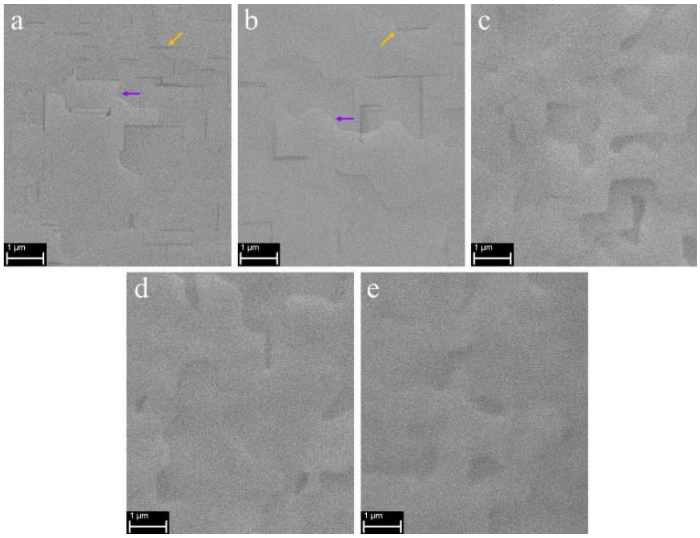

Figure 5.2. *SEM images of GaSb epilayers grown on Si with GaSb NL thickness of (a) 2, (b) 8, (c) 24, (d) 40 and (e) 80 MLs. The MTs and APBs are marked by yellow and violet arrows, respectively.*

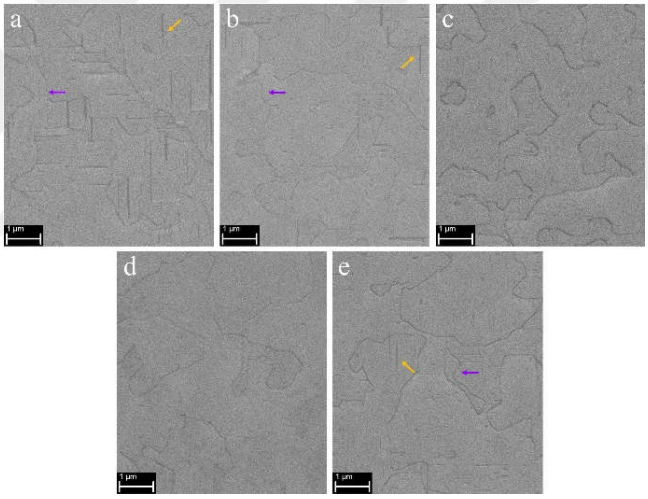

Figure 5.3. *SEM images of etched GaSb epilayers grown on Si having with GaSb NL thickness of (a) 2, (b) 8, (c) 24, (d) 40 and (e) 80 MLs. The MTs and APBs are marked by yellow and violet arrows, respectively.*

The RMS values of the as-grown samples and the APB density determined from the etched samples are presented in Figure 5.4. Depending on the GaSb NL thickness, the APB density doesn't change dramatically, since the obtained values are in the range between 0.58-0.63 μm^{-1}. The best surface roughness were observed for the samples grown with GaSb NL thickness of 24 ML (1.22 nm) and 40 ML (1.25 nm). By decreasing GaSb NL, surface roughness getting worse. Meanwhile, the surface roughness of the sample NB4-1 is increased by 32%, when compared to the sample NB4-4. As mentioned above,

the highest MT density is obtained for the samples NB4-1 and NB4-2. The MTs were observed from the etched surface of the sample with GaSb NL thickness of 80 ML (Figure 5.3(e)), as well. As depicted in Chapter 4, the surface roughness degradation is attributed to the defects, especially consisting of MTs for the samples having GaSb NL thickness of 2, 8 and 80 ML.

As a consequence of the results, the GaSb NL as an intermediate layer can assist the epitaxial growth of GaSb on Si and the 40 ML thickness of GaSb NL is decided as the optimum GaSb NL for the growth of GaSb epilayers on Si.

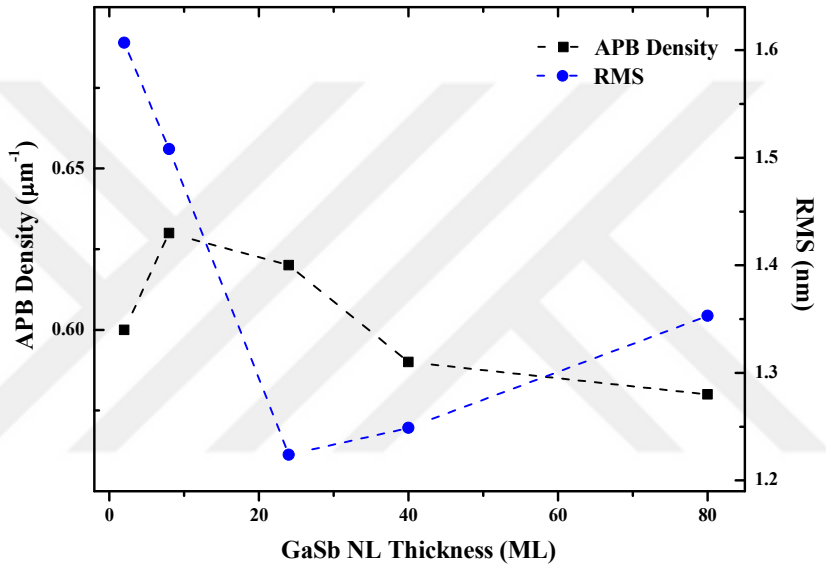

Figure 5.4. *The APB density and RMS of the GaSb epilayers grown on Si as a function of GaSb NL thickness.*

5.3. The Effect of GaSb Nucleation Layer Growth Temperature

To find out the optimum growth temperature of GaSb NL, the samples having GaSb NL thickness of 40 ML in Set 5 were chosen since the best quality was obtained by that sample. As presented in Figure in 5.5, the best FWHM (340 arcsec) and TD density (3.98×10^{8} cm^{-2}) is obtained from the sample NB5-2. Hence, the TD density is decreased by 15% by optimizing the growth temperature of GaSb NL.

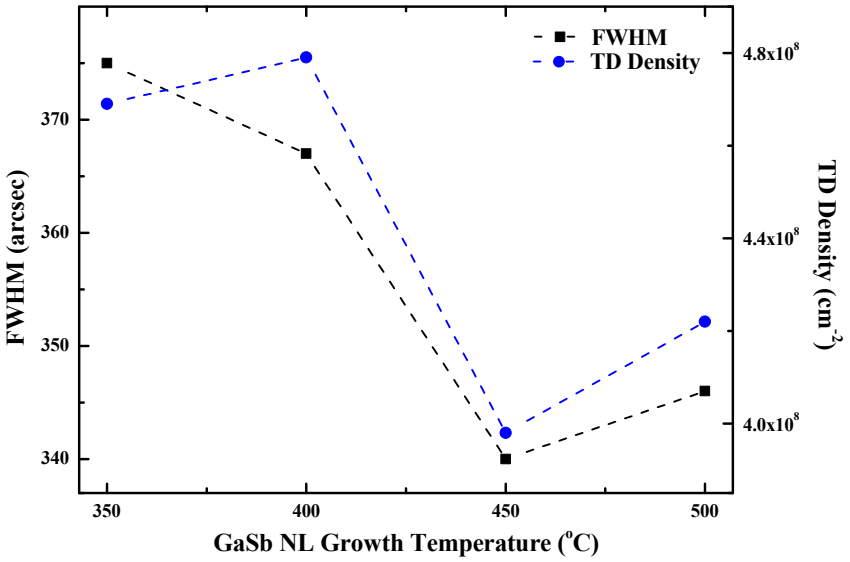

Figure 5.5. *The FWHM of X-ray RC around the (004) reflection and the TD density of GaSb epilayers as a function of growth temperature of GaSb NL.*

Depending on the growth temperature of GaSb NL, the surface morphology of the as-grown and the etched samples are shown in Figure 5.6. The RMS values of the as-grown sample and the APB densities of the etched samples are given in in Figure 5.7. Although the TD density is enhanced for the case of growth of GaSb NL at 450 ºC, the APB density is slightly increased by 8%, when compared to NB4-4. In consideration of the surface roughness, the RMS values don't varied significantly, which is expected considering the determined APB density range.

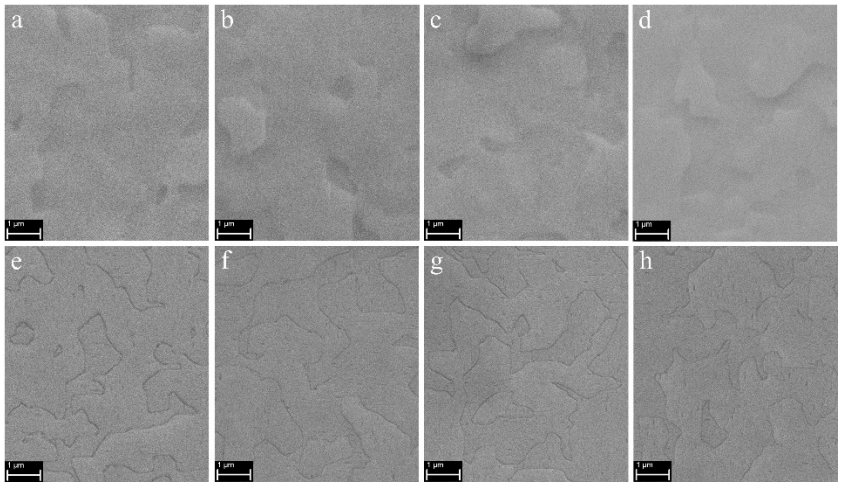

Figure 5.6. *SEM images of as-grown GaSb epilayers having GaSb NL grown at the growth temperature of (a) 350, (b) 400, (c) 450 and (d) 500 ºC. SEM images of etched GaSb epilayers having GaSb NL grown at the growth temperature of (e) 350, (d) 400, (g) 450 and (h) 500 ºC.*

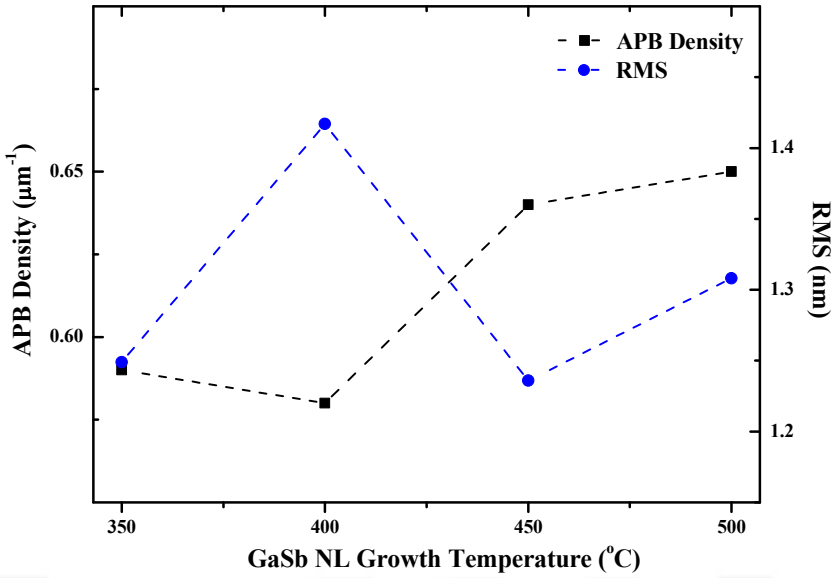

Figure 5.7. *The APB density and RMS of the GaSb epilayers grown on Si as a function of GaSb NL thickness.*

5.4. Summary and Conclusions

It is demonstrated that the GaSb epilayers are achieved with initiating GaSb NLs. As a consequence of optimizing the growth parameters, the best thickness and the growth temperature for GaSb NL is found to be 40 ML and 450 °C, respectively. In general terms, the surface roughness and the APB density exhibited a slight variation. However, the TD density could be reduced to 3.98×10^{8} cm^{-2}.

For comparison purposes, Table 5.3 summarize the obtained results from the samples grown via AlSb NL and GaSb NL under similar growth conditions. As shown in Table 5.3, the NL growth temperature differs from each other. It is attributed that the Ga diffusion length is larger than the Al on Si. Since, we acquire the optimum condition at lower growth temperatures. The sample NB1-3 with AlSb NL seems to be more effective when compared the results, but not offer a distinct difference considering the characterization methods. At this point, it should be conducted further investigations to reveal the effect of the GaSb NL and AlSb NL on the growth process in detail with the structural analysis. Nevertheless, the results indicate that the GaSb NL can also be used for the growth of GaSb epilayers with optimizing the growth parameters and using alternative methods, although most studies presents the GaSb epilayers with AlSb NL.

Table 5.3. *Summary of the obtained results for the samples NB1-3 and NB5-2.*

Sample Code	**NB1-3**	**NB5-2**
NL growth temperature (°C)	485**	450*
RC FWHM (arcsec)	302	340
TD density (cm^{-2})	3.09×10^{8}	3.98×10^{8}
RMS (nm)	1.06	1.24
The MT density (cm^{-1})	268	214
The APB density (μm^{-1})	0.55	0.64

*Substrate holder thermocouple temperature
**Pyrometer temperature

6. INVESTIGATION OF GaSb EPILAYERS GROWN WITH VARIOUS METHODS

6.1. Introduction

In this chapter, the growth of GaSb epilayers on vicinal Si (100) substrates and the growth of GaSb epilayers with SL layers are presented. By using those alternative methods, the aim is to examine the effects on the defect density and the morphology and to enhance the crystal quality of GaSb epilayers as far as possible for the consideration of Sb based device integration with Si substrates.

The GaSb epilayers with AlSb NL were grown on Si (100) vicinal surfaces with various miscut angles towards [110] direction, as presented in Table 6.1. For all the samples, the growth parameters including Al/Sb flux ratio (50), the growth temperature of the AlSb NL (485 ºC), Sb/Ga flux ratio (10), the growth temperature of GaSb epilayer (530 ºC) and GaSb epilayer thickness (1 μm) were kept identical. For the GaSb epilayers with the SL layers, two samples were grown on nominal Si (100) substrates under identical growth conditions. Those samples were named as NB7-1 and NB7-2, consisting of 10 or 166 period of 3 nm AlSb/3 nm GaSb SL layers, respectively. And, NB1-3 in Table 6.1 refers to the reference sample for comparison purposes.

Table 6.1. *The Si (100) substrate types for the samples in Set 6.*

Sample Code	Si (100) Substrate Type
NB1-3	Nominal
NB6-1	0.15º towards [110]
NB6-2	2º towards [110]
NB6-3	4º towards [110]
NB6-4	6º towards [110]

6.2. The Role of Vicinal Substrate Surfaces on GaSb Epilayers

Figures 6.1 and 6.2 represents the SEM images and 3D AFM images of the as-grown GaSb epilayers on vicinal Si (100) substrates, respectively. It is observed that the surface morphologies depends on the miscut angles where the surface roughness of the GaSb epilayers demonstrated a nonmonotonic behavior.

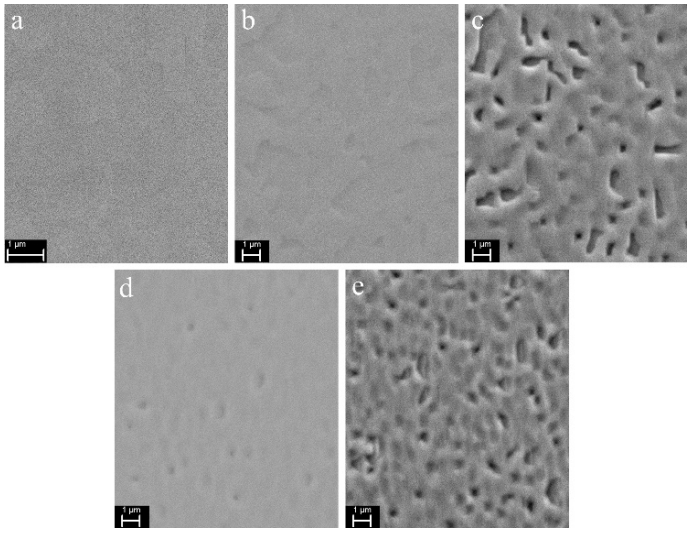

Figure 6.1. *(a) represents the SEM image of NB1-3 as a reference sample. SEM images of GaSb epilayers grown on Si (100) vicinal surfaces with (b) 0.15º, (c) 2º, (d) 4º and (e) 6º towards [110] direction.*

For the NB6-1 grown on vicinal Si (100) surface with low miscut (0.15º), a similar surface morphology was observed, compared to GaSb epilayers on nominal Si (100) (Figure 6.1(a) and (b)). While the GaSb epilayers grown on vicinal Si (100) substrates with miscut angles of 2º and 6º exhibits a rough surface (Figure 6.1(c) and (e)), smoother surface was obtained for the one grown on 4º miscut Si substrate. In general, the surface roughness of the epilayers is increased for all the samples in Set 6 compared to the sample NB1-3 which was grown on nominal substrate (Figure 6.2). The surface roughness of the samples are determined as 2.40, 9.17, 4.66, and 12.95 nm for NB6-1, NB6-2, NB6-3, NB6-4, respectively. From the results, it can be said that the best surface morphology is obtained from the sample grown on the lowest angle miscut Si substrate.

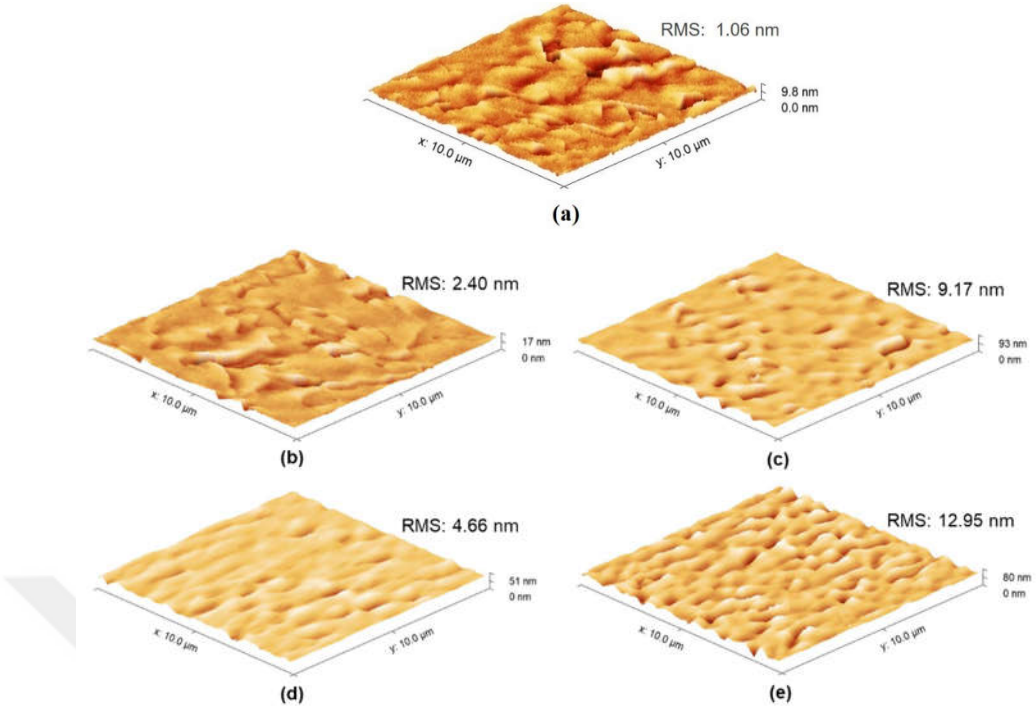

Figure 6.2. *(a) represents the 3D AFM image of NB1-3 as the reference sample. 3D AFM images of GaSb epilayers grown on Si (100) vicinal surfaces with (b) 0.15°, (c) 2°, (d) 4° and (e) 6° towards [110] direction.*

As presented in Figure 6.3, the best FWHM value and the lowest TD density are found as 259 arcsec and 1.98×10^{8} cm^{-1}, respectively, for the sample grown on vicinal Si (100) substrate with a miscut angle of 4°. Besides, the APB density is deduced from the SEM images of the samples and Figure 6.4 represents the etched sample surfaces. Once again, the APB density dramatically decreases down to a value of 0.06 μm^{-1}, for the sample NB6-3, as shown in Figure 5.3. The other important result obtained from the SEM images of etched sample surfaces is the observation of significant closed-loop boundaries. It indicates that the size of APDs decreases in the case of using vicinal Si (100) substrates with high miscut angles (2°-6°). Hence, it is the evidence of the self-annihilation of APBs during the growth thanks to the miscut Si substrates [84].

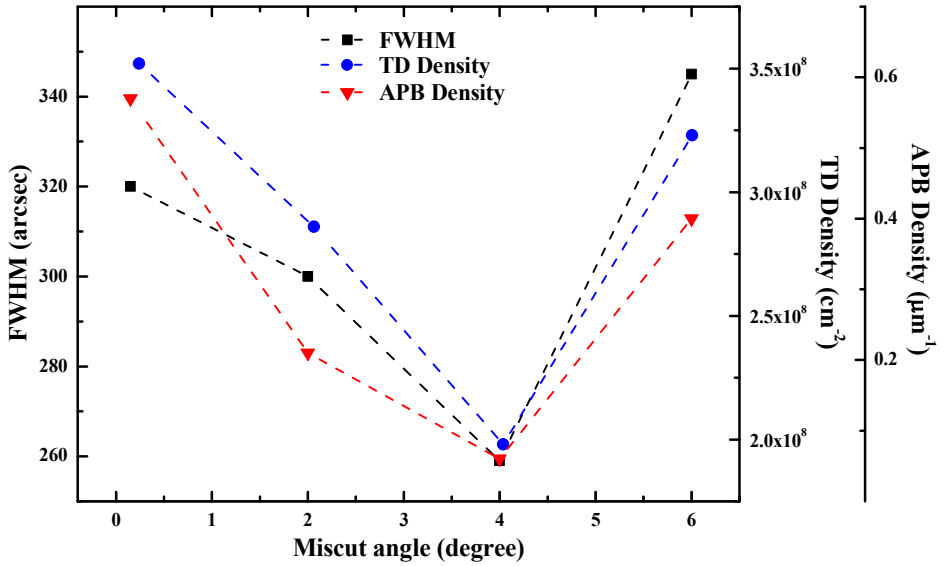

Figure 6.3. *The FWHM of X-ray RC around the (004) reflection, the TD and APB densities of the samples having miscut angles of 0.15, 2, 4 and 6º. The dotted lines are guide for the eyes. The APB density is obtained from etched samples.*

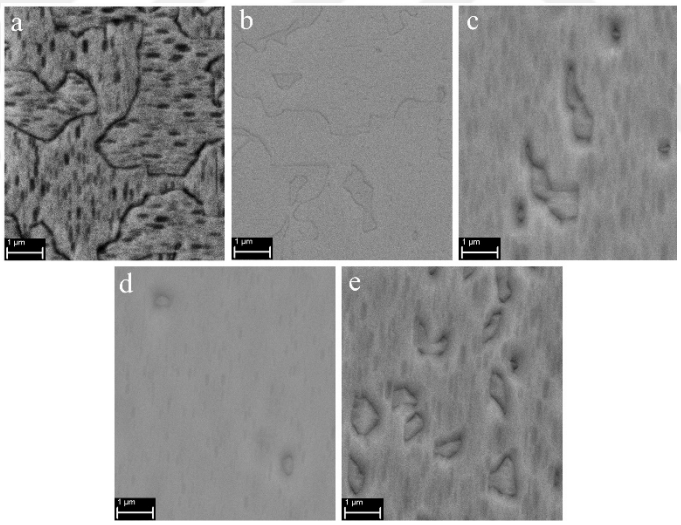

Figure 6.4. *(a) represents the SEM image of NB1-3 as the reference sample. SEM images of etched GaSb epilayers grown on Si (100) vicinal substrates (b) 0.15º, (c) 2º, (d) 4º and (e) 6º towards [110] direction.*

The vicinal Si substrates with low angle exhibits single height type surface configuration. As the miscut angle is increased, a surface with double-height step configuration mostly occurs [121] and so the double step height type can facilitates the suppression of APDs. Therefore, the abrupt change of the profile of the APB density and APD variation between the samples grown low and high angle miscut Si substrates basically hinges on the miscut angle of the vicinal Si substrates. On the other hand,

as illustrated in Figure 6.5, the miscut angle (θ) of the vicinal substrates alter the step length (L) and the number of the steps. Increasing the miscut angle yields the increase in the step length and the number of the steps. Besides, it is known that the AlSb NL generates IMF dislocations along the interface [38]. Therefore, the APB density variation between the high miscut Si substrates may be attributed to the relation between the step length and IMF array spacing. If the step length is longer but shorter than the IMF array spacing, this may introduce the increment in points between the step edge and the IMF dislocations, resulting in rather large defect density [30]. As depicted from the AFM images, it also may affect surface roughness.

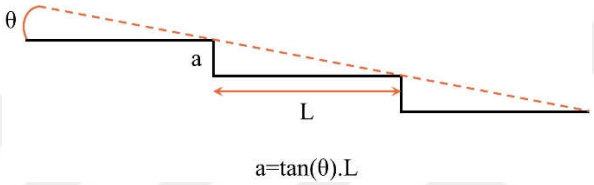

Figure 6.5. *Step geometry of vicinal Si (100) substrate.*

6.3. The Growth of GaSb Epilayers with Superlattice Layers

Figure 6.6 presents the structure of GaSb epilayers grown with SL layers. The main difference between the NB7-1 and NB7-2 is the SL period number; the NB7-2 is considered as a GaSb SL buffer layer due to the high number of periods. Also, the XRD pattern of NB7-2 in Figure 6.7 denotes the growth of GaSb epilayers with SL layer, successfully.

NB7-1		
GaSb layer	790 nm	
GaSb/AlSb	3/3 nm	x10
GaSb layer	200 nm	
AlSb NL	20 ML	
Si (100) Substrate		

NB7-2		
GaSb layer	300 nm	
GaSb/AlSb	3/3 nm	x166
GaSb layer	200 nm	
AlSb NL	20 ML	
Si (100) Substrate		

Figure 6.6. *Schematic representation of GaSb epilayer structures of the samples NB7-1 and NB7-2.*

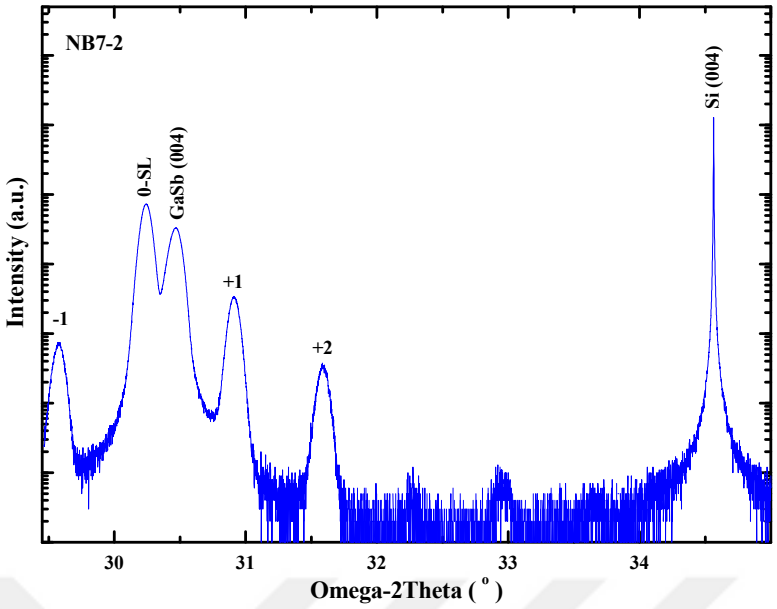

Figure 6.7. *The XRD pattern of the sample, NB7-2.*

The surface roughness of the samples NB7-1 and NB7-2 are determined as 1.13 nm and 0.90 nm, respectively. No distinct difference from the samples in Set 1-3 is observed for these samples. As presented in Figure 6.8, a surface including APBs and MTs are obtained.

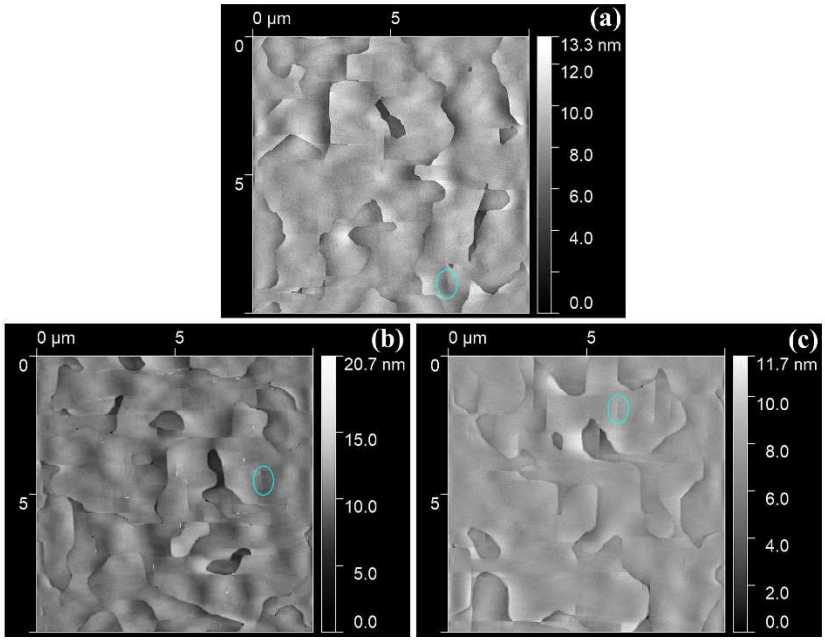

Figure 6.8. *(a) represents the 2D AFM image of NB1-3 as the reference sample. 2D AFM images of GaSb epilayers grown on nominal Si (100) substrates (b) NB7-1 and (c) NB7-2. The blue circles denote the MTs.*

When the surfaces of the etched samples, NB7-1 and NB7-2, are examined, the APBs density is decreased significantly for NB7-2. The APB densities are calculated as 0.58 and 0.36 μm^{-1} for NB7-1 and NB7-2, respectively. This result shows that it is achieved to reduce the APB density down to 0.3 μm^{-1} range, which is close the value obtained from the sample grown on low angle miscut Si substrate (NB6-1). Moreover, a better surface roughness is obtained when compared to NB6-1.

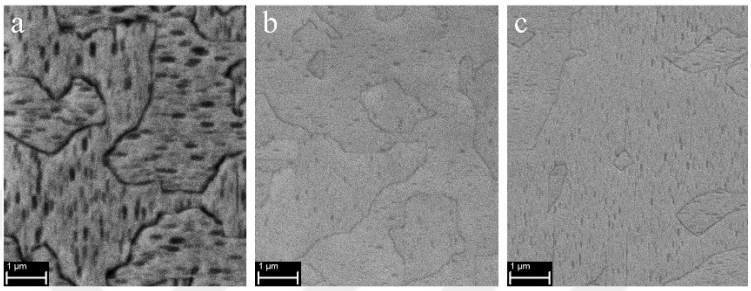

Figure 6.9. *(a) represents the SEM image of NB1-3 as reference sample. SEM images of etched GaSb epilayers grown on nominal Si (100) substrates (b) NB7-1 and (c) NB7-2.*

6.4. Conclusions

The GaSb epilayers grown on miscut Si (100) substrates are studied systematically with regard to the miscut angle. The obtained results are summarized in Table 6.2. From the results, the MTs are not observed on the surface of the samples and the closed-loop boundaries are appeared as a result of the annihilation of the APBs. Among the vicinal substrates, the use of vicinal Si substrate with 4^o miscut angle provides the suppression of APBs. When compared to the reference sample grown on nominal substrate, the APB density is reduced by 90% and the TD density is decreased by 35%. The results put the importance of the choice of degree of miscut. In addition to those, the surface roughness is severely increased, which may affect the growth of SL device structure on such rough buffer epilayer. Hence, this means that the growth of the highly mismatched GaSb on Si still needs to be improved.

For the GaSb epilayers with SL layer, increasing the number of SL period lead to the reduction of the APB density, significantly, without surface roughness degradation, but larger size APDs appears on the surface. It indicates that the SLs in the GaSb epilayer has a role as a dislocation filter for the defects by preventing them to propagate towards the surface. However, in terms of defects, to use a Si vicinal substrate with low angle will

be more advantageous with regard to the time consuming issue, when considered the similar results between NB6-1 and NB7-2

Consequently, the crystal quality of GaSb epilayers can be improved by using vicinal Si substrates and SLs as dislocation filters. Also, the growth process can be diversified via the combinations of all such methods, including thermal treatment.

Table 6.2. *Summary of the obtained results for the samples in Set 6 and Set 7.*

Sample Code	**NB1-3**	**NB6-1**	**NB6-2**	**NB6-3**	**NB6-4**	**NB7-1**	**NB7-2**
RC FWHM (arcsec)	302	320	300	259	345		
TD density (cm^{-2})	3.05×10^{8}	3.52×10^{8}	2.86×10^{8}	1.98×10^{8}	3.68×10^{8}		
APB density (μm^{-1})	0.55	0.36	0.21	0.06	0.4	0.58	0.33
RMS (nm)	1.06	2.40	9.17	4.66	12.95	1.13	0.90

7. GROWTH OF GaAs NANOWIRES ON Si (111)

In this chapter, to examine the effect of growth temperature, Ga growth rate and group V/III ratio on the structure of the GaAs NWs, the Set 8 and Set 9 series were grown on Si (111) substrates, which were purchased from Virginia Semiconductor Inc. and Siltronix, respectively. The native oxides of the Si wafers were ~1.7 nm for Virginia Semiconductor Inc. and ~1.3 nm for Siltronix as determined by ellipsometer. If the surface is covered with SiO_x, the oxide thickness should be thin enough to initiate NW growth from beneath the Si surface [90]. The native oxide thicknesses of both substrates are in a proper range according to the reported critical thickness of native oxide for NW growth [69].

7.1. The Effect of Growth Temperature

To examine the effect of growth temperature, GaAs NWs were grown on three different Si (111) substrates which were purchased from Virginia Semiconductor Inc. and the growth parameters were summarized in Table 7.1. During the growth, the crystal phases in respect to the growth temperatures were monitored by RHEED patterns at regular intervals. After the growth, the samples were analyzed by both SEM and TEM techniques.

Table 7.1. *Growth parameters for the samples in Set 8.*

Sample Code	Ga 2D Growth Rate (nm/s)	Group V/III Flux Ratio	The Growth Temperature (^oC)
NBW-1	0.22	20	580
NBW-2	0.22	20	600
NBW-3	0.22	20	620

Figure 7.1 presents tilted view SEM images of GaAs NW samples obtained from the samples in Set 8. Depending on the growth temperature, vertical and tilted GaAs NWs in altered amounts are observed on the substrates. As it can be perceived from Figure 7.1, in addition to the GaAs NWs, the surfaces of the substrates contain parasitic growth, which seems to be converted to larger clusters with increasing growth temperature. Parasitic growth, which is the formation of polycrystalline structures on the substrate surface between the NWs, can be observed during the growth of group III-V NWs on the Si surface with/without native oxide or patterned Si surface [65-66, 68, 91, 122-124]. It was reported

that the sticking coefficient of Ga (s_{Ga}) is ~1 for the temperature below 565 ºC and it is not possible to precipitate Ga adatoms on the native oxide for the temperature higher than 650 ºC [125]. Thus, the sticking probability of Ga adatoms on the native oxide would decrease with increasing the growth temperature from 580 ºC up to 620 ºC due to the desorption of Ga adatoms from the surface with a fraction of (1- s_{Ga}) [126]. In the case of the growth at comparably low temperature, GaAs polycrystalline structures fully coats the surface. Conversely, huge GaAs clusters formed on the sample surface slightly separated from each other for the growth temperature of 620 ºC, as seen in Figure 7.1. Besides, the growth condition under high Ga growth rate and As/Ga flux ratio also naturally triggers the large amount of parasitic growth on the Si surface with native oxide.

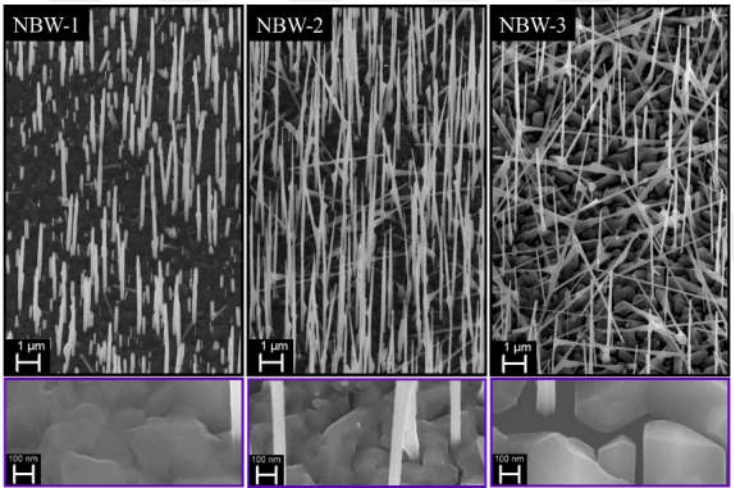

Figure 7.1. *Tilted-view SEM images of the samples of NBW1-2-3. The SEM images of the parasitic growth regions on the sample surfaces are framed in violet.*

Examining SEM images infers that the Ga droplets are missing at the tip of NWs. For a deeper analysis, the EDS was performed for NBW-1 and presented in Figure 7.2. The acquired EDS spectra from the regions 1 and 2 reveal that the regions comprise of both Ga and As elements as well as the tip of GaAs NW (region 1). Hence, NBW-1 doesn't have a Ga droplet with a round shape, instead a crystalline tip was detected, as it is seen from the inserted TEM images in Figure 7.2(a). In addition to NBW-1, the same result was obtained for the samples NBW-2 and NBW-3, which indicates that group V/III ratio effects

the Ga droplet preservation in all the samples grown at the indicated growth conditions. Some studies reveal that the Ga droplet may be consumed under As flux and is transformed into a needle like structure or crystalline tip [64, 127]. Obviously, due to the high group V/III ratio the vanishing of Ga droplets was established [65, 128]. The crystalline tip of NWs denotes that As-rich condition (group V/III=20) used in this set of samples can be a factor for the depletion of Ga droplets during the growth or the cooling process (the As shutter was closed after the Ga shutter with a delay of 47-70 sec). Although further investigations should be performed, it is believed that the vanishing of the Ga droplets during the growth is more probable considering the morphology of NWs (which will be depicted later in this chapter). Additionally, this action could have a role on the contribution to parasitic growth following the Ga droplet consumption.

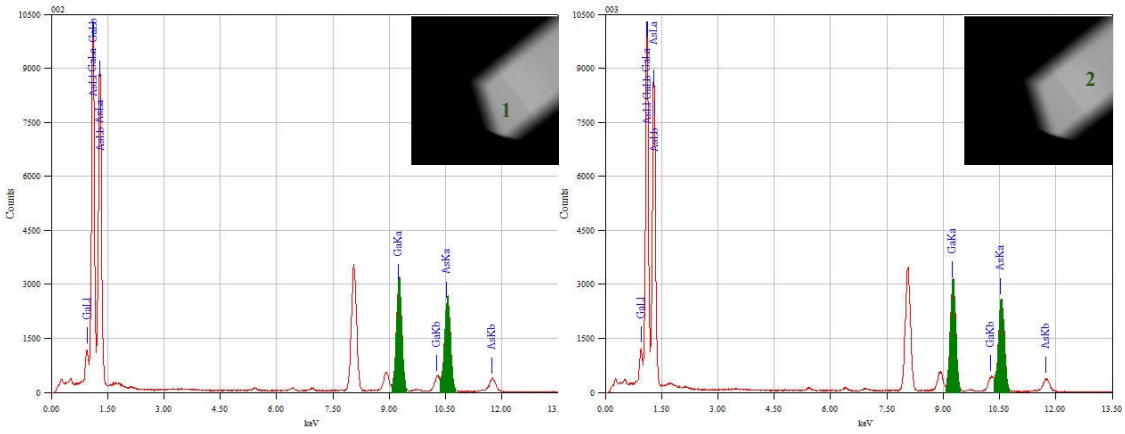

Figure 7.2. *EDS profile of a NW extracted from NBW-1 which belongs to (a) the tip of NW (region 1) and (b) just below the tip of NW (region 2).*

The growth rate of group III-V NWs is determined by group V flux, as distinct from the growth of 2D epitaxial layers. It means that the axial growth of GaAs NWs is driven by As adatoms incorporated with the Ga, subsequent to the impingement of As atoms on the Ga droplets and diffuse towards the interface [129]. Thus, the growth rate depends on the As flux significantly [92, 128-129]. Depending on the growth temperature, the average NW length of NBW-1-2-3 were determined as 7.2, 11.2 and 8.5 μm, respectively, as shown in Figure 7.3. Accordingly, the growth rates were calculated as 4.1, 6.1 and 4.7 nm/s for

NBW-1-2-3, respectively. It is obvious that the growth rates of NWs are much higher than the 2D growth rate of Ga which is 0.22 nm/s. It brings out that the main contribution to the NW growth is provided by the incorporation of adatoms via the droplets [130]. Besides, in the case of the existence of the Ga droplets, Ga adatoms preferentially feed the Ga droplets [129]. Hence, the high group V/III flux ratio results in an enormous increase in the growth rate.

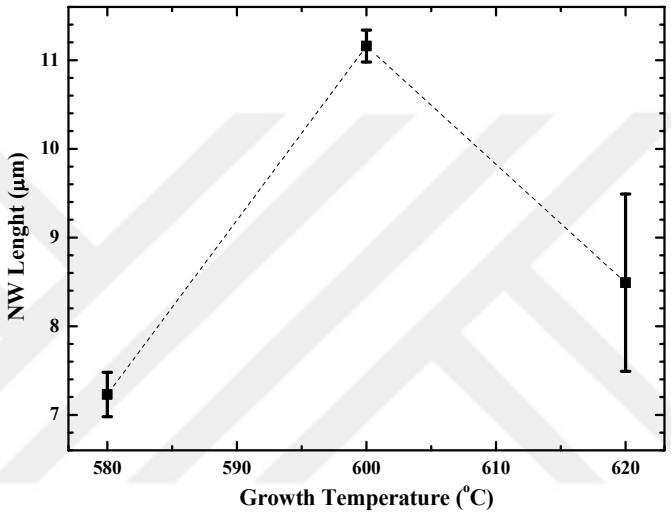

Figure 7.3. *The average length of NWs obtained from the samples in Set 8 as a function of growth temperature.*

Another important point is that, the length of GaAs NWs exhibits a nonmonotonic variation with the growth temperature (Figure 7.3). Namely, above 600 °C, the lengths of GaAs NWs decrease as reported previously by several Authors [124, 128, 130-132] where this behavior can be attributed to the thermally limited diffusion [131]. Above 600 °C, the desorption process is dominant which limits the contribution of Ga and As atoms to the NW growth. In addition, this would lead the reduction of the Ga droplets on the native oxide. The Ga droplet density formed on native oxide is influenced by the growth temperature and it is inversely related to the growth temperature increment [133-134].

While the highest NW density was obtained from NBW-2 grown at 600 °C, it decreases above 600 °C (Figure 7.4). With increasing growth temperature, the Ga deposition rate is decreased due to the shorter effective diffusion length [135] which indicates a crucial impact on the NW density by initial growth stage. From Figure 7.4, both the vertical and non-vertical

NWs densities were obtained. Although vertical NWs are generally favoured at high group V/III ratios [136], it shows an alteration depending on the growth temperature. For the growth temperature at 600°C, the highest NW density was observed but the non-vertical NWs were emerged. The drastic decrement in the vertical NW density occurred at the highest growth temperature, where the lowest NW density was obtained as well as almost equal vertical and non-vertical NWs densities.

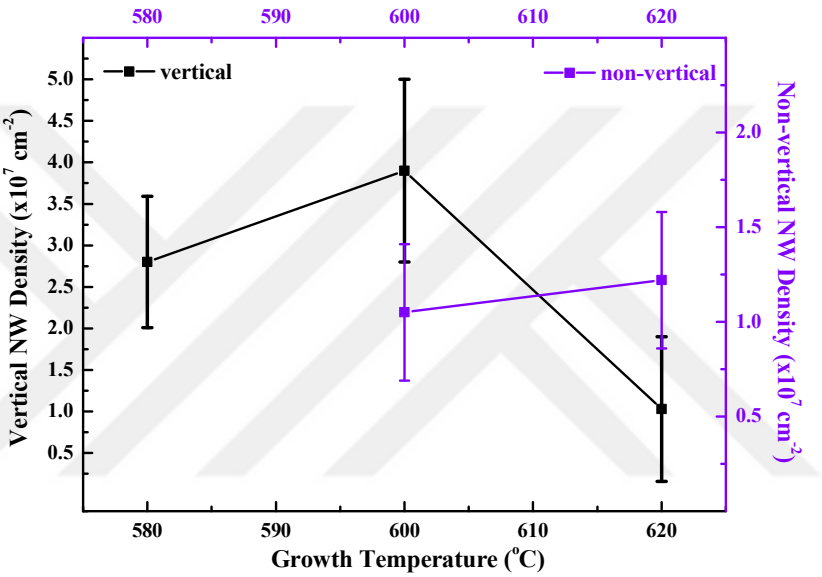

Figure 7.4. *The variation of vertical and non-vertical NW density with respect to the growth temperature.*

The density of vertical NWs hinges on the initial nucleation stage and it strongly depends on the growth parameters (the temperature, group V/III flux, the droplet contact angle/size and the native oxide layer). In the VLS growth, group III-V NWs initiate in the directions that minimize the surface free energy at the interface between the NW and the catalyzer. For instance, the V-terminated (111)B surface is favourable for the vertical ZB-NW yield because of its lowest surface free energy, while the inclined NWs are formed on the group III-terminated (111)A surface. But, group III-V NW growth on Si substrate has its own challenges since Si has a polar nature and four equivalent (111) oriented surface exist [137]. During the initiation stage, a change in the polarity lead to vertical or inclined NW growth in a direction of 90° or 19.5° from Si substrate surface or 3D multiple twinning can

occur [68, 138]. That is the reason for observing NWs having different angles different than 90 and 19.5^{o} [68, 138]. In our case, the angle between the inclined NWs and the surface were found as 31, 35 or 56^{o} for the samples NBW-2 and 3. This result remarks that multiple-order twinned seed could form at the interface during the initial growth stage. At this point, it can be outlined that the relative Ga droplet size and its sorption current are the key parameters, which are influenced by the growth temperature and the effective group III/V ratio. For the samples NBW-1 and 2, which were grown at the lower temperature regime, the growth condition should be enabled to an As terminated (111)B surface interface, since vertical GaAs NWs were observed mostly. In the case of the growth temperature higher than 620 ^{o}C, it is believed that the effective group V/III ratio [136] is decreased due to the high As desorption rate from the Ga droplet, which induces an increase in the Ga droplet size [138] as a result of the effective collection area of Ga adatoms [136]. Hence, the size of the Ga droplet exceeds the top surface of GaAs seed, and the new {111} facets are favourable, resulting in the growth of non-vertical GaAs NWs. If the group V/III ratio is increased for the growth temperature of 620 ^{o}C, the increment in the density of vertically aligned NWs will be expected.

Depending on the growth temperature, the change on the shape of GaAs NWs was deduced from the SEM analysis. As illustrated in Figure 7.5 (a-b), the tapering is observed for NBW-2 and NBW-3, while convex like structure is identified for NBW-1. Mainly, the size of the NW is determined by the catalyzer diameter [64, 124, 139-140]. However, the diameter and shape of NWs may vary with growth kinetics as well. Since the Ga droplet depletion is detected for all samples, it is believed that the consumption of Ga droplets under high group V/III ratio results in the tapering of NW structure for the samples of NW-1 and NBW-2 (Figure 7.5(c)). On the other hand, the axial and radial growth should be take into account as well. Although, the NW growth is commonly occurred in the axial direction, the radial growth may also contribute to the NW growth which is based on the diffusion of adatoms through NW sidewalls. Besides, it is known that the axial growth does not proceed after the Ga droplet depletion [64-65].

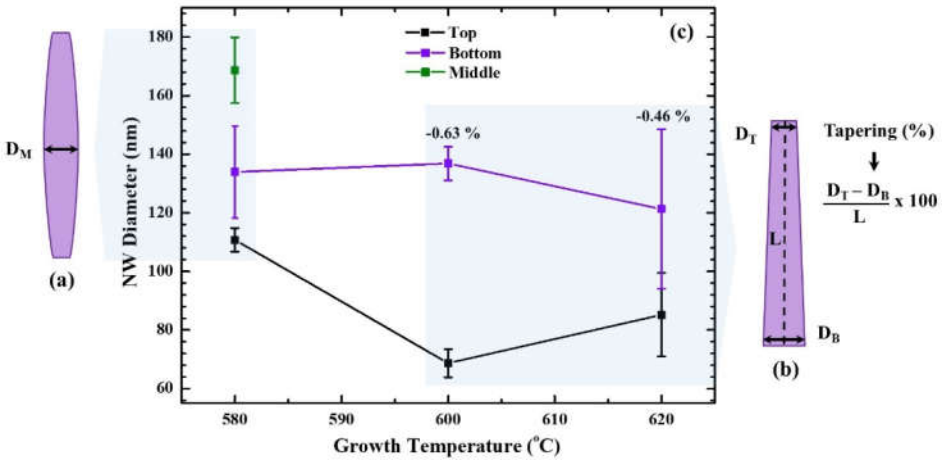

Figure 7.5. *(a) The illustration of convex-like NW, (b) the illustration of inversed tapered NW and the tapering formula* and *(c) the variation of NW diameter with respect to the growth temperature; the tapering amounts are specified on the graph.*

Other than that, branch-like formations are identified on the GaAs NWs grown at the temperature above 580 ºC. Figure 7.6 shows the individual GaAs NWs separated from substrates by drop casting. Especially, the branches appear significantly on the sample NW obtained from NBW-3 (Figure 7.6(c)). It is known that the critical diameter of GaAs NWs is ~ 110 nm [130]. The diameter of GaAs NWs through the bottom regions was demonstrated as >110 nm in Figure 7.5(c). Therefore, the lateral stress could be arisen, which causes branch-like formations towards <110> direction, although the free surface energy is higher than <111> direction [141]. It seems that increasing the growth temperature might actuate this process. Although more studies should be performed to clarify the convex-like structure of nanowires achieved from the sample NBW-1, considering the branching point with respect to the bottom of the nanowires in NBW-2 and NBW-3 which is around 3.2 μm (that is almost the half of the lengths of nanowires obtained from the sample NBW-1), it could be proposed that the enlargement in the radial direction occurs in all the samples but due to the comparably low temperature, the diffusion length of Ga adatoms on the sidewalls of the nanowires decreases in the sample NBW-1 and instead of forming branches only an enlargement (convex-like structure) in the diameter of the NWs was observed in that sample.

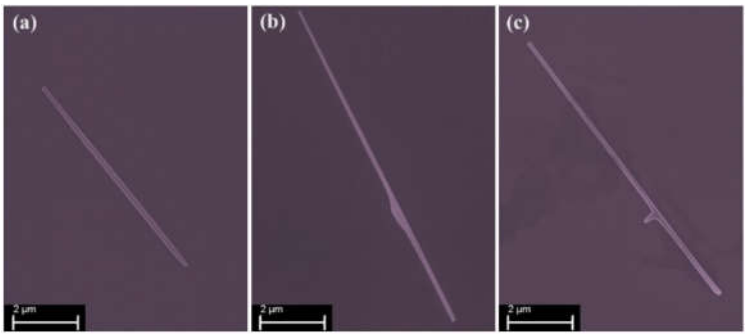

Figure 7.6. *SEM images of the individual GaAs NW samples gathered from (a) NBW-1, (b) NBW-2 and (c) NBW-3.*

When RHEED diffraction patterns are analysed, a spotty RHEED pattern pronounced gradually with increasing growth time, indicating the self-catalysed VLS growth [92] (Figure 7.7(a)). For NBW-1, initially, twinned ZB NW crystal phase is observed. The twinned ZB diffraction pattern along [011] direction is attributed to the rotational twin defects due to the stacking fault sequence alternation [142]. After 1 min, twinned ZB/WZ mixed phase begin to appear (Figure 7.7(b)). Once again, the RHEED pattern demonstrated twinned ZB crystal phase at the growth time of 15 min (Figure 7.7(c)) and it turns into WZ/ZB mixed phase at the end of the growth (Figure 7.7(d)). ZB crystal structure in [011]/[112] directions corresponds to WZ crystal structure in [0112]/[0110] directions. While it is nearly impossible to distinguish the ZB phase in [112] direction and WZ phase in [0110], due to the similar diffraction patterns [101], the RHEED pattern along [011]/[0112] direction evidenced mixed WZ/ZB phase as marked in Figure 7.7(d). Thus, the transformation is attributed to relatively thick WZ and ZB layers that occurs at the beginning and the end of NWs' growth. On contrary, the sample NBW-2 exhibits only twin ZB-WZ mixed phase during cooling process at 500 ^{o}C. In other words, it can be said that NBW-2 is predominantly twinned ZB in structure. For the two samples, following the Ga shutter close, the mixed phase pattern may imply WZ phase formation during the consumption of Ga droplets. Unfortunately, the RHEED pattern couldn't be recorded reliably for the sample grown at the highest growth temperature due to the very low RHEED intensity.

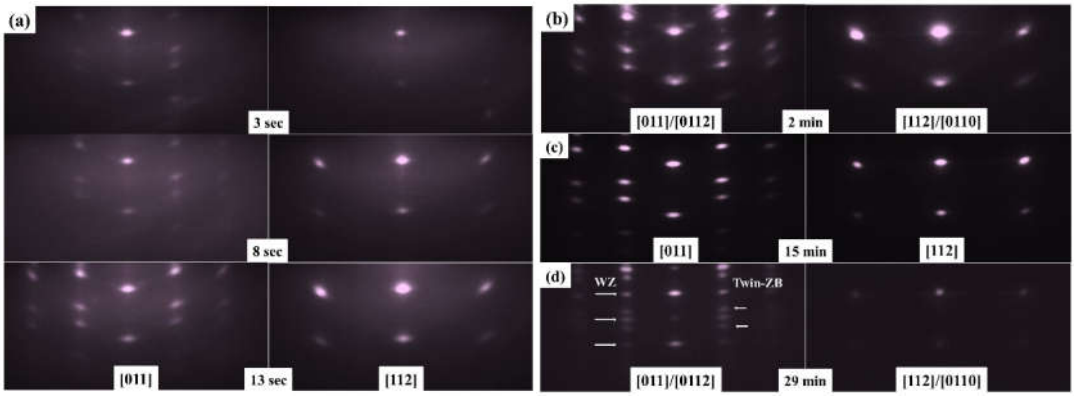

Figure 7.7. *Time evolution of RHEED patterns observed during the growth of NBW-1, (a) showing the appearance of spotty RHEED patterns gradually and the formation of twinned ZB phase at the initial stage, (b) indicating ZB/WZ mixed phase at the growth time of 1 min, (c) showing the transition to twinned ZB phase at the growth time of 15 min and (d) the re-observation of twinned ZB and WZ spots at the end of the growth. Twinned ZB and WZ spots are denoted by white arrows.*

Among all the samples, TEM analysis of NBW-1 was performed. GaAs NWs were randomly distributed on the grid and TEM images were obtained and presented in Figure 7.8. As can be identified from the contrast difference, each NW seems to contain mixed crystal phases or planar defects. Definitely, further examinations are required for the clarity of the whole crystal structure of the GaAs NWs but the multi-twin region was observed as shown in Figure 7.9. Comparing the diffraction patterns of the regions 1 and 2 on GaAs NW, the point 1 represents ZB crystal structure and the point 2 indicates the twin boundary as confirmed by SAED pattern. This situation confirms the twin fault, which usually occurs during the nucleation formation due to the alteration of the free energy depending on the contact angle of the droplet with respect to the solid-vapor facet [143].

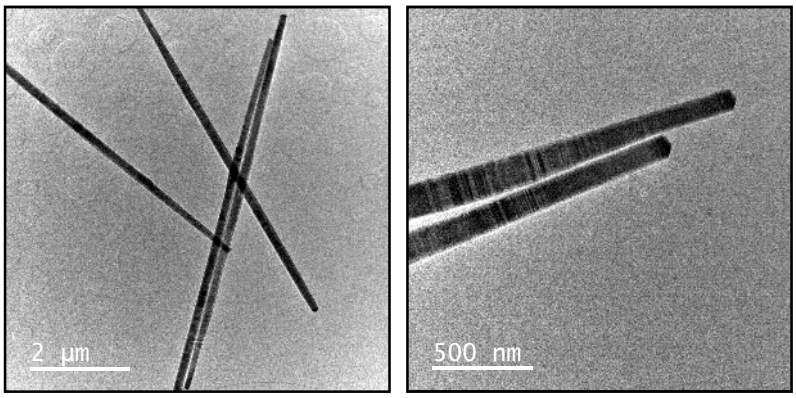

Figure 7.8. *TEM images of the NWs collected from NBW-1.*

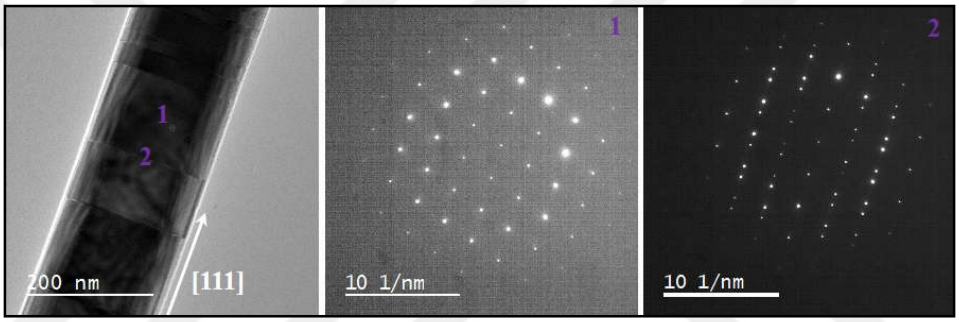

Figure 7.9. *TEM image of a GaAs NW obtained from the sample NBW-1. The SAED patterns captured from the regions 1 and 2 on the GaAs NW indicates ZB phase and twinned ZB phase, respectively.*

Besides, EDX mapping was performed on the middle region of a GaAs NW. Figure 7.10 shows that Ga and As elements are almost evenly distributed, indicating a uniform GaAs chemical phase. The atomic concentrations are found as 51% and 49% for Ga and As elements, respectively. In addition, Figure 7.10(b) and (e) display that the GaAs NWs are oxidized which is an undesirable case. It is known that the native surface oxides of group III-V semiconductor are lack of stability, inducing interfacial defects [144]. It takes precedence over NWs having the increased surface/volume ratio, which alters the electronic properties of the NWs [145-146].

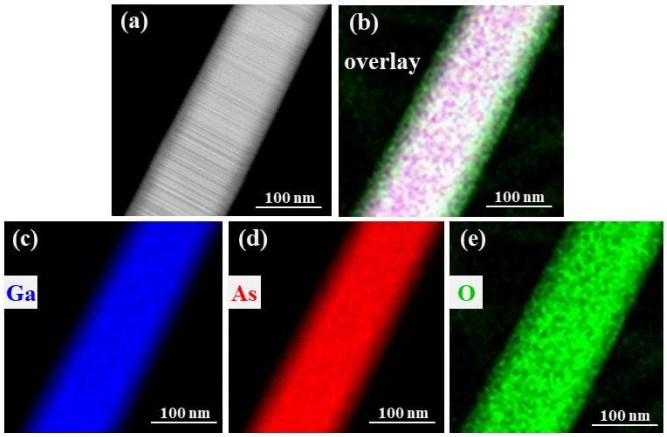

Figure 7.10. *(a) The TEM image and (b) EDS mapping of a single GaAs NW from NBW-1 and (c-e) corresponding elemental distribution maps of Ga-K, As-K, O-K, respectively.*

7.2. The Effect of Group III and V Flux

To understand the general characteristics of GaAs NWs in terms of change in the Ga growth rate and group V/III flux ratio another set of samples were grown (Table 7.2). For the samples in this set, SEM analysis were performed and SEM images are presented in Figure 7.11. Comparing the Figure 7.11(a) with Figure 7.11(b-c), it is clearly seen that the residuals on the surface significantly decrease with reducing the Ga growth rate. As mentioned in Section 7.1, it is interpreted that the high Ga rate may have a role in the amount of residuals on the surface. Here, the result apparently confirms that the parasitic growth can be suppressed by optimizing the Ga flux for a chosen growth temperature.

Table 7.2. *Growth parameters for the samples in Set 9.*

Sample Code	Ga 2D Growth Rate (nm/s)	Group V/III Flux Ratio	Growth Temperature (ºC)	Duration (min)
NBW-4	0.18	20	580	20
NBW-5	0.07	20	580	20
NBW-6	0.07	80	580	20

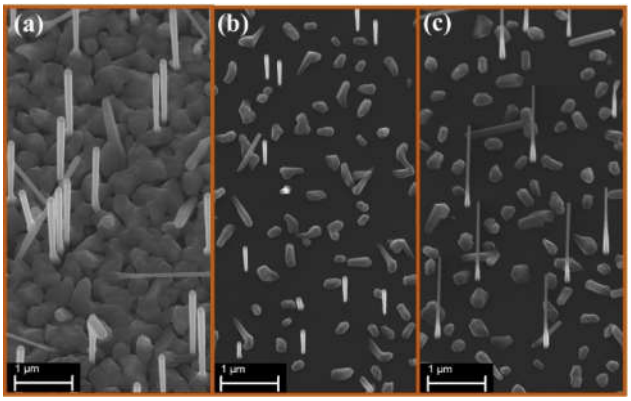

Figure 7.11. *Tilted-view SEM images of the samples (a) NBW-4, (b) NBW-5 and (c) NBW-6.*

The effect of increase in the As flux on the length of GaAs NWs is clearly observed by comparing NBW-5 and NBW-6, as seen in Figure 7.11. Besides, it seems that the increment in the Ga flux significantly increases the average length of the GaAs NWs, as well (Figure 7.12). However, as discussed below this is not true. To confirm the effect of group V/III flux ratio, GaAs NWs were grown in addition to NBW-4-5-6 samples. The results reveal that the increment in the length of GaAs NWs changes linearly with increasing the group V flux for a fixed Ga growth rate, as presented in Figure 7.13. Besides, for a fix group V flux, Figure 7.13 further corroborates that the NW growth rate is almost independent from the group III flux.

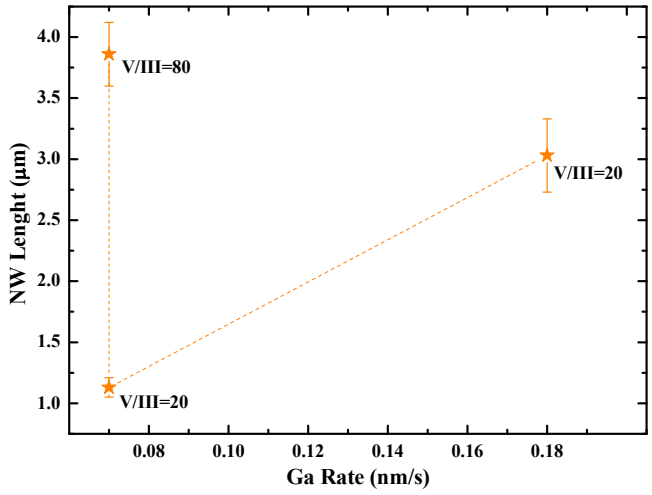

Figure 7.12. Average length of NWs as *a function of Ga growth rate and group V/III flux ratio.*

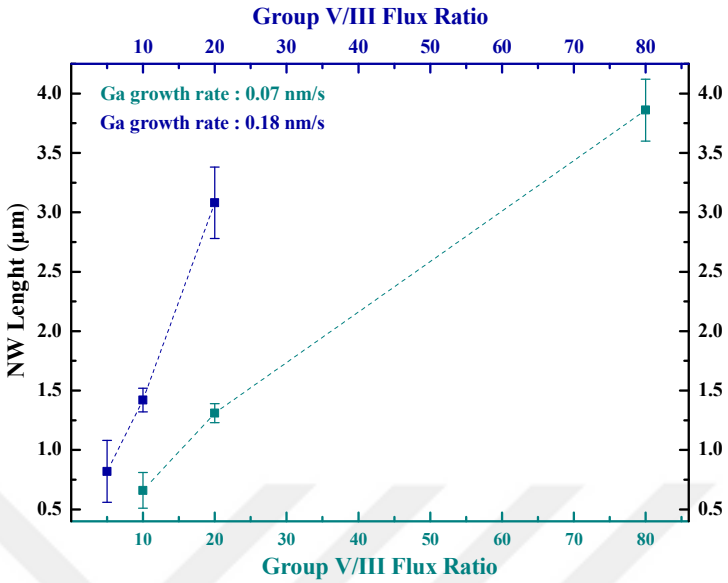

Figure 7.13. *The role of group V flux on the average length of GaAs NWs grown at 0.07 and 0.18 nm/s Ga growth rates.*

The average diameters obtained from TEM analysis are 116.6 nm and 52.8 nm for NWs extracted from the samples NBW-4 and NBW-5, respectively. More Ga flux leads to larger droplets. Hence, the result reveals that it is possible to tune the diameter of the NWs by optimizing the Ga growth rate. The average NW densities are calculated as 1.93×10^7, 1.61×10^7 and 1.38×10^7 cm^{-2} for the samples NBW-4-5-6, respectively. It is seen that the change of Ga flux variation does not show an impact on the NW density, significantly [133]. As presented in Figure 7.14, the other important observation is slightly inverse tapering morphology. The tapering is calculated as 0.009% and 0.011% for the samples NBW-4 and NBW-5, respectively. It gives the hint of enlargement of Ga droplet during the growth. It is known that under higher Ga growth rate conditions, the higher impingement of Ga adatoms may increase the Ga droplet size as a function of time [128,130].

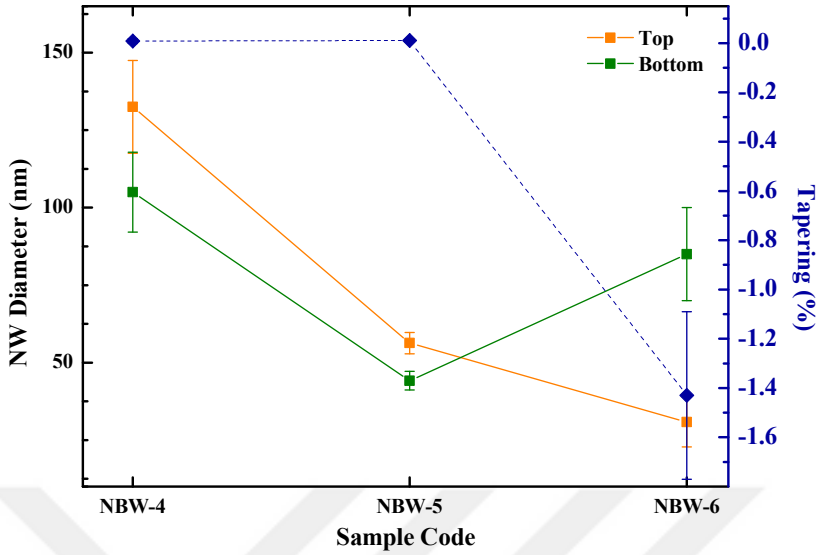

Figure 7.14. Average diameter and tapering obtained from the GaAs NWs.

On the other hand, instead of inverse tapering, the tapered shape was observed for the NWs gathered from sample NBW-6 (Figure 7.14). Also, the Ga droplets were not seen in TEM analysis, as presented in Figure 7.15(c). As it is seen, the transition of the morphology is based on the high group V/III flux ratio. We especially kept the growth time shorter than the Set 8 samples. Even so, the shrink of Ga droplets may occur due to the much higher group V flux. Therefore, -1.43% tapering occurred under excessive group V flux, resulting the consumption of Ga droplets during the growth time or the cooling period, by the excess As contribution to the process. Focusing on the diameter, NBW-6 demonstrates a different behavior compared to others. Despite the same Ga growth rate applied, the diameter of the NW at the bottom in NBW-6 is larger compared to the tip. Keeping in mind that the diameter of GaAs NWs decreases with increasing As group flux [64], it may evidence vapor-solid (VS) growth mechanism. As mentioned previously, the Ga droplets can be consumed due to the high As pressure. In this case the preferential diffusion to the Ga droplet region doesn't take place. Consequently, it is believed that the radial growth begins to occur with the contribution of group III and V adatoms under the high group V pressure condition, indicating the change of the growth mechanism from VLS to VS mode [92, 128]. So, it may be proposed that the local radial VS growth rate strongly decreases near the droplet within a comparable length to the diffusion length [140]. Accordingly, it is reasonable to

observe the GaAs NWs with larger diameter at the bottom, for the sample NBW-6 compared to NBW-5, despite the fixed Ga growth rate.

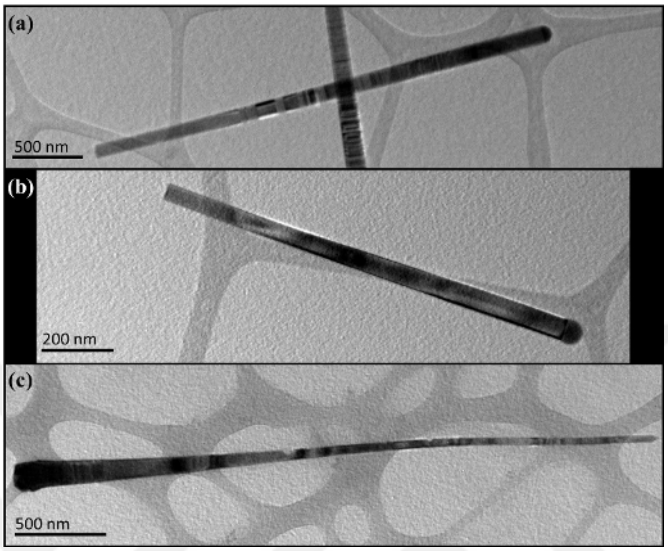

Figure 7.15. *TEM images of the samples (a) NBW-4, (b) NBW-5 and c) NBW-6.*

TEM offers information about the chemical composition of the NWs. As can be seen from Figure 7.16, the chemical analysis (the elements Ga K and As K) of a GaAs NW obtained from NBW-4 revealed that it has a well-defined Ga droplet at the tip segment. It is evidenced that the initiation of GaAs NWs occurs according to VLS growth mechanism. Besides, the same elemental ratio was obtained for the all the samples (not shown here) as an indication of homogeneous chemical structure throughout the GaAs NW.

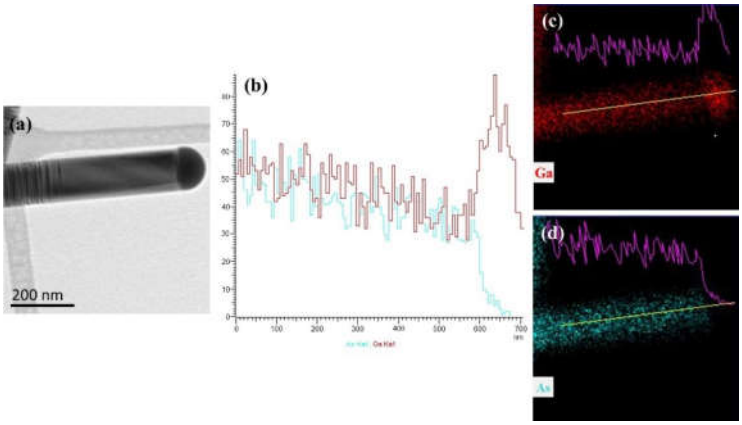

Figure 7.16. *(a) The TEM image and (b) EDS line profile analysis of a single GaAs NW collected from NBW-4 and (c-d) corresponding elemental distribution maps of Ga-K, As-K, respectively.*

Figure 7.17 displays TEM images of a GaAs NW from the sample NBW-5, including HRTEM images and FFT/SAED patterns obtained from different segments. The GaAs NW is dominated by ZB crystal phase, while some WZ and twin ZB domains is also observed along the NW. The crystallization begins with planar defects together with polytypism that corresponds to a short segment with a length of 40 nm at the bottom of the NW. It is followed by pure ZB phase (Figure 7.17(b-c)). Furthermore, a twin region is observed in Figure 7.17(d) indicating {111} planes with a 0.33 nm spacing. The SAED pattern in Figure 7.17(f) confirms the rotational twin ZB phase. After a twinned free ZB crystal in Figure 7.17(j), WZ and twinned ZB regions is observable at the tip of GaAs NW. The SAED pattern in Figure 7.17(k) is a superposition of WZ and twinned ZB. The streaky diffraction spots indicate the planar defects such as stacking faults. At the top of GaAs NW under the Ga droplet, WZ segment is found and it is confirmed by FFT pattern as shown in Figure 7.17(l). As a consequence, 86% region of GaAs NW exhibits predominantly ZB in structure. The WZ formation under the Ga droplet points to the abrupt change in the growth regime [93, 130, 147,148]. It is attributed to the Ga flux termination after the growth. In a growth process, when the Ga flux is terminated, the NW growth does not cease immediately by reducing the substrate temperature. The Ga droplets begin to decrease and As flux still fed the Ga droplets. Therefore, a transition layer is generated consisting of twin and stacking faults following WZ phase.

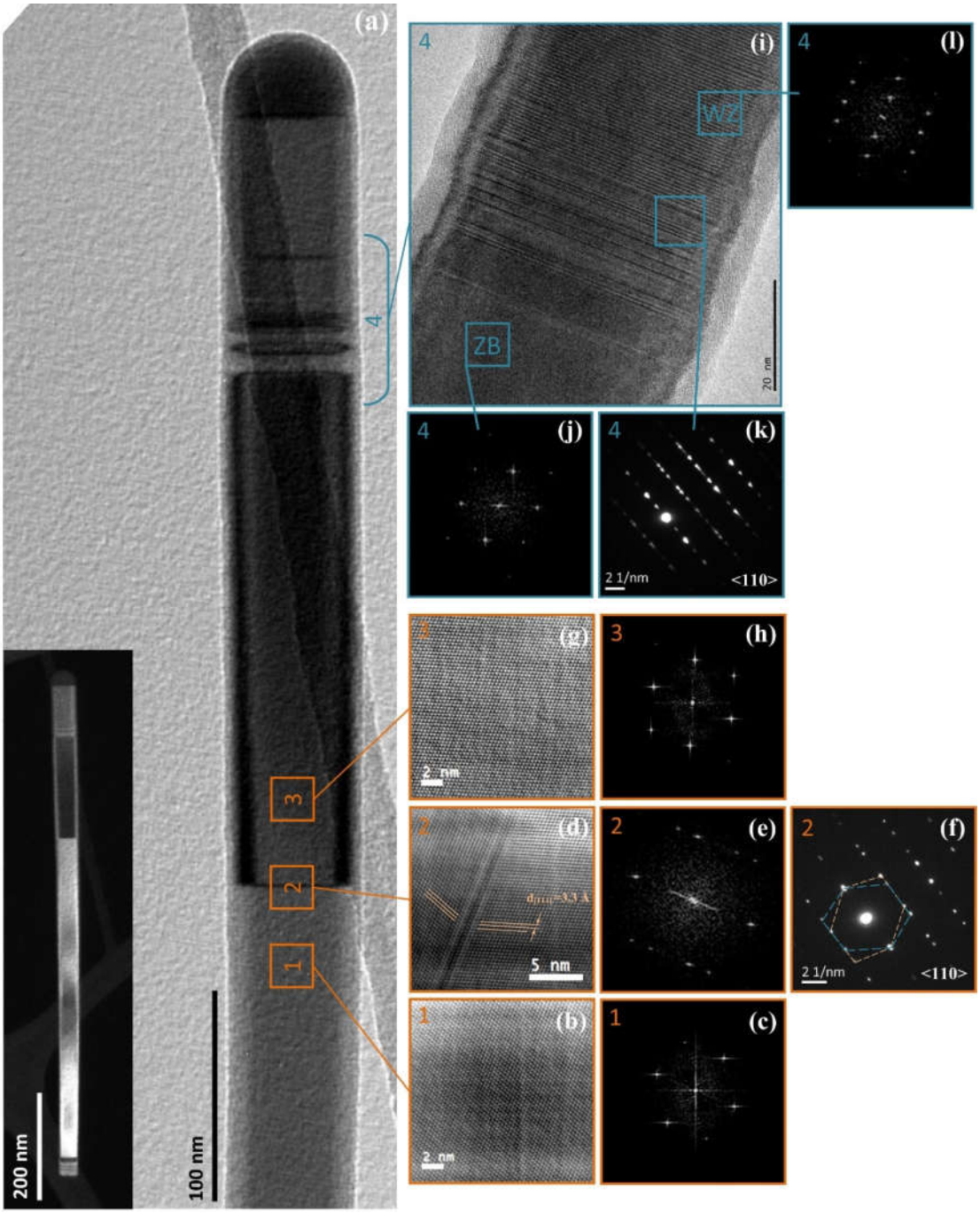

Figure 7.17. *The TEM images of a NW belong to the sample NBW-5. (a) HRTEM low-magnification overview, (b) HRTEM image of pure ZB phase, (c) FFT pattern of point 1. (d) HRTEM image of twinned ZB segment, (e) and (f) FFT and SAED patterns of rotational twinned ZB region (point 2), respectively, (g) HRTEM image of pure ZB phase, (h) FFT pattern of point 3, (i) HRTEM image of the top segment of NW, (j) FFT pattern of pure ZB segment, (k) SAED pattern that indicates WZ and twinned ZB with the planar defects region and (l) FFT pattern that shows WZ phase of the segment under the Ga droplet.*

7.3. Conclusions

Following the results obtained, the effect of growth temperature on self-assisted GaAs NWs can be mainly summarized as follows: (1) By increasing growth temperature, the vertical and non-vertical NWs variation occurs with the influence on the GaAs seed formation and that induces an increment in the density of non-vertical NWs; (2) length of NWs are changed depending on the growth temperature due to growth kinetics; (3) the density of NWs are related with the impact on Ga droplet distribution on the surface at the initial stage; (4) GaAs NWs grown at higher temperature are apparently grown in the favour of ZB structure phase; and (5) the growth temperature has a control on the coverage of parasitic growth on the surface.

Besides, it is found that the Ga growth rate is the main effect on the amount of parasitic growth by taking into account high Ga growth rate. By decreasing Ga flux, the residuals on the Si substrates can be dramatically decreased. Also, the diameter of the GaAs NWs can be adjusted by tuning the Ga growth rate. On the contrary, no significant influence of the Ga and As flux on the NW density is observed at the studied growth conditions.

It is confirmed that the lengths of GaAs NWs are mainly influenced by the As flux ratio. However, the increment in the As flux can cause the depletion of Ga droplets depending on the growth condition. At the same time, the impact of the group V/III flux ratio on the morphology is seen from the obtained results with the change of NW diameter due to the Ga droplet size alteration during the growth or cooling process and the divert in the growth mode from VLS to VS.

Consequently, the control of nucleation mechanism is crucial during the NW growth. It is clearly seen that the NW growth is very sensitive to the growth parameters. Fine adjustment should be necessary to create a stable specie contribution to the nucleation seed during the growth process for the achievement of a homogenous NW in terms of the morphology and the crystal structure. This is because, the crystal phase variation with planar defects and the change of diameter along the NW have a negative influence on the performance of possible devices that will be fabricated in the future. Finally, the results point out that further investigations should be performed about the growth dynamics of the NWs for the sake of reproducibility and high quality.

8. CONCLUSIONS AND FINAL REMARKS

The crystal quality of the heteroepitaxial GaSb epilayers on nominal Si (100) substrates was investigated in terms of AlSb NL layer thickness, growth and post annealing temperature. The results demonstrate that the best GaSb epilayer crystal quality was obtained for an AlSb NL thickness of 20 ML and growth temperature of 530 ^{o}C. Although structural improvements were observed for the samples grown at higher temperatures, it was shown that the optical quality and the surface roughness of the samples worsen with an increase in the growth temperature. Similarly, while improving the structural quality by the post annealing it was revealed that the improvement in the optical quality and surface roughness of the samples were limited. As a consequence, considering the structural, optical and surface roughness properties of the GaSb epilayers on nominal Si (100) substrates, the best performance was obtained from the GaSb epilayer grown at 530 ^{o}C with an AlSb NL thickness of 20 ML and post annealed at 550 ^{o}C for 30 min. For this sample, an RMS value of 0.98 nm for a scan area of 100 μm^2 was obtained.

Both AFM and SEM images indicate the formation of MTs and APBs at the surface of the GaSb epilayers grown on Si (100) nominal substrates. Counting the MTs in SEM images the MT densities were determined and it was found that the lowest MT density was achieved for the sample where 20 ML AlSb NL thickness was used. Besides, it was shown that, although an increase in the growth temperature reduces slightly the MT density and the RMS value increases which is undesired for the growth of device quality GaSb films on nominal Si (100) substrates. Among all the samples grown on nominal Si (100) substrate the lowest APB and MT densities of 0.50 $\mu m^{-1}$and 186 cm^{1}, respectively were achieved. Furthermore, it was found that, longer annealing times improve the crystal quality of the grown GaSb epilayers. As such, the APB density as low as 0.48 μm^{-1} was obtained with the post-growth annealing for 60 min and by applying an intermediate annealing step. Also, the FWHM of 229 arcsec and the TD density of $1.72x10^{-8}$ cm^{-2} were achieved for the sample grown with an intermediate annealing step. Considering the obtained values, these results are the best values reported in the literature for the GaSb epilayers grown on nominal Si (100) substrates up to now. In addition, the growth of GaSb epilayers on Si (100) substrate was demonstrated

by applying GaSb NL as an intermediate layer. By optimizing the GaSb NL, it is believed that the nucleation sites are formed to initiate the GaSb epilayer as AlSb NL.

In the case of the growth of GaSb epilayers on vicinal substrate, the impact on the APB suppression is revealed by choosing the Si (100) substrate with optimum miscut angle. Although the surface roughness of grown epilayers worsen in general, it still seems the most effective way for the reduction of APB and TD densities together. Besides, the SLs in the GaSb epilayer has a role as a dislocation filter, when considering the reduced etch pits on the surface which is attributed the TDs. By increasing the SL period, it is also achieved to reduce the APB density effectively.

Regarding GaAs NWs, the influence of the group III and V BEP on the growth of GaAs NWs were investigated. It was determined that the effect of the group V BEP on the growth rate of the GaAs NWs is much higher compared group III. Namely, an increase in the group III and V BEP by a factor of 4 increases the growth rate by a factor of ~1.3 and 3.5, respectively. On the other hand, it was observed that the effect of the increase in group III is more pronounced in the diameter of the GaAs NWs which is a disadvantage considering quantum confinement effect and the parasitic growth. So, the diameter of the GaAs NWs and the amount of parasitic growth can be adjusted by tuning the Ga growth rate. Besides, it was demonstrated that depending on the growth temperature the vertical and non-vertical NW densities changed between 1.0-3.9×10^7 and 1.1-1.2 ×10^7 cm^{-2}, respectively. Also, it was demonstrated that the NWs are all in the vertical direction for the sample grown at the lowest growth temperature (580 ^oC). In addition, convex-like GaAs NWs were identified in the same sample which is believed to be important for fabricating GaAs NW based devices. It was also confirmed that the increment in the As flux can cause the depletion of Ga droplets depending on the growth condition. At the same time, the impact of the group V/III flux ratio on the morphology was seen from the obtained results with the change of NW diameter due to the Ga droplet size alteration during the growth or cooling process and the divert in the growth mode from VLS to VS.

In the light of those results, I believe that there is more room to improve the crystal quality of GaSb epilayers on Si substrates. Since, the fabricated devices are very sensitive to the defects throughout the device structure, the APBs should be suppressed significantly so that one does not experience a short in the device. To this purpose, miscut substrates seems

to be a promising method. Hence, it would be a good idea to focus on those substrates and optimize the growth condition for the device quality GaSb epilayer. Since, SL structure embedded in the GaSb epilayer serves as defect blocker a combination of SL structure together with miscut substrates would yield the best result. Optimization of GaAs NWs are significantly harder compared to 2D layer growth due to the highly sensitive growth variables. However, there are very promising results which lead us to study functional GaAs NWs in more detail in the near future. In order to achieve the best result, it is believed that sets of samples should be grown on the same batch of substrates so that the growth parameters would be optimized consistently. Hence, in the future one can grow sets of samples to optimize the growth parameter and achieve the monophase GaAs NW (either a complete ZB or WZ phase).

REFERENCES

[1] Miller, D.A.B (2009). Device Requirements for optical interconnects to silicon chips. *Proceedings of the IEEE*, 97, 1166-1185.

[2] Wang, R., Vasiliev, A., Muneeb, M., Malik, A., Sprengel, S., Boehm, G., Amann, M.C., Simonyte, I., Vizbaras, A., Vizbaras, K., Baets, R., Roelkens, G. (2017). III-V-on-silicon photonic integrated circuits for spectroscopic sensing in the 2-4 μm wavelength range. *Sensors*, 17, 1788 (1-21).

[3] Bolkhovityanov, Y.B. and Pchelyakov, O.P. (2009). III-V compounds-on-Si: Heterostructure fabrication, application and prospects. *The Open Nanoscience Journal*, 3, 20-33.

[4] Liang, D., Roelkens, G., Baets, R., Bowers, J.E. (2010). Hybrid integrated platforms for silicon photonics. *Materials*, 3, 1782-1802.

[5] Duan, G.H., Jany, C., *et. al.* (2014). Hybrid III-V on silicon lasers for photonic integrated circuits on silicon. *IEEE Journal of Selected Topics in Quantum Electronics*, 20, 6100213.

[6] Geum, D., Park, M., Lim, J.Y., Yang, H., Song, J.D., Kim, C.Z., Yoon, E., Kim, S., Choi, W.J. (2016). Ultra-high-throughput production of III-V/Si wafer for electronic and photonic applications. *Scientific Reports*, 6, 20610 (1-10).

[7] Ghegin, E., Rodriguez, Ph., Nemouchi, F., Jany, Ch., Brihoum, M., Halimaoui, A., Sagnes, I., Szelag, B. (2016). Towards contact integration for III-V/Silicon heterogeneous photonics devices. *IEEE International Interconnect Technology Conference/Advanced Metallization Conference*, San Jose, CA, USA, 23-26 May., 2016, IITC-AMC. pp. 69-71. ISBN: 978-1-5090-0386-0.

[8] Kao, Y.C., Chou, H.M., Hsu, S.C., Lin, A., Lin, C.C., Shih, Z.H., Chang, C.L., Hong, H.F., Horng, R.H. (2019). Performance comparison of III-V//Si and III-V//InGaAs multi-junction solar cells fabricated by the combination of mechanical stacking and wire bonding. *Sciencific Reports*, 9, 4308.

[9] Li, Q., Lau, K.M. (2017). Epitaxial growth of highly mismatched III-V materials on (001) silicon for electronics and optoelectronics. *Progress in Crystal Growth and Characterization of Materials*, 63, 105-120.

[10] Kroemer, H., Polasko, K.J., Wright, S.C. (1980). On the (110) orientation as the preferred orientation for the molecular beam epitaxial growth of GaAs on Ge, GaP on Si, and similar zincblendeon diamond systems. *Applied Physics Letters*, 36, 763-765.

[11] Fang, S.F., Adomi, K., Iyer, S., Morkoç, H., Zabel, H. (1990). Gallium arsenide and other compound semiconductors on silicon. *Journal of Applied Physics*, 68, R31-R58.

[12] Yang, V.K., Groenert, M., Leitz, C.W., Pitera, J., Currie, M.T. (2003). Crack formation in GaAs heteroepitaxial films on Si and SiGe virtual substrates. *Journal of Applied Physics*, 93, 3859-3865.

[13] Brammertz, G., Mols, Y., Degroote, S., Motsnyi, V., Leys, M., Borghs, G., Caymax, M. (2006). Low-temperature photoluminescence study of thin epitaxial GaAs films on Ge substrates. *Journal of Applied Physics*, 99, 093514 (1-10).

[14] Tea, E., Vidal, J., Pedesseau, L., Cornet, C., Jancu, J.-M., Even, J., Laribi, S., Guillemoles, J.-F., Durand, O. (2014). Theoretical study of optical properties of anti phase domains in GaP. *Journal of Applied Physics*, 115, 063502 (1-5).

[15] Alcotte, R., Martin, M., Moeyaert, J., Cipro, R., David, S., Bassani, F., Ducroquet, F., Bogumilowicz, Y., Sanchez, E., Ye, Z., Bao, X.Y., Pin, J.B., Baron, T. (2016). Epitaxial growth of antiphase boundary free GaAs layer on 300 mm Si(001) substrate by metalorganic chemical vapour deposition with high mobility. *APL Materials*, 4, 046101 (1-6).

[16] Kunert, B., Mols, Y., Baryshniskova, M., Waldron, N., Schulze, A., Langer, R. (2018). How to control defect formation in monolithic III/V hetero-epitaxy on (100) Si? A critical review on current approaches. *Semiconductor Science and Technology*, 33, 093002 (1-19).

[17] Jung, D., Herrick, R., Norman, J., Turnlund, K., Jan, C., Feng, K., Gossard, A.C., Bowers, J.E. (2018). Impact of the threading dislocation density on the lifetime of InAs quantum dot lasers on Si. *Applied Physics Letters*, 112, 153507 (1-4).

[18] Datta, S., Dewey, G., Fastenau, J.M., Hudait, M.K., Loubychev, D., Liu, W.K., Radosavljevic, M., Rachmady, W., Chau, R. (2007). Ultrahigh-speed 0.5 V supply voltage $In_{0.7}Ga_{0.3}As$ quantum-well transistors on silicon substrate. *IEEE Electron Device Letters*, 28, 685-687.

[19] Cerutti, L., Rodriguez, J.B., Tournie, E. (2010). GaSb-based laser, monolithically grown on silicon substrate, emitting at 1.55 μm at room temperature. *IEEE Photonics Technology Letters*, 22, 553-555.

[20] Lee, A., Liu, H., Seeds, A. (2013). Semiconductor III-V lasers monolithically grown on Si substrates. *Semiconductor Science Technology*, 28, 015027 (1-11).

[21] Jain, N., Hudait, M.K. (2014). III-V multijunction solar cell integration with silicon: Presen status, challenges and future outlook. *Energy Harvesting and Systems*, 1, 121-145.

[22] Durlin, Q., Perez, J.P., Cerutti, L., Rodriguez, J.B., Cerba, T., Baron, T., Tournié E., Christol, P. (2019). Midwave infrared barrier detector based on Ga-free InAs/InAsSb type-II superlattice grown by molecular beam epitaxy. *Infrared Physics&Technology*, 96, 39-43.

[23] Levinshtein, M., Rumyantsev, S., Shur, M. (1996). *Handbook Series on Semiconductor Parameters*. Singapore: World Scientific.

[24] Safa, K., Capper, P. (2017). *Handbook of Electronic and Photonic Materials*. Switzerland: Springer.

[25] Joullié, A., Christol, P. (2003). GaSb-based mid-infrared 2-5 μm laser diodes. *Comptes Rendus Physique*, 4, 621-637.

[26] Bett, A.W., Dimroth, F., Stollwerck, G., Sulima, O.V. (1999). III-V compounds for solar cell applications. *Applied Physics A*, 69, 119-129.

[27] Razeghi, M., Haddadi, A., Hoang, A.M., Huang, E.K., Chen, G., Bogdanov, S., Darvish, S.R., Callewaert, F., McClintock, R. (2013). Advances in antimonide-based type-II superlattices for infrared detection and imaging at center for quantum devices. *Infrared Physics&Technology*, 59, 41-52.

[28] Nainani, A., Irisawa, T., Yuan, Z., Bennett, R.B., Boos, J.B., Nishi, Y., Saraswat, K.C. (2011). Optimization of the Al_2O_3/GaSb interface and a high-mobility GaSb pMOSFET. *IEEE Transactions on Electron Devices,* 58, 3407-3415.

[29] Akahane, K., Yamamoto, N., Gozu, S., Ueto, A., Ohtani, N. (2005). Initial growth stage of GaSb on Si(001) substrates with AlSb initiation layers. *Journal of Crystal Growth,* 283, 297-302.

[30] Huang, S.H., Balakrishnan, G., Khoshakhlagh, A., Dawson, L.R., Huffaker, D.L. (2008). Simultaneous interfical misfit array formation and antiphase domain suppression on miscut silicon substrate. *Applied Physics Letters,* 93, 071102 (1-3).

[31] Noh, Y.K., Kim, M.D., Oh, J.E., Yang, W.C. (2010). Structural and optical properties of GaSb films grown on AlSb/Si (100) by insertion of a thin GaSb interlayer grown at a low temperature. *Journal of the Korean Physical Society,* 57, 173-177.

[32] Noh, Y.K., Kim, M.D., Oh, J.E., Yang, W.C., Kim, Y.H. (2011). Growth of low defect AlGaSb films on Si (100) using AlSb and InSb quantum dots intermediate layers. *Journal of Crystal Growth,* 323, 405-408.

[33] Woo, S.Y., Vajargah, S.H., Ghanad-Tavakoli, S., Kleiman, R.N., Botton, G.A. (2012). Direct observation of anti-phase boundaries in heteroepitaxy of GaSb thin films grown on Si(001) by transmission electron microscopy. *Journal of Applied Physics,* 112, 0774306 (1-7).

[34] Vajargah, S.H., Ghanad-Tavakoli, S., Preston, J.S., Kleiman, R.N., Botton, G.A. (2013). Growth mechanism of GaSb heteroepitaxial films on Si with an AlSb buffer layer. *Journal of Applied Physics,* 114, 113101 (1-9).

[35] Rodriguez, J.B., Madiomanana, K., Cerutti, L., Castellano, A., Tournié, E. (2016). X-ray diffraction study of GaSb grown by molecular beam epitaxy on silicon substrates. *Journal of Crystal Growth,* 439, 33-39.

[36] Kim, Y.H., Lee, J.Y., Noh, Y.G., Kim, M.D., Cho, S.M. (2006). Growth mode and structural characterization of GaSb on Si(001) substrate: A transmission electron microscopy study. *Applied Physics Letters,* 88, 241907 (1-3).

[37] Kim, Y.H., Noh, Y.K., Kim, M.D., Oh, J.E., Chung, K.S. (2010). Transmission electron microscopy study of the initial growth stage of GaSb grown on Si (001) substrate by molecular beam epitaxy. *Thin Solid Films,* 518, 2280-2284.

[38] Vajargah, S.H., Coulliard, M., Cui, K., Ghanad-Tavakoli, S., Robinson, B., Kleiman, R.N., Preston, J.S., Botton, G.A. (2011). Strain relief and AlSb buffer layer morphology in GaSb heteroepitaxial films grown on Si as revealed by high-angle annular dark-field scanning transmission electron microscopy. *Applied Physics Letters,* 98, 082113 (1-3).

[39] Vajargah, S.H., Woo, S.Y., Ghanad-Tavakoli, S., Kleiman, R.N., Preston, J.S., Botton, G.A. (2012). Atomic-resolution study of polarity reversal in GaSb grown on Si by scanning transmission electron microscopy. *Journal of Applied Physics,* 112, 093101 (1-9).

[40] Rodriguez, J.B., Cerutti, L., Patriarche, G., Largeau, L., Madiomanana, K., Tournié, E. (2017). Characterization of antimonide based material grown by molecular epitaxy on vicinal silicon substrates via a low temperature AlSb nucleation layer. *Journal of Crystal Growth*, 477, 65-71.

[41] Cerba, T., Martin, M., Moeyaert, J., David, S., Rouviere, J.L., Cerutti, L., Alcotte, R., Rodriguez, J.B., Bawedin, M., Bourty, H., Bassani, F., Bogumilowicz, Y., Gergaud, P., Tournié, Baron, T. (2018). Anti phase boundary free GaSb layer grown on 300 mm (001)-Si substrate by metal organic chemical vapor depositon. *Thin Solid Films*, 645, 5-9.

[42] Huu Ha, M.T., Huynh, S.H., Do, H.B., Nyguyen, T.A., Luc, Q.H., Chang, E.Y. (2017). Demonstrating antiphase domain boundary-free GaAs buffer layer on zero off-cut Si (001) substrate for interfacial misfit dislocation GaSb film by metalorganic chemical vapor depositon. *Materials Research Express*, 4, 085901 (1-7).

[43] Craig, A.P., Carrington, P.J., Liu, H., Marshall, A.R.J. (2016). Characterization of 6.1 Å III-V materials grown GaAs and Si: A comparison of GaSb/GaAs epitaxy and GaSb/AlSb/Si epitaxy. *Journal of Crystal Growth*, 435, 56-61.

[44] Madisetti, S.K., Tokranov, V., Greene, A., Novak, S., Yakimov, M., Oktyabrsky, S., Bentley, S., Jacob, A.P. (2014). GaSb on Si: Structural defects and their effect on surface morphology and electrical properties. *Mater. Res. Soc. Symp. Proc.*, 1635, 115-120.

[45] Sasaki, S., Dropiewski, K., Madisetti, S., Tokranov, V., Yakimov, M., Oktyabrsky, S., Bentley, S., Galatage, R., Jacob, A.P. (2017). Electrical properties related to growth defects in metamorphic GaSb films on Si. *Journal of Vacuum Science&Technology B*, 35, 011203 (1-7).

[46] Sun, Y., Rogers, J.A. (2004). Fabricating semiconductor nano/microwires and transfer printing ordered arrays of them onto plastic substrate. *Nano Letters*, 4, 1953-1959.

[47] Joyce, H.J., Gao, Q., Tan Hoe, H., Jagadish, C., Kim, Y., Zou, J., Smith, L.M., Jackson, H.E., Yarrison-Rice, J.M., Parkinson, P., Johnston, M.B. (2011). III-V semiconductor nanowires for optoelectronic device applications. *Progress in Quantum Electronics*, 35, 23-75.

[48] Zhang, Y., Wu, J., Aagesen, M., Liu, H. (2015). III-V nanowires and nanowire optoelectronic devices. *Journal of Physics D: Applied Physics*, 48, 463001 (1-29).

[49] Wernersson, L.E., Thelander, C., Lind, E., Samuelson, L. (2010). III-V nanowires-extending a narrowing road. *Proceedings of the IEEE*, 98, 2047-2060.

[50] Svensson, J., Dey, A.W., Jacobsson, D., Wernersson, L.E. (2015). III-V nanowires complementary metal-oxide semiconductor transistors monolithically integrated on Si. *Nano Letters*, 15, 7898-7904.

[51] Tomioka, K., Tanaka, T., Hara, S., Hiruma, K., Fukui, T. (2011). III-V nanowires on Si substrate: Selective-area growth and device applications. *IEEE Journal of selected topics in Quantum Electronics*, 17, 1112-1129.

[52] LaPierre, R.R., Chia, A.C.E., Gibson, S.J., Haapamaki, C.M., Boulanger, J., Yee, R., Kuyanov, P., Zhang, J., Tajik, N., Jewell, N., Rahman, K.M.A. (2013). III-V nanowire photovoltaics: Review of design for high efficiency. *Physica Status Solidi RRL*, 7, 815-830.

[53] Kim, H., Lee, W., Farrell, A.C., Morales, J.S.D., Senanayake, P., Prikhodko, S.V., Ochalski, T.J., Huffaker, D.L. (2017). Monolithic InGaAs nanowire array lasers on silicon-on-insulator operating at room temperature. *Nano Letters*, 17, 3465-3470.

[54] Bae, M., Kim, B., Ha, D., Lee, S.J., Sharma, R., Choi, K.J., Kim, J., Choi, W.J., Shin, J.C. (2014). Non-lithographic growth of core-shell GaAs nanowires on Si for optoelectronic applications. *Crystal Growth&Design*, 14, 1510-1515.

[55] Yao, M., Huang, N., Cong, S., Chi, C., Seyedi, M.A., Lin, Y., Cao, Y., Pvinelli, M.L., Dapkus, P.D., Zhou, C. (2014). GaAs nanowire array solar cells with axial p-i-n junctions. *Nano Letters*, 14, 3293-3303.

[56] Ho, J., Tatebayashi, J., Sergent, S., Fong, C.F., Iwamoto, S., Arakawa, Y. (2015). Low-threshold near-infrared GaAs-AlGaAs core-shell nanowire plasmon laser. *ACS Photonics*, 2, 165-171.

[57] Peng, K., Parkinson, P., Fu, L., Gao, Q., Jiang, N., Guo, Y., Wang, F., Joyce, H.J., Boland, J.L., Tan, H.H., Jagadish, C., Johnston, M.B. (2015). Single nanowire photoconductive terahertz detectors. *Nano Letters*, 15, 206-210.

[58] Wu, Y., Yang, P. (2001). Direct observation of vapor-liquid-solid nanowire growth. *Journal of the American Chemical Society*, 123, 3165-3166.

[59] Harmand, J.C., Patriarche, G., Péré-Laperne, N., Mérat-Combes, M-N., Travers, L., Glas, F. (2005). Analysis of vapor-liquid-solid mechanism in Au-assisted GaAs nanowire growth. *Applied Physics Letters*, 87, 203101 (1-3).

[60] Dick, K.A., Caroff, P. (2014). Metal-seeded growth of III-V semiconductor nanowires: towards gold-free synthesis. *Nanoscale*, 6, 3006-3021.

[61] Perea, D.E., Allen, J.E., May, S.J., Wessels, B.W., Seidman, D.N., Lauhon, L.J. (2006). Three-dimensional nanoscale composition mapping of semiconductor nanowires. *Nano Letters*, 6, 181-185.

[62] Allen, J.E., Hemesath, E.R., Perea, D.E., Lensch-Falk, J.L., Li, Z.Y., Yin, F., Gass, M.H., Wang, P., Bleloch, A.L., Palmer, R.E., Lauhon, L.J. (2008). High-resolution detection of Au catalyst atoms in Si nanowires. *Nature Nanotechnology*, 3, 168-173.

[63] Bar-Sadan, M., Barthel, J., Shtrikman, H., Houben, L. (2012). Direct imaging of single Au atoms within GaAs nanowires. *Nano Letters*, 12, 2352-2356.

[64] Paek, J.H., Nishiwaki, T., Yamaguchi, M., Sawaki, N. (2009). Catalyst free MBE-VLS growth of GaAs nanowires on (111)Si substrate. *Physica Status Solidi C*, 6, 1436-1440.

[65] Plissard, S., Dick, K.A., Larrieu, G., Godey, S., Addad, A., Wallart, X., Caroff, P. (2010). Gold-free growth of GaAs nanowires on silicon: arrays and polytypism. *Nanotechnology*, 21, 385602 (1-8).

[66] Somaschini, C., Bietti, S., Trampert, A., Jahn, U., Hauswald, C., Riechert, H., Sanguinetti, S., Geelhaar, L. (2013). Control over the number density and diameter of GaAs nanowires on Si(111) mediated by droplet epitaxy. *Nano Letters*, 13, 3607-3613.

[67] Munshi, A.M., Dheeraj, D.L., Fauske, V.T., Kim, D.C., Huh, J., Reinertson, J.F., Ahtapodov, L., Lee, K.D., Heidari, B., van Helvoort, A.T.J, Fimland, B.O., Weman, H. (2014). Position-controlled uniform GaAs nanowires on silicon using nanoimprint lithography. *Nano Letters*, 14, 960-966.

[68] Russo-Averchi, E., Heiss, M., Michelet, L., Krogstrup, P., Nygard, J., Magen, C., Morante, J.R., Uccelli, E., Arbiol, J., Fontcuberta i Morral, A. (2012). Suppression of three dimensional twinning for a 100% yield of vertical GaAs nanowires on silicon. *Nanoscale*, 4, 1486-1490.

[69] Matteini, F., Tütüncüoğlu, G., Rüffer, D., Alarcón-Lladó, J., Fontcuberta i Morral, A. (2014). Ga-assisted growth of GaAs nanowires on silicon, comparison of surface SiOx of different nature. *Journal of Crystal Growth*, 404, 246-255.

[70] Herman, M.A., Sitter, H. (1996). *Molecular beam epitaxy fundamentals and current status*. Berlin: Springer.

[71] Rijnders, G. and Blank, D.H.A., (2005). Real-time growth monitoring by high-pressure RHEED during pulsed laser deposition. Ogale, S.B., (Ed.), *Thin films and heterostructures for oxide electronics* (368-369). New York: Springer.

[72] Tsao, J.Y. (1993). *Materials fundamentals of molecular beam epitaxy*. San Diego: Academic Press.

[73] Levine, M.S., Golovin, A.A. and Volpert, V.A. (2008). Step-flow growth of a crystal surface by Lévy flights. *A Letters Journal Exploring the Frontiers of Physics*, 82, 28007 (1-5).

[74] H.J. Scheel, (1997). Control of epitaxial growth modes for high performance optoelectronic devices, in: T. Sasaki (Ed.), Proceedings of the International Symposium on Laser and Nonlinear Optical Materials, Data Storage Institute, Singapore.

[75] Adachi, S. (2005). *Properties of group-IV, III-V and II-VI semiconductors*. West Sussex: John Wiley&Sons.

[76] Weinberg, W.H., Reaves, C.M., Nosho, B.Z., Pelzel, R.I., DenBaars, S.P. (2001). Strained-layer heteroepitaxy to fabricate self-assembled semiconductor islands. Nalwa, H.S. (Ed.), *Nanostructured materials and nanotechnology*, (208-241). California: Academic Press.

[77] Fluri, A., Schneider, C.W., Pergolesi, D. (2018). In situ stress measurements of metal oxide thin films. Pryds, N., Esposito, V. (Ed.), *Metal-oxide based thin film structures*, (109-132).

[78] Vilà, A., Cornet, A., Morante, J.R., Ruterana, P., Loubradou, M., Bonnet, R. (1996). Structure of 60º dislocations at the GaAs/Si interface. *Journal of Applied Physics*, 79, 676-681.

[79] Huang, S.H., Balakrishnan, G., Khoshakhlagh, Dawson, L.R., Huffaker, D.L. (2008). Simultaneous interfacial misfit array formation and antiphase domain suppression on miscut substrate. *Applied Physics Letters*, 93, 071102 (1-3).

[80] Akahane, K., Yamamoto, N., Gozu, S., Ohtani, N. (2004). Heteroepitaxial growth of GaSb on Si(001) substrates. *Journal of Crystal Growth*, 264, 21-25.

[81] Al Zoubi, T. (2013). *Molecular beam epitaxial growth of III-V semiconductor nanostructures on silicon substrates*. PhD dissertation. Kassel: University of Kassel, Department of Technological Physics.

[82] Kroemer, H. (1987). Polar-on-nonpolar epitaxy. *Journal of Crystal Growth*, 81, 193-204.

[83] Rubel, O., Baranovskii, S.D. (2009). Formation energies of antiphase boundaries in GaAs and GaP: An *ab Initio* study. *International Journal of Molecular Sciences*, 10, 5104-5114.

[84] Ueda, O., Soga, T., Jimbo, T., Umeno, M. (1989). Direct evidence for self-annihilation of antiphase domains in GaAs/Si heterostructures. *Applied Physics Letters*, 55, 445-447.

[85] Georgakilas, A., Stoemenos, J., Tsagaraki, K., Komninou, Ph., Flevaris, N., Panayotatos, P. (1993). Generation and annihilation of antiphase domain boundaries in GaAs on Si grown by molecular beam epitaxy. *J. Mater. Res.*, 8, 1908-1921.

[86] Georgakilas, A., Papavassiliou, Ch., Constantinidis, G., Tsagaraki, K., Krasny, H., Löchtermann, E., Panayotatos, P. (1996). Effects of Si(100) tilting angle and prelayer conditions on GaAs/Si heterostructures. *Applied Surface Science*, 102, 67-72.

[87] Sakamoto, T., Hashiguchi, G. (1986). Si(001)-2x1 single domain structure obtained by high temperature annealing. *Japanese Journal of Applied Physics*, 25, L78-L80.

[88] Wagner, R.S., Ellis, W.C. (1964). Vapor-liquid-solid mechanism of single crystal growth. *Applied Physics Letters*, 4, 89-90.

[89] Bullis, W.M. (1966). Properties of gold in silicon. *Solid-state Electronics*, 9, 143-168.

[90] Fontcuberta i Morral, A., Colombo, C., Abstreiter, G. (2008). Nucleation mechanism of gallium-assisted molecular beam epitaxy growth of gallium arsenide nanowires. *Applied Physics Letters,* 92, 063112 (1-3).

[91] Plissard, S., Larrieu, G., Wallart, X., Caroff, P. (2011). High yield of self-catalyzed GaAs nanowire arrays grown on silicon via gallium droplet positioning. *Nanotechnology*, 22, 275602 (1-7).

[92] Rudolph, D., Hertenberger, S., Bolte, S., Paosangthong, W., Spirkoska, D., Döblinger, M., Bichler, M., Finley, J.J., Abstreiter, G., Koblmüller, G. (2011). Direct observation of a noncatalytic growth regime for GaAs nanowires. *Nano Letters*, 11, 3848-3854.

[93] Glas, F., Harmand, J-C., Patriarche, G. (2007). Why does wurtzite form in nanowires of III-V zinc blende semiconductors. *Pyhsical Review Letters*, 99, 146101 (1-4).

[94] Kusch, P., Grelich, E., Somaschini, C., Luna, E., Ramsteiner, M., Geelhaar, L., Riechert, H., Reich, S. (2014). Type-II bad alignment of zinc-blende and wurtzite segments in GaAs nanowires: A combined photoluminescence and resonant Raman scattering study. *Physical Review B*, 89, 045310 (1-5).

[95] Arthur, J.R. (2002). Molecular beam epitaxy. *Surface Science*, 500, 189-217.

[96] Cho, A.Y. and Arthur, J.R. (1975). Molecular beam epitaxy. *Progress in Solid-State Chemistry*, 10, 157-191.

[97] McCray, W.P. (2007). MBE deserves a place in the history books. *Nature Nanotechnology*, 2, 259-261.

[98] Franchi, F. (2013). Molecular beam epitaxy: fundamentals, historical background and future prospects. M. Henini (Ed.), Molecular beam epitaxy from research to mass production (1-46). Oxford: Elsevier.

[99] Bracker, A.S., Yang, M.J., Bennett, B.R., Culbertson, J.C., Moore, W.J. (2000). Surface reconstruction phase diagrams for InAs, AlSb, and GaSb. *Journal of Crystal Growth*, 220, 384–392.

[100] Goldstein, J.I., Newbury, D.E., Michael, J. R., Ritchie, N.W.M., Scott, J.H.J., Joy, D.C. (2017). *Scanning electron microscopy and x-ray microanalysis*. Fourth edition. New York: Springer.

[101] Williams, D.B., Carter, C.B. (2009). *Transmission electron microscopy a text book for materials science*. New York: Springer.

[102] Vilalta-Clemente and A., Gloystein, K. (2008). Principles of Atomic Force Microscopy. *Physics of Advanced Materials Winter School*, Thessaloniki, Greece, January 14 18, p.1-10.

[103] Birkholz, M. (2006). *Thin film analysis by x-ray scattering*. Darmstadt: Wiley-VCH.

[104] Bragg, W.H. and Bragg, W.L. (1913). The reflection of X-rays by crystals. *Proceedings of the Royal Society London A*, 88, 428-438.

[105] Ayers, J. E. (1994). The measurement of threading dislocations densities in semiconductor crystals by X-ray diffraction. *Journal of Crystal Growth*, 135, 71-77.

[106] Hasegawa, S., (2012). Reflection high-energy electron diffraction. Kaufmann, E.N., (Ed.), *Characterization of materials* (1925-1938). New York: John Wiley & Sons.

[107] Reijnen, L., Brunton, R., and Grant, I.R. (2005). GaSb single-crystal growth by vertical gradient freeze. *Journal of Crystal Growth*, 275, e595-600.

[108] Jasik, A., Sankowska, I., Wawro, A., Ratajczak, J., Jakieła, R., Pierścińska, D., Smoczyński, Czuba, D.K., Regiński, K. (2018). Comprehensive investigation of the interfacial misfit array formation in GaSb/GaAs material system. *Applied Physics A*, 124, 512(1-12).

[109] Niu, S., Wei, Z., Fang, X., Wang, D., Wang, X., Gao, X., Chen, R. (2017). Brief review of epitaxy and emission properties of GaSb and related semiconductors. *Crystals*, 7, 337(1-21).

[110] Rühle, W., Jakowetz, W., Wölk, C., Linnebach, R., Pilkuhn, M. (1976). Optical studies of free and bound excitonic states in GaSb evidence for deep A+-complexes. *physica status solidi (b)* 73, 255-264.

[111] Xu, Z., He, Z., Song, Y., Fu, X., Rommel, M., Luo, X., Hartmaier, A., Zhang, J., Fang, F. (2018). Topic review: Application of Raman spectroscopy characterization in micro/nano-machining. *Micromachines*, 9, 361(1-23).

[112] Németh, I., Kunert, B., Stolz, W., Volz, K. (2008). Ways to quantitatively defect antiphase disorder in GaP films grown on Si(001) by transmission electron microscopy. *Journal of Crystal Growth*, 310, 4763-4767.

[113] Wong, C.S., Bennett, N.S., Galiana, B., Tejedor, P., Benedicto, M., Molina-Aldarequia, J.M., McNally, P.J. (2012) Structural investigation of MOVPE-grown GaAs on Ge by x-ray techniques. *Semiconductor Science and Technology*, 27, 115012.

[114] Barrett, C.S.C., Martin, T.P., Bao, X.-Y., Kennon, E.L., Gutierrez, L.. Martin, P., Sanchez, E., Jones, K.S. (2016). Effect of bulk growth temperature on antiphase domain boundary annihilation rate in MOCVD-grown GaAs on Si. *Journal of Crystal Growth*, 450, 39-44.

[115] Hudait, M.K., Krupanidhi, S. B. (2001). Self-annihilation of antiphase boundaries in GaAs epilayers on Ge substrates grown by metal-organic vapor-phase epitaxy. *Journal of Applied Physics*, 89, 5972.

[116] Li, Y., Salviati, G., Bongers, M.M.G., Lazzarini, L., Nasi, L., Giling, L.J. (1996). On the formation of antiphase domains in the system of GaAs on Ge. *Journal of Crystal Growth*, 163, 195-202.

[117] Serincan, U., Arpapay, B., (2019). Structural and optical characterization of GaSb on Si (001) grown by molecular beam epitaxy. *Semiconductor Science of Technology*, 34, 035013.

[118] Guo, W., Bondi, A., Cornet, C., Létoublon, A., Durand, O., Rohel, T., Boyer-Richard, S., Bertru, N., Loualiche, S., Even, J., Le Corre, A. (2012). Thermodynamic evolution of antiphase boundaries in GaP/Si epilayers evidenced by advanced X-ray scattering. *Applied Surface Science*, 258, 2808-2815.

[119] Barrett, C.S.C., Atassi, A., Kennon, E.L., Weinrich, Z., Haynes, K., Bao, X.-Y., Martin, P., Jones, K.S. (2019), Dissolution of antiphase domain boundaries in GaAs on Si(001) via post-growth annealing. *Journal of Material Science*, 54, 7028-7034.

[120] Madisetti, S.K., Tokrano,v V., Greene, A., Novak, S., Yakimov, M., Oktyabrsky, S., Bantley, S., Jacob, A.P. (2014). GaSb on Si: Structural defects and their effects on surface morphology and electrical properties. *Materials Research Society Symposium Proceedings*, 1635, 115-120.

[121] Barbier, L., Khater, A., Salanon, B., Lapujoulade, M. (1991). Observation of the double-step-single-step transition on a vicinal surface of Si (100). *Physical Review B*, 43, 14730-14733.

[122] Bietti, S., Somaschini, C., Frigeri, C., Fedorov, A., Esposito, L., Geelhaar, L., Sanguinetti, S. (2014). Self-assisted GaAs nanowires with delectable number density on silicon without oxide layer. *Journal of Physics D: Applied Physics*, 47, 394002 (1-5).

[123] Heiss, M., Russo-Averchi, E., Dalmau-Mallorqui, A., Tütüncüoğlu, G., Matteini, F., Rüffer, D., Conesa-Boj, S., Demichel, O., Alarcón-Lladó, J., Fontcuberta i Morral, A. (2014). III-V nanowire arrays: growth and light interaction. *Nanotechnology*, 25, 014015 (1-9).

[124] Matteini, F., Dubrovskii, V.G., Rüffer, D., Tütüncüoğlu, G., Fontana, Y., Fontcuberta i Morral, A. (2015). Tailoring the diameter and density of self-catalyzed GaAs nanowires on silicon. *Nanotechnology*, 26, 105603 (1-8).

[125] Heiв, M., Riedlberger, E., Spirkoska, D., Bichler, M., Abstreiter, G., Fontcuberta i Morral, A. (2008). Growth mechanisms and optical properties of GaAs-based semiconductor microstructures by selective area epitaxy. *Journal of Crystal Growth*, 310, 1049-1056.

[126] Lee, S.C., Brueck, S.R.J. (2009). Scaling of the surface migration length in nanoscale patterned growth. *Applied Physics Letters*, 94, 153110 (1-3).

[127] Dastjerdi, M.H.T., Boulanger, J.P., Kuyanov, P., Aagesen, M., LaPierre, R.R. (2016). Methods of Ga droplet consumption for improved GaAs nanowire solar cell efficiency. *Nanotechology*, 27, 475403 (1-7).

[128] Rieger, T., Heiderich, S., Lenk, S., Lepsa, M.I., Grützmacher, D. (2012). Ga-assisted MBE growth of GaAs nanowires using thin HSQ layer. *Journal of Crystal Growth*, 353, 39-46.

[129] Colombo, C., Spirkoska, D., Frimmer, M., Abstreiter, G., Fontcuberta I Morral, A. (2008). Ga-assisted catalyst-free growth mechanism of GaAs nanowires by molecular beam epitaxy. *Pyhsical Review B*, 77, 155326 (1-5).

[130] Cirlin, G.E., Dubrovskii, V.G., Samsonenko, Y.B., Bouravleuv, A.D., Durose, K., Proskuryakov, Y.Y., Mendes, B., Bowen, L., Kaliteevski, M.A., Abram, R.A., Zeze, D. (2010). Self-catalyzed, pure zincblende GaAs nanowires grown on Si (111) by molecular beam epitaxy. *Physical Review B*, 82, 035302 (1-6).

[131] Giang L.T.T., Bougerol, C., Mariette, H., Songmuang, R. (2013). Intrinsic limits governing MBE growth of Ga-assisted GaAs nanowires on Si (111). *Semiconductors*, 364, 118-122.

[132] Samsonenko, Y.B., Cirlin, G.E., Khrebtov, A.I., Bouravleuv, A.D., Polyakov, N.K., Ulin, V.P., Dubrovskii, V.G., Werner, P. (2011). Study of processes of self-catalyzed

growth of GaAs crystal nanowires by molecular beam epitaxy on modified Si (111) surfaces. *Semiconductors*, 45, 431-435.

[133] Detz, H., Kriz, M., MacFarland, D., Lancaster, S., Zederbauer, T., Capriotti, M., Andrews, A.M., Schrenk, W., Strasser, G. (2015). Nucleation of Ga droplets on Si and SiO_x surfaces. *Nanotechnology*, 26, 315601 (1-8).

[134] Tauchnitz, T., Nurmamytov, T., Hübner, R., Engler, M., Facsko, S., Schneider, H., Helm, M., Dimakis, E. (2017). Decoupling the two roles of Ga droplets in the self-catalyzed growth of GaAs nanowires on SiO_x/Si(111) substrates. *Crystal Growth&Design*, 17, 5276-5282.

[135] Shibata, M., Stoyanov, S.S., Ichikawa, M. (1999). Selective growth of nanometer-scale Ga dots on Si(111) surface windows formed in an ultrathin SiO_2 film. *Physical Review B*, 59, 10289-10295.

[136] Krogstrup, P., Popovitz-Biro, R., Johnson, E., Madsen, M.H., Nygard, J., Shtrikman, H. (2010). Structural phase control in self-catalyzed growth of GaAs nanowires on silicon (111). *Nano Letters*, 10, 4475-4482.

[137] Nishinga, T., Kuech, T.F. (2015). *Handbook of Crystal Growth Thin Films and Epitaxy: Basic Techniques*. Oxford: Elsevier.

[138] Uccelli, E., Arbiol, J., Magen, C., Krogstrup, P., Russo-Averchi, E., Heiss, M., Mugny, G., Morier-Genoud, F., Nygard, J., Morante, J.R., Fontcuberta i Morral, A. (2011). Suppression of three dimensional twinning for a 100% yield of vertical GaAs nanowires on silicon. *Nano Letters*, 11, 3827-3832.

[139] Cui, Y., Lauhon, L.J., Gudiksen, M.S., Wang, J., Lieber, C.M. (2001). Diameter-controlled synthesis of single-crystal silicon nanowires. *Applied Physics Letters*, 78, 2214-2216.

[140] Küpers, H., Lewis, R.B., Tahraoui, A., Matalla, M., Krüger, O., Bastiman, F., Riechert, H., Geelhaar, L. (2018). Diameter evolution of selective area grown Ga-assisted GaAs nanowires. *Nano Research*, 11, 2885-2893.

[141] Wu, Z.H., Mei, X., Kim, D., Blumin, M., Ruda, H.E. (2003). Growth, branching, and kinking of molecular-beam epitaxial <110> GaAs nanowires. *Applied Physics Letters*, 83, 3368-3370.

[142] Rajkumar, K.C., Chen, P., Madhukar, A. (1991). A transmission electron microscope study of twin structure in GaAs/GaAs (111)B grown via molecular beam epitaxy. *Journal of Applied Physics*, 69, 2219-2223.

[143] Algra, R.E., Verheijen, M.A., Feiner, L., Immink, G.G.W., Theissmann, R., Enckevort, W.J.P., Vlieg, E., Bakkers, E.P.A.M. (2010). Paired twins and {112} morphology in GaP nanowires. *Nano Letters*, 10, 2349-2356.

[144] Zhou, H.L., Hoang, T.B., Dheeraj, D.L., van Helvoort, A.T., Liu, L., Harmand, J.C., Fimland, B.O., Weman, H. (2009). Wurtzite GaAs/AlGaAs core-shell nanowires grown by molecular beam epitaxy. *Nanotechnology*, 20, 415701 (1-7).

[145] Demichel, O., Heiss, M., Bleuse, J., Mariette, H., Fontcuberta i Morral, A. (2010). Impact of surfaces on the optical properties of GaAs nanowires. *Applied Physics Letters*, 97, 201907 (1-3).

[146] Yang, Z., Yin, Y., Sun, J., Bian, L., Han, N., Zhou, Z., Shu, L., Wang, F., Chen, Y., Song, A., Ho, J.C. (2018). Chalcogen passivation: an in-situ method to manipulate the morphology and electrical property of GaAs nanowires. *Scientific Reports*, 8, 6928 (1-8).

[147] Bauer, B., Rudolph, A., Soda, M., Fontcuberta i Morral, Zweck, J., Schuh, D., Reiger, E. (2010). Position controlled self-catalyzed growth of GaAs nanowires by molecular beam epitaxy. *Nanotechnology*, 21, 435601 (1-5).

[148] Yu, X., Wang, H., Lu, J., Zhao, J., Misuraca, J., Xiong, P., von Molnar, S. (2012). Evidence for structural phase transitions induced by the triple phase line shift in self-catalyzed GaAs nanowires. *Nan Letters*, 12, 5436-5442.

CURRICULUM VITAE

Name-Surname: Burcu ARPAPAY
Birth Place and Date: İstanbul/1984
Foreign Language: English
E-mail: barpapay@eskisehir.edu.tr

Education:

- 2010-2019 **PhD**
  Eskişehir Technical University, Turkey
  Department of Physics
- 2007-2010 **M.Sc.**
  Anadolu University
  Department of Physics
- 2003-2007 **B.Sc.**
  İstanbul University
  Department of Physics
- 1998-2003 **High School**
  Kadıköy Anadolu Lisesi

Publications:

1. Serincan, U., **Arpapay, B.** (2019). Structural and optical characterization of GaSb on Si (001) grown by Molecular Beam Epitaxy. *Semiconductor Science and Technology*, 34, 035013.
2. Gunes, M., Erken, O., Gumus, C., Yalaz, E., Pesen, E., Ukelge, M.O., **Arpapay, B.**, Serincan, U., Taykurt Daday, M., Galvão Gobato, Y., Henini, M. (2016). A comparative photoluminescence study on Mn-Free GaAs/AlAs and Mn-containing $Ga_{1-x}Mn_xAs$/AlAs quantum wells (QWs) grown on various orientations by MBE. *Philosophical Magazine*, 96, 223-229.

3. Ozden, P.B., Arslan, A., **Arpapay, B.**, Ilican, S., Hur, E., Caglar, M., Serincan, U., Aksoy, S. (2014). Structural and optical properties of electrochemically grown fluorine doped zinc oxide rods. *Journal of Nanoelectronics and Optoelectronics*, 9, 590-595.
4. **Arpapay, B.,** Sahin, S., Arikan, B., Serincan, U. (2014). Redundant Sb condensation on GaSb epilayers grown on molecular beam epitaxy. *Thin Solid Films*, 564, 110-114.

Conference Presentations:

1. **Arpapay, B.**, Serincan, U., Molecular Beam Epitaxy of Highly Mismatched GaSb on Si, Oral Presentation, *34th Turkish Physical Society International Physical Congress*, Turkey, 5-9 September 2018.
2. **Arpapay, B.**, Serincan, U., Rapid thermal annealing effect on GaSb epilayer grown on Si substrates, Oral Presentation, *Italian Crystal Growth Conference*, Italy, 20-21 November 2017.
3. Yalaz, E., Pesen, E., Ukelge, M.O., Gunes, M., Erken, O., Gumus, C., **Arpapay, B.**, Serincan, U., Henini, M., A comparative study on Mn-Free GaAs/AlAs and Mn containing GaAs1-xMnx/AlAs quantum wells (QWs) grown on various orientations by MBE, Poster Presentation, *2nd International Nanoscience and Nanotechnolgy for Next Generation*, Turkey, 29-31 October 2015.
4. **Arpapay, B.**, Serincan, U., Optimization of GaSb Epilayers Grown on Si (100) Substrates by Molecular Beam Epitaxy, Poster Presentation, *31st North American Molecular Beam Epitaxy Conference*, Mexico, 4-7 October 2015.
5. Serincan, U., **Arpapay, B.**, Arıkan, B., Comparison of GaSb Epilayers Grown on Si and GaAs Substrates by Molecular Beam Epitaxy, Poster Presentation, *31st North American Molecular Beam Epitaxy Conference*, Mexico, 4-7 October 2015.
6. Kuru Mutlu, H., Serincan, U., **Arpapay, B.**, Aslan, B., Analysis and Comparison of $Al_XGa_{1-X}As$/GaAs LWIR QWIPs, Poster Presentation, *11th Nanoscience and Nanotechnology Conference*, 22-25 June, 2015, Türkiye.
7. **Arpapay, B.**, Serincan, U., InAs nanowires grown on Si (111) substrates with native oxide layer by molecular beam epitaxy, Poster Presentation, *8th Nanowire Growth Workshop*, Netherlands, 25-29 August 2014.

8. Serincan, U., **Arpapay, B.**, Ga-assisted InAs nanowires grown on Si (111) by molecular beam epitaxy, Poster Presentation, *8th Nanowire Growth Workshop*, Netherlands, 25-29 August 2014.
9. **Arpapay, B.**, Serincan, U., The Growth of Self-Catalyzed GaAs Nanowires on (111) Si Substrates by Molecular Beam Epitaxy, Poster Presentation, *Science & Applications of Thin Films,Conference & Exhibition*, Turkey, 15-19 September 2014.
10. **Arpapay, B.**, Sahin, S., Arıkan, B., Serincan, U., Characterization of GaSb Epi-Layers Grown on GaSb Substrates, Poster Presentation, *9th Nanoscience and Nanotechnology Conference*, Turkey, 24-28 June 2013.
11. Sahin, S., **Arpapay, B.**, Serincan, U., MBE Grown GaSb Epi-layers on GaSb Substrate: The Effect of Growth Parameters, Poster Presentation, *9th Nanoscience and Nanotechnology Conference*, Turkey, 24-28 June 2013.
12. Kuru Mutlu, H., **Arpapay, B.**, Arıkan B., Aslan, B., Serincan, U., Characterization of a Multilayer GaAs/AlGaAs Broadband Quantum Well Infrared Photodetectors, Poster Presentation, *6th Nanoscience and Nanotechnology Conference*, Turkey, 25-18 June 2010.

Assigned Projects:

1. "Growth and characterization of III-V group nanostructures on Si substrates by MBE", Eskisehir Technical University Scientific Research Projects, Project No: BAP-1305F092, **Researcher**, Continued.
2. "Growth of Type II InAs/GaSb superlattice structures on Si substrate by molecular beam epitaxy", The Scientific and Technological Research Council of Turkey, Project No: 116F199, **Researcher**, 2019.
3. "Growth and Characterization of High Efficient GaAs-based Solar Cells", Eskisehir Technical University Scientific Research Projects, Project No: 1506F541, **Researcher**, 2019.
4. "The investigation of the usage potential of MBE grown III-V/Bi semiconductor nanostructures in optoelectronic applications", The Scientific and Technological Research Council of Turkey, Project No: 115F063, **Researcher**, 2018.
5. "Growth of InSb detector structure by MBE", Anadolu University Scientific Research Projects, Project No: BAP-1705F287, **Researcher**, 2018.

6. "Growth of GaAs Nanowires on Si Substrates by MBE", Anadolu University Scientific Research Projects, Project No: BAP-1605F468, **Researcher**, 2017.
7. "Growth of High Quality GaSb Epilayers on Si Substrates", Anadolu University Scientific Research Projects, Project No: BAP-1505F304, **Researcher**, 2016.
8. "Characterization of Nanostructured ZnO Films by Electrochemical Technique and Fabrication of Heterostructure Diodes", Anadolu University Scientific Research Projects, Project No: BAP-1207F118, **Researcher**, 2016.
9. "Growth and Characterization of GaSb and InAs layers on GaAs Substrate by Molecular Beam Epitaxy", The Scientific and Technological Research Council of Turkey, Project No: 111T335, **Researcher**, 2014.
10. "Device Fabrication and Characterization of GaAs/AlGaAs Based Semiconductors", Anadolu University Scientific Research Projects, Project No: BAP-091014, **Researcher**, 2010.